THE HONG KONG
POLYTECHNIC UNIVERSITY
香港理工大學
Pao Yue-kong Library
包玉剛圖書館

Copyright Undertaking

This thesis is protected by copyright, with all rights reserved.

By reading and using the thesis, the reader understands and agrees to the following terms:

1. The reader will abide by the rules and legal ordinances governing copyright regarding the use of the thesis.
2. The reader will use the thesis for the purpose of research or private study only and not for distribution or further reproduction or any other purpose.
3. The reader agrees to indemnify and hold the University harmless from and against any loss, damage, cost, liability or expenses arising from copyright infringement or unauthorized usage.

IMPORTANT

If you have reasons to believe that any materials in this thesis are deemed not suitable to be distributed in this form, or a copyright owner having difficulty with the material being included in our database, please contact lbsys@polyu.edu.hk providing details. The Library will look into your claim and consider taking remedial action upon receipt of the written requests.

Pao Yue-kong Library, The Hong Kong Polytechnic University, Hung Hom, Kowloon, Hong Kong

http://www.lib.polyu.edu.hk

DESIGN, ANALYSIS AND APPLICATION OF NOVEL FLUX-CONTROLLABLE FLUX-MODULATED MACHINES

QINGSONG WANG

Ph.D

The Hong Kong Polytechnic University

2018

The Hong Kong Polytechnic University

Department of Electrical Engineering

Design, Analysis and Application of Novel Flux-Controllable Flux-Modulated Machines

Qingsong Wang

A thesis submitted in partial fulfillment of the requirements for the
degree of Doctor of Philosophy

December 2017

CERTIFICATE OF ORIGINALITY

I hereby declare that this thesis is my own work and that, to the best of my knowledge and belief, it reproduces no material previously published or written, nor material that has been accepted for the award of any other degree or diploma, except where due acknowledgement has been made in the text.

Signed____________

December 2017

ABSTRACT

Direct-drive machines have drawn much attention in applications like electric vehicles (EVs), wind power generation systems and industrial cooling fans, etc, which usually operate at low speeds and require high torque density. Compared with gear assist driving systems, direct-drive systems can reduce the size, simplify the structure and operate with higher efficiency. Permanent magnet (PM) machines are good candidates for direct-drive applications due to their inherent high torque density and high efficiency, especially when high magnetic energy magnets are used.

In recent decades, flux-modulated machines have become very popular which have the potential to further improve the torque density of PM machines due to the incorporated gear effect. The air-gap permeance is artfully modulated and significant harmonics will be induced, which can contribute to torque improvement when the pole-pair combination is specifically chosen. Another important feature for direct-drive machines is good flux controllability. Therefore, the machines can achieve wide constant power speed range when worked as motors, and maintain constant output voltage when worked as generators.

The purpose of this thesis is to give a deep investigation on the flux-controllable flux-modulated (FCFM) machines, which can achieve both high torque density and good flux controllability. Bi-directional flux modulating theory is proposed and its analytical model is established. The pole-pair number (PPN) and rotating speed of air-gap harmonics are made clear, which gives an insight of the working principle of

FCFM machines.

Hybrid PM memory machines are firstly proposed, in which both AlNiCo and NdFeB are employed. Through apply DC current pulses, the magnetization state of AlNiCo can be flexibly changed and the air-gap flux is regulated accordingly. NdFeB is used to ensure high output torque. When the armature windings are designed with five phases, good fault-tolerant capability can be realized. The major drawback is the doule air-gap structure, which is relatively complicated and difficult to manufacture.

Based on the double air-gap structures, improved FCFM machine concepts with single air-gap are proposed. The PMs can be employed on both the stator and the rotor. Hybrid excitation can be achieved through two approaches, one is employing DC field windings in the stator slots, the other is injecting DC bias current into the armature winding, which results in DC coil free hybrid excitation. The electromagnetic performances are firstly analyzed using finite element method (FEM), and verified by experimental tests.

PUBLICATIONS ARISING FROM THE THESIS

Book chapter:

[1] **Q. Wang** and S. Niu, "New developments of electrical machines" in the book " Advanced power engineering", to be published by CRC Press.

Accepted Journal Papers:

[1] **Q. Wang** and S. Niu, "A novel DC-coil-free hybrid-excited machine with consequent-pole PM rotor," *Energies*, 2018. (To appear)

[2] **Q. Wang**, S. Niu and L. Yang, "Design optimization of a novel scale-down hybrid-excited dual-PM generator for direct-drive wind power application," *IEEE Trans. Magn.*, vol. 54, pp. 1-4, 2018.

[3] **Q. Wang** and S. Niu, "Design, modeling and control of a novel hybrid excited flux bidirectional modulated generator based wind power generation system," *IEEE Trans. Power Electron.*, vol. 33, pp. 3086 - 3096, 2018.

[4] **Q. Wang**, S. Niu and L. Yang, "Design optimization and comparative study of novel dual-PM excited machines," *IEEE Trans. Ind. Electron.*, vol. 64, pp. 9924-9933, 2017.

[5] **Q. Wang**, S. Niu, and X. Luo, "A novel hybrid dual-PM machine excited by AC with DC bias for electric vehicle propulsion," *IEEE Trans. Ind. Electron.*, 2017, vol. 64, pp. 6908-6919, 2017.

[6] **Q. Wang**, S. Niu, and S. Yang, "Design optimization and comparative study of novel magnetic-geared permanent magnet machines," *IEEE Trans.Magn.*, vol. 53, pp.

1-4, 2017.

[7] **Q. Wang** and S. Niu, "A novel hybrid-excited dual-PM machine with bi-directional flux modulation," *IEEE Trans. Energy Convers.*, vol. 32, pp. 424-435, 2017.

[8] **Q. Wang** and S. Niu, "Overview of flux-controllable machines: Electrically excited machines, hybrid excited machines and memory machines," *Renewable and Sustainable Energy Reviews,* vol. 68, pp. 475-491, 2017.

[9] S. Ho, **Q. Wang**, S. Niu, and W. Fu, "A novel magnetic-geared tubular linear machine with halbach permanent-magnet arrays for tidal energy conversion," *IEEE Trans.Magn.,* vol. 51, pp. 1-4, 2015.

[10] **Q. Wang**, S. Niu, S. Ho, W. Fu, and S. Zuo, "Design and analysis of novel magnetic flux-modulated mnemonic machines," *Electric Power Applications, IET,* vol. 9, pp. 469-477, 2015.

[11] **Q. Wang** and S. Niu, "Electromagnetic design and analysis of a novel fault-tolerant flux-modulated memory machine," *Energies,* vol. 8, pp. 8069-8085, 2015.

Accepted Conference Papers:

[1] **Q. Wang** and S. Niu, "A novel hybrid-excited flux bidirectional modulated machine for electric vehicle propulsion," in *2016 IEEE Vehicle Power and Propulsion Conference (VPPC),* 2016, pp. 1-6.

[2] **Q. Wang** and S. Niu, "Design optimization and comparative analysis of

dual-stator flux modulation machines," in *43th Annual Conference of the IEEE Industrial Electronics Society (IECON 2017)*.

Patents:

[1] S. Niu, **Q. Wang**, W. Fu, "An excitation directly controlled d-q self-decoupled wide speed range machine," Patent No.: CN106712332 A.

ACKNOWLEDGEMENTS

First of all, I would like to express my most sincere gratitude and appreciation to my chief supervisor Dr. Shuangxia Niu, for her constant and invaluable guidance, inspiration and encouragement throughout these four years. I must deliver my gratitude to my co-supervisor Professor WN Fu for his genuine guidance in my research. I have learnt a lot from his dedication, attitude and devotion to not only the academic activities but also the way of life.

Many thanks are also given to all the students and research assistants in my group for their support, encouragement and opinions, most notably Dr. Yanpu Zhao, Dr. Xiu Zhang, Dr. Lin Yang, Dr. Yulong Liu, Dr. Yunchong Wang, Mr. Linghan Li, Mr. Tiantian Sheng, Mr. Xing Zhao, Mr. Yunpeng Zhang, Miss. Yiduan Chen, Miss Xiaoyu Liu and Miss Xu Weng.

Last but not the least, I wish to express my deepest appreciation to my family, especially my wife Ms. Zizhou Wang and my son Yichen Wang, for their constant understanding and encouragement as well as genuine support. Without these, this work would have been much more difficult.

TABLE OF CONTENTS

LIST OF FIGURES

LIST OF TABLES

CHAPTER 1 INTRODUCTION

1.1 BACKGROUND

Electrical machines are devices used to achieve electromechanical energy conversion, which play an important role in modern industries and have a broad power range from mWs to MWs. In recent years, with the ever increasing concerns on energy crisis and environmental pollution, electrical machines are becoming especially popular in clean energy systems, such as electric vehicles (EVs)/hybrid electric vehicles (HEVs), wind power generation system and tidal energy conversion system. Since electrical machines can greatly benefit the industrial intelligence, and electrical energy is renewable with zero emission, it is foreseeable that the utilization of electrical machines will continue to increase.

One of the important branches of electrical machines is the low-speed large-torque machines, which generally used in direct-drive applications. Technical requirements of such machines include:

a) Large torque density to realize direct drive;

b) Good flux controllability to achieve wide constant power speed range;

c) High efficiency over a wide operating range;

d) High reliability and mechanical robustness;

e) Acceptable material cost and manufacturing cost.

Permanent magnet (PM) machines can achieve high torque density and high efficiency especially when high magnetic energy magnets are used. Since the appearance of co-axial magnetic gear, flux-modulated PM machines have been widely studied and considered as promising candidates for direct-drive applications due to the incorporated gear effect. Compared with traditional surface/interior PM machines, flux-modulated PM machines can further increase the torque capability. When the flux-modulated PM machines are designed with hybrid excitations, good flux controllability can be achieved and the machines can maintain constant power operation over a wide speed range when work as motor, and output constant voltage when work as generator, which can reduce the impact to the power electronic converter. Therefore, the research work in this thesis is to investigate flux-controllable flux-modulated (FCFM) machines, from the principle, novel machine concepts to performance analysis and applications.

1.2 REVIEW OF FLUX-CONTROLLABLE MACHINES

According to the types of excitation sources and flux controlling methods, the flux-controllable machines can be divided into three categories, namely, electrically excited machines (EEMs), hybrid excited machines (HEMs) and memory machines (MMs). EEMs are only excited by field windings, continuous excitation currents are needed during the whole operating range, the flux regulating is achieved by directly controlling the excitation currents. HEMs are excited by both the field windings and PMs with high coercivity, continuous excitation currents are needed during flux regulating. MMs are excited by PMs with low coercivity and nonlinear hysteresis loops, the flux regulating can be achieved by applying current pulses. The equivalent circuit model of EEMs, HEMs and MMs in *d*-*q* frame is shown in Fig. 1.1.

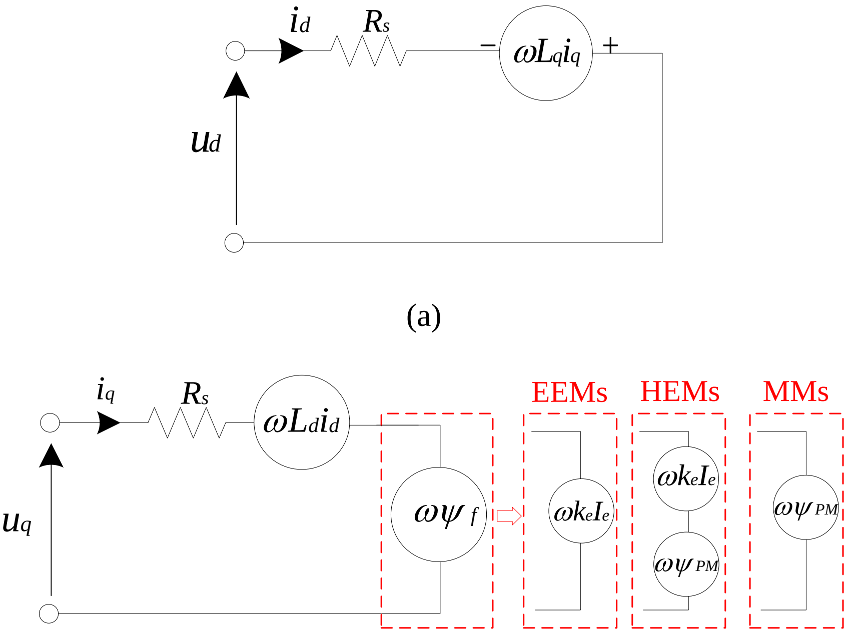

(a)

(b)

Figure 1.1 Equivalent circuit model. (a) d-axis equivalent circuit. (b) q-axis equivalent circuit.

where $i_{d,q}$, $u_{d,q}$, $L_{d,q}$ are the *d*-*q* axis current, voltage and inductance, respectively. I_e and k_e are the excitation current and mutual inductance between excitation coil and armature coil, respectively. ψ_f is the total excitation flux linkage and ψ_{PM} is PM flux linkage. ω and R_s refer to rotor speed and phase resistance of armature coil. The back EMF vector can be obtained by differentiate the flux linkage vector:

$$\vec{e} = -\frac{d\vec{\psi}_f}{dt} = \omega\psi_f \begin{bmatrix} \sin(\theta) \\ \sin(\theta - 2\pi/3) \\ \sin(\theta + 2\pi/3) \end{bmatrix} \tag{1.1}$$

One can find that the excitation flux can act as a regulator for the back EMF.

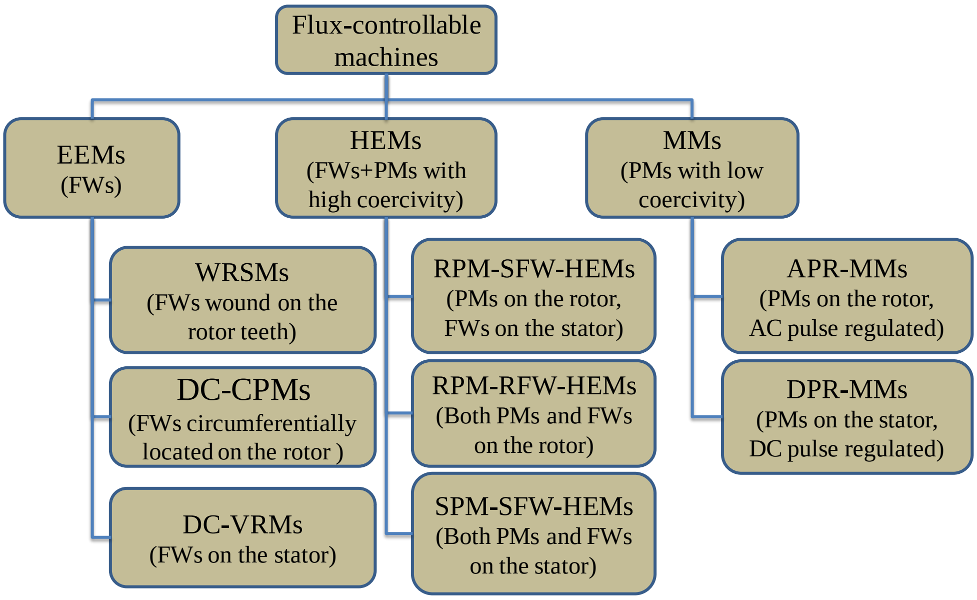

Figure 1.2 Classification of flux-controllable machines.

Based on the location of excitation sources, each group can be further classified into several subgroups. EEMs can be divided into wound rotor synchronous machines (WRSMs)with the field windings wound on the rotor teeth, DC excited claw-pole machines (DC-CPMs)with field windings circumferentially located on claw-pole rotor, and DC excited variable reluctance machines (DC-VRMs) with the field windings on the stator. HEMs can also be divided into three subgroups, which are the rotor-PM stator-field-winding HEMs (RPM-SFW-HEMs) which have the PMs located on the rotor while the field windings located on the stator, the rotor-PM rotor-field-winding HEMs (RPM-RFW-HEMs) which have both PMs and field windings on the rotor, and the stator-PM stator-field-winding HEMs (SPM-SFW-HEMs) which have both PMs and field windings on the stator. MMs can be divided into the AC pulse regulated MMs (APR-MMs) in which the PMs are located on the rotor and the magnetizing/demagnetizing is achieved by applying AC current pulse, and DC pulse regulated MMs (DPR-MMs) in which the PMs are located on the stator and the magnetizing/demagnetizing is realized by applying DC current pulse. The detailed classification of flux-controllable machines is shown in Fig. 1.2.

1.2.1 Electrically excited machines

Although PM machines usually have high torque density and high efficiency, they are not always preferable choices especially when wide constant power speed range (CPSR) are needed due to their fixed PM excitations. Other drawbacks such as weak mechanical strength and low heat resistance of PM materials also limit the usage of PM machines. EEMs can well solve the aforementioned problems. The air-gap flux can be regulated readily by adjusting the excitation current, and hence guarantee wide CPSR. Moreover, since the rare-earth magnets are only owned by a small part of countries and sale at a high price, EEMs are becoming increasingly attractive and show good potential in certain applications.

1.2.1.1 Wound rotor synchronous machines

Traditional WRSMs have been used in applications like EV propulsion [1, 2]for many decades. Despite the price advantage over PM machines, WRSMs can achieve wider CPSR due to their flexible flux controllability by simply adjusting the excitation current. A WRSM is proposed for EV traction which owns high overload capability at low speed and wide speed range at constant power[3].

One of the main drawbacks of traditional WRSMs is their bad thermal conditions. The temperature distributions in both WRSMs and PM machines are calculated and compared using the same cooling condition in[4]. The results show that WRSMs have higher winding temperatures than PM machines, especially the field winding temperature. This is because the field windings of WRSMs will produce continuous excitation loss, and rotor cooling is more difficult than stator cooling. Hence in real applications, WRSMs are more likely to compromise the torque density to meet the thermal constrains. Other comparisons between WRSMs and PM machines are reported in[5, 6].To provide sufficient flux intensity, the WRSMs should also employ enough field windings on the rotor. A spoke type of winding is proposed to maximize the copper area [1], which results in a considerable higher rotor copper loss than the stator copper loss and reduced efficiency. In[7], various operational envelops and efficiency maps of a WRS machine are calculated and analyzed. It shows that the copper and iron losses in the high-speed region are much higher than the losses at low speed.

Besides the high copper loss, reduced efficiency and difficult rotor cooling, the WRSMs also require slip rings or brushes as the excitation coils are located on the rotor, which will further reduce the machine efficiency and stability. Therefore, moving field excitation to the stator where cooling can be more effective, and the use of slip rings can be eliminated, is a more reasonable design choice.

1.2.1.2 DC excited claw-pole machines

The claw-pole machines are widely used as generators in vehicles. Generally, DC excited claw-pole machines (DC-CPM) have three parts, the claw-pole rotor, the field coil and the stator, as shown in Fig. 1.3. The magnetic flux produced by the field coils will pass through the rotor yoke, rotor claw-pole, the air-gap between the rotor and stator, the stator, then back to the air-gap between the rotor and stator, the adjacent rotor claw-pole and close at the rotor yoke. The prominent merits of DC-CPM are the low cost and easy manufacture since the claw-pole rotors are made by mold, which have great advantage over the laminated structure when produced in large scale. However, since the pole shape is not symmetrical along rotor axis, 3-D flux distribution is produced in the machine which requires 3-D magnetic field analysis [8, 9]. FEMs are more effective due to the special shape of claws, high saturation and the effects of flux leakage.

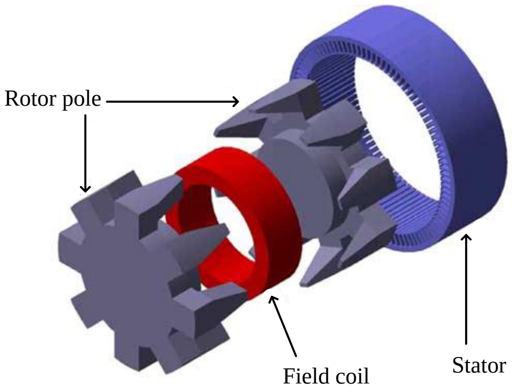

Figure 1.3 Configuration of DC-CPM [8].

Different magnetic materials are investigated to improve the performances of DC-CPMs [10-12]. The results show that using novel soft magnetic composite (SMC) materials like AFK502 which are more effective in terms of magnetic loss, permeability and magnetic saturation can reduce the machine dimensions and improve the power density. As the excitation coils are circumferentially located on the rotor in DC-CPMs, brushes or slip rings are inevitably needed. The excitation current is also limited due to the magnetic saturation, which reduces the torque density of DC-CPMs. Therefore, claw-pole machines with PM excitations and hybrid excitations when field adjustment is needed are widely investigated [13-17], which will be further discussed in HEMs.

1.2.1.3 DC excited variable reluctance machines

DC-VRM is a novel machine concept which moves the excitation coils to the stator. A robust rotor structure similar to that of switched reluctance machine (SRM) is applicable for DC-VRM. Slip rings are not needed and the cooling efficiency is improved as the excitation coils are employed on the stator. The same as other EEMs, DC-VRMs can online adjust the air-gap flux simply by controlling the DC excitation currents.

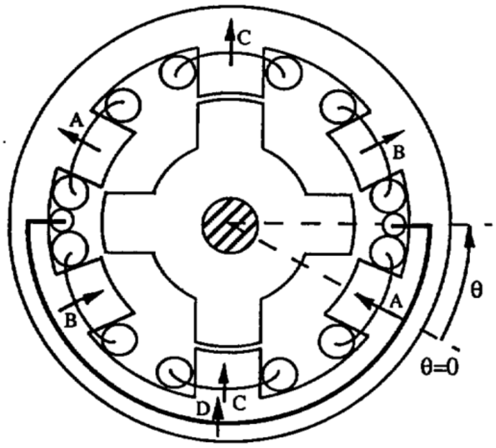

Figure 1.4 The structure and winding connection of 6/4 DFDSM [18].

Fig. 1.4 shows one typical DC-VRM configuration with 6/4 stator/rotor poles, which was first proposed in[18] and also referred as doubly fed doubly salient machine (DFDSM) in the later research [19-23].The original intension of this DFDSM is to deal with the current commutation and energy circulation problems of SRM[18].Compared with SRMs, the output power of this DFDSM can increase 11 percent in the constant torque operation region and increase from 14 percent to 20 percent in the constant power operating region without a marked reduction in the efficiency. The CPSR can also be significantly extended by simply tuning the field current[22].

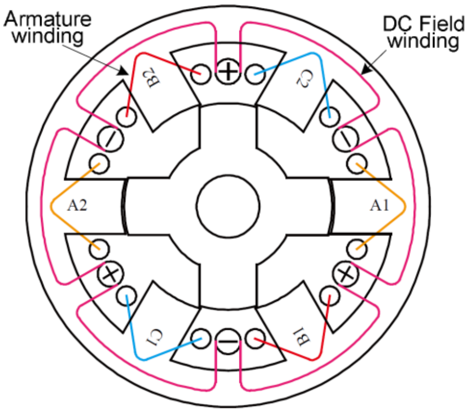

Figure 1.5 Novel DFDSM excited by sinusoidal excitation with DC bias [24].

A novel DFDSM is proposed as shown in Fig. 1.5 [24], which is excited by bipolar sinusoidal excitation with DC bias. Since the field winding in this novel DFDSM is identically located for each phase, symmetric flux distribution can be achieved, and the current requirement for the field winding is reduced due to the short flux path. On the other hand, the symmetric flux distribution can also help to produce identical back-EMF for all phases, which can reduce the torque ripple as well as the vibration and acoustic noise. Compared with traditional SPMs with bipolar sinusoidal excitation, the novel DFDSM can achieve much higher torque density. The back-EMF can also be regulated through field current adjustment[25].

1.2.2 Hybrid excited machines

HEMs are those which employ both a primary PM excitation and a secondary field coil excitation source, and can be regarded as combinations of PM machines and EEMs. Good flux regulating capability can be achieved while high torque density and high efficiency can still be maintained. Therefore, HEMs have good potential to be used in applications where high torque density and high efficiency as well as wide CPSR are needed.

Many HEM topologies have been reported in existing literatures. Generally, there are two clarification methods for HEMs: 1) Concerning the magnetic circuits of the two excitation sources, HEMs can be grouped as series HEMs, in which the flux lines excited by the field coils pass through the PMs, and parallel HEMs, in which the flux lines of field coils don't pass through the PMs. 2) According to the location of excitation sources, HEMs can be grouped into three categories, those are RPM-SFW-HEMs with PMs on the rotor while field coils on the stator, RPM-RFW-HEMs which have both PMs and field coils on the rotor, and SPM-SFW-HEMs which have both PMs and field coils on the stator. In this thesis, the second one is used to group the HEMs.

1.2.2.1 HEMs with PMs on the rotor while coils on the stator

Lots of HEMs belong to this group. By employing PMs on the rotor, RPM-SFW-HEMs have good potential to realize high torque density. Slip rings or brushes are not needed as the excitation coils are located on the stator.

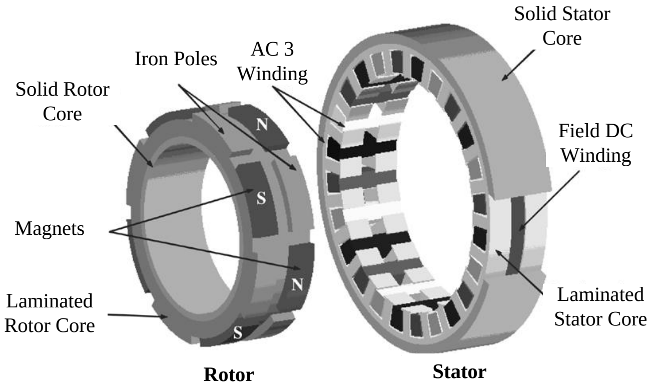

Figure 1.6 Configuration of the CPPM machine [26].

Consequent-pole PM (CPPM) machine [26]is a typical configuration in this category, which is shown in Fig. 1.6. The rotor of this machine is divided into two sections, one has partial radially magnetized surface mounted PMs, while the other has a laminated iron pole. A circumferential field winding is placed in the middle of the stator to achieve flux regulation. A wide CPSR can be achieved by controlling the excitation field current without demagnetization risk for the PM pieces. However, the power density of this machine is reduced since the additional DC windings reduce the inner diameter of the stator if the machine outer diameter is kept unchanged. Moreover, the air-gap associated to the DC winding section will not participate in the energy conversion process.

Some other HEMs with PMs on the rotor while field coils on the stator are also studied. Through employing PMs on the rotor of DC excited vernier machine, a novel hybrid excited vernier machine can be resulted [27, 28]. This machine can easily achieve high output torque at low speed operation and good flux weakening capability at high speed operation.

1.2.2.2 HEMs with both PMs and field coils on the rotor

To achieve brushless structures, most HEMs locate the field coils in the stator. Only few HEMs employ both PM excitation and field coils on the rotor. Fig. 1.7 shows the configuration of a RPM-RFW-HEM[29] , in which the rotor is employed with both surface mounted PMs and a wound field coil. Compared with the aforementioned HEM topologies, this machine has relatively simple structure. However, undesirable torque pulsations and vibration may be generated due to the space and time harmonic components. The use of brush or slip-ring will also reduce the machine's reliability. Similar structure is reported in[30], the rotor pole number can be changed when the direction of DC current changes. Another RPM-RFW-HEM is reported in[31], in which the rotor is divided into two parts, one for excitation coils and the other for PMs. Claw pole HEM with both excitations in the rotor is also studied in [32].

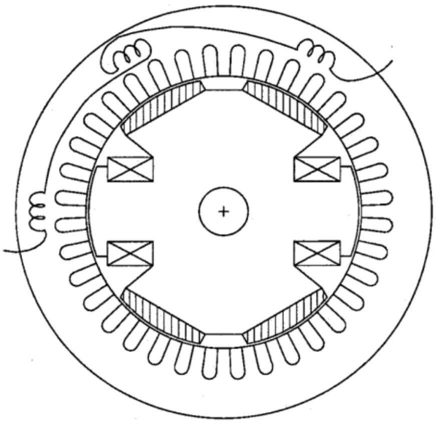

Figure 1.7 Configuration of hybrid-excited PM machine with both excitation sources on the rotor [29].

1.2.2.3 HEMs with both PMs and field coils on the stator

Among all the HEMs, the SPM-SFW-HEMs are the most popular ones because all excitations are located on the stator, a robust rotor structure can be achieved, which are very suitable for high speed operation. The drawbacks of SPM-SFW-HEMs are the relatively complicated stator structures and reduced torque density compared with the rotor PM excited machines. Generally, the SPM-SFW-HEMs contain two machine types, namely, hybrid excited doubly salient machines (HEDSMs) and hybrid excited flux switching machines (HEFSMs). Similar to the rotor PM hybrid excited vernier machines (RPM-HEVMs), the PMs can also be employed on the stator, which are named as stator PM HEVMs (SPM-HEVMs).

Fig. 1.8 shows several HEDSM topologies in which the flux lines of field windings and PMs are in series. For the machine shown in Fig. 1.8(a) [33], the PMs are radially magnetized. As the flux excited by the field windings would pass through the large reluctance PMs, big DC exciting power is needed to realize good flux regulation, which would reduce the machine efficiency and also bring risk of PM demagnetization. A new HEDSM employs magnetic bridges as low reluctance paths for the flux generated by the field windings [34, 35], is shown in Fig. 1.8 (b). The magnetic bridges can greatly reduce the required field exciting ampere-turns. However, it also belongs to the series HEMs, and the magnetic saturation has big influence on the reluctance of magnetic bridges. Another HEDSM which uses air bridges to realize the same features of the magnetic bridges [36], is shown in Fig. 1.8 (c). The difference is that the reluctance of air bridges is invariant and will not be influenced by magnet saturation. Comparative study in [37] show that topology in Fig. 1.8 (a) is hard to fabricated due to the separated stator lamination. And the topology with air bridges in Fig. 1.8 (c) can well reduce the risk of demagnetization of PMs.

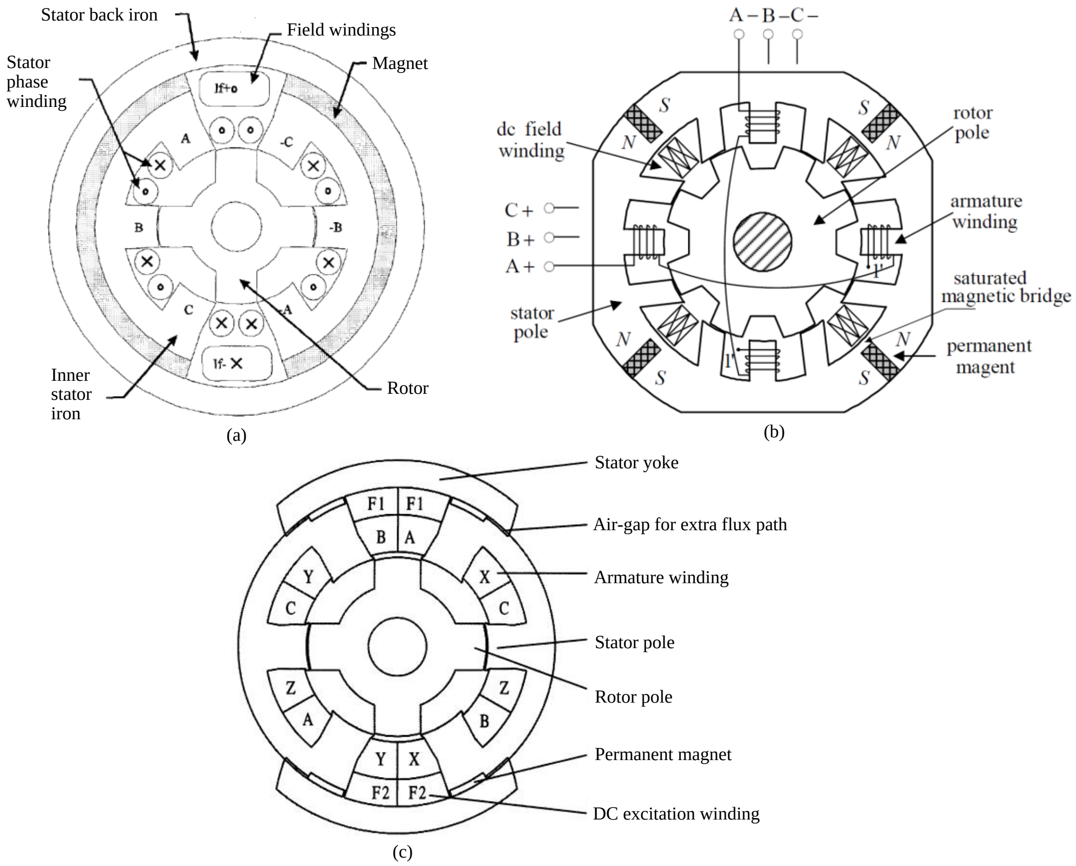

Figure 1.8 Configuration of series HEDSMs. (a) Primary topology [33]. (b) HEDSM with magnetic bridges [34]. (c) HEDSM with air bridges [36].

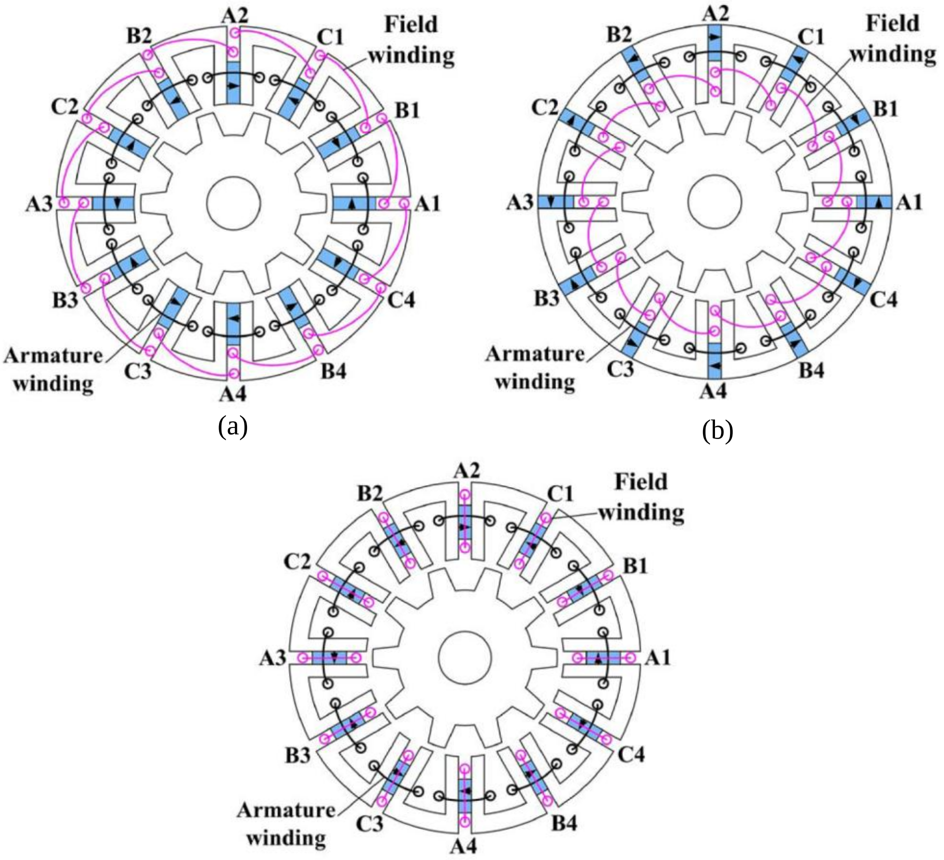

(a) (b)

(c)

Figure 1.9 Configurations of HEFSMs [38]. (a) PM-Top. (b) PM-Bottom. (c) PM-Middle.

HEFSMs were proposed based on the FSPM machines, by shortening the length of PMs in an original FSPM machines while introducing an additional set of field windings into the saved place. The PMs can be located in the top or bottom or middle of the stator slots, which are referred as PM-Top, PM-Bottom and PM-Middle topologies in[38] and shown in Fig. 1.9 (a)-(c), respectively. The PM-Middle topology owns the weakest flux regulation capability since the currents in the two slots adjoining each magnet exhibit reversal hybrid excitation results. This issue can be efficiently improved by artfully reconnecting the field windings [39].

The current direction in one of the slots is reversed while the motor structure is kept identical. The improved machine has much better regulating capability of no-load flux and output torque. Since the flux of PMs and excitation coils are in series, the magnetic circuit excited by field windings owns relatively high reluctance due to the low permeability of PMs, which limits the flux regulating capability. Moreover, the PMs also have higher risk of demagnetization. Iron flux bridges are used to overcome the aforementioned drawbacks [40]. The field excitation can be effectively increased through adding iron bridges at the outer radius of the machine, with the tradeoff of slightly reduced torque density. Even with iron flux bridges, the excitation current utilization ratio is limited due to the magnetic saturation. The PM flux short-circuit also occurs which further increase the saturation and reduce the efficiency.

Parallel HEFSM with two-part rotor (PHEFSM-T) is proposed in [41].By flexibly allocating the axial length of the two parts, the required flux adjusting capability and torque density can be achieved. The excitation current utilization ratio is improved while the excitation loss is reduced compared with the series HEFSMs. Another PHEFSM with E-core stator (PHEFSM-E) is reported in [42]. Compared with the PHEFSM-T, the PHEFSM-E has relatively simple structure but low excitation current utilization ratio since high saturation are observed in the stator yoke, the stator tooth, the middle tooth of E-core and the rotor tooth caused by the PM flux [43]. The flux regulation ability among series hybrid excited flux switching

(SHEFS) machine with and without air bridges, PHEFSM-T and PHEFSM-E is given in Fig. 1.10. The results show that air bridges can significantly improve the flux regulating ability of SHEFS machine. And the PHEFSM-T enjoys the increased flux regulating range.

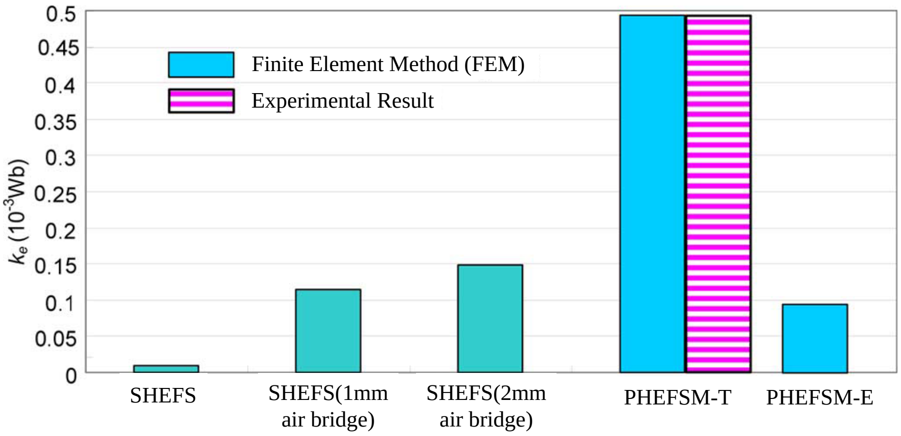

Figure 1.10 Comparison of flux regulating ability among SHEFS, PHEFSM-T and PHEFSM-E [43].

1.2.3 Memory machines

MMs are relatively new machine concepts which were firstly proposed in [44]. The key is to use PMs with both low coercivity and nonlinear hysteresis loop, such as AlNiCo PMs. On the one hand, the nonlinear demagnetization characteristic ensures the recoil line never superpose on the demagnetization curve. Once the demagnetization current is applied and then removed when flux weakening is needed, the working point of AlNiCo PM will move along the recoil line and settle at a lower magnetization level, which means that the magnetization level is memorized. Therefore, for MMs, there is no need to apply continuous excitation current during flux weakening, only current pulse is needed since the magnetization level of

AlNiCo PM will not change if no other magnetizing/demagnetizing current is applied, which will greatly reduce the copper loss and hence improve efficiency.

MMs can be grouped into two categories based on the magnetizing/demagnetizing method, namely, APR-MMs when the PMs are located on the rotor and the magnetizing/demagnetizing is achieved by applying AC current pulse, and DPR-MMs when the PMs are located on the stator and the magnetizing/demagnetizing is realized by applying DC current.

1.2.3.1 MMs with AC pulse regulation

In APR-MMs, the AlNiCo PMs are located on the rotor, usually with sandwiched structure as shown in Fig. 1.11 [44, 45]. The stator is the same as that of a traditional PM synchronous machine. During flux weakening operation, a negative d-axis current pulse is generated through controlling the armature currents. This kind of machine is easy to fabricate due to the relatively simple structure, but the control process is complicated. The demagnetization physics are investigated using coupled Preisach modeling and FEM [46, 47].

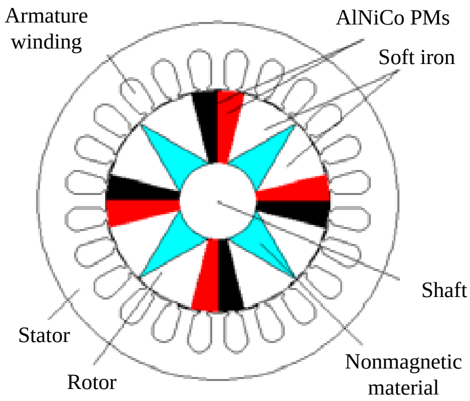

Figure 1.11 Configuration of a primary APR-MM [44].

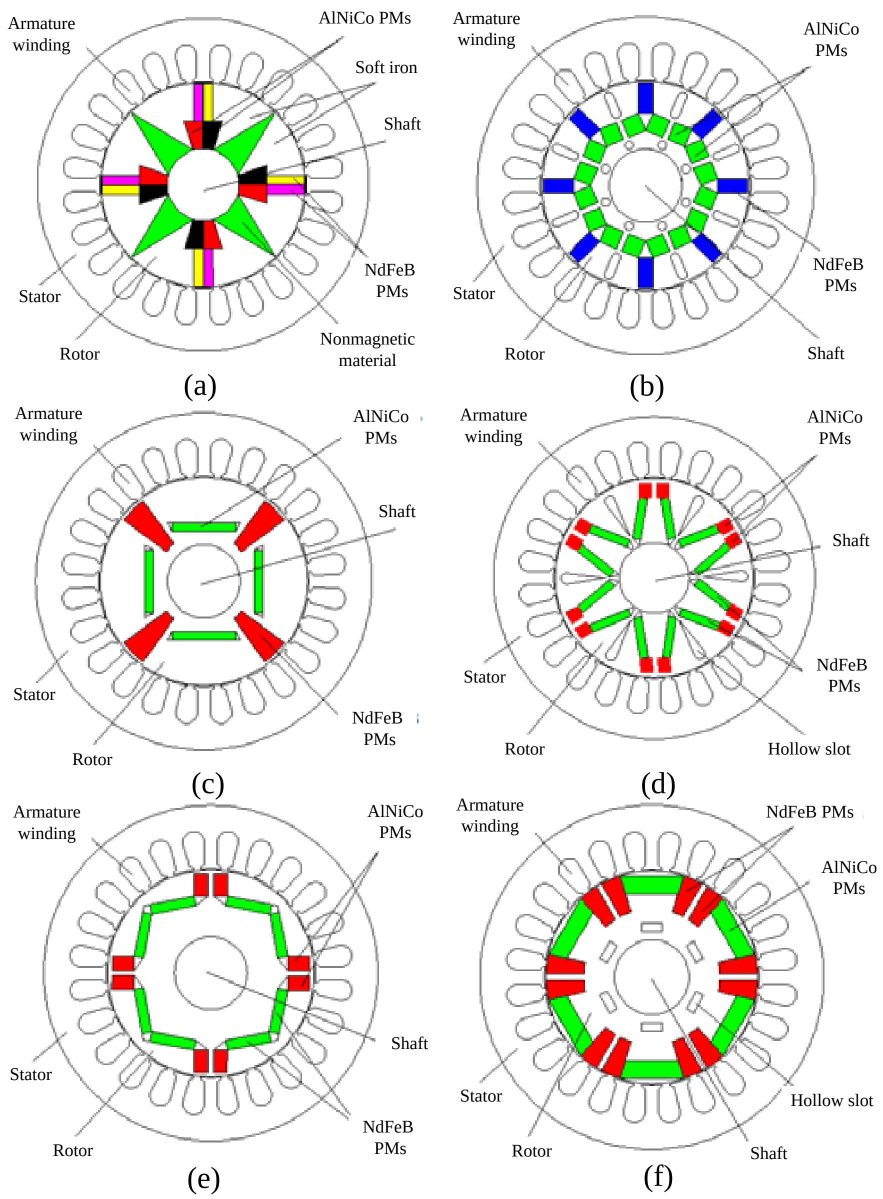

Figure 1.12 Configurations of hybrid excited APR-MMs. (a) Linear type. (b) Y-type. (c) U-type. (d) V-type. (e) W-type. (f) Halbach type.

APR-MMs with both AlNiCo and NdFeB are proposed as shown in Fig. 1.12 (a)-(f) [48-53]. The high magnetic energy NdFeB PMs are used to increase the air-gap flux density, while the AlNiCo PMs are used for online flux regulation. Therefore, the machine can enjoy both high output torque during low speed operation and good flux weakening capability at constant power region. All the aforementioned MMs use d-axis current pulse to realize flux regulation. To produce enough magnetizing/demagnetizing current, the armature windings should be able to suffer large current and with sufficient turns. Accurate detection of rotor position is also needed to realize efficient flux regulation.

1.2.3.2 MMs with DC pulse regulation

To achieve the magnetizing/demagnetizing process more easily, the DPR-MMs were proposed which use DC current pulse to realize magnetizing/demagnetizing. Fig. 1.13 (a) shows a typical structure of DPR-MMs, in which the stator is divided into two parts [54-56]. The AlNiCo PMs and field windings are located in the inner layer stator, while the armature windings are housed in the outer layer stator slots. The use of field windings to directly magnetizing/demagnetizing PMs while eliminating complicated indirect current control in APR-MMs can ensure effective flux regulation. Moreover, the armature windings and PMs are located in different lays of stator, which make the PMs immune from accidental demagnetization by armature reaction. Similar to the APR-MMs, as the AlNiCo PMs own relatively low magnetic energy than the NdFeB PMs, hybrid DPR-MMs with both AlNiCo and NdFeB excitations are proposed in[57-59], as shown in Fig. 1.13 (b). The torque density of the proposed machines are improved while still maintaining good flux regulating capability. By applying demagnetizing current to certain poles, the flux lines of corresponding poles can be short circuited or even reversed, which can achieve pole-changing operation [60, 61]. This ability can provide torque augment by dropping poles when the machine speed approaches to the limit.

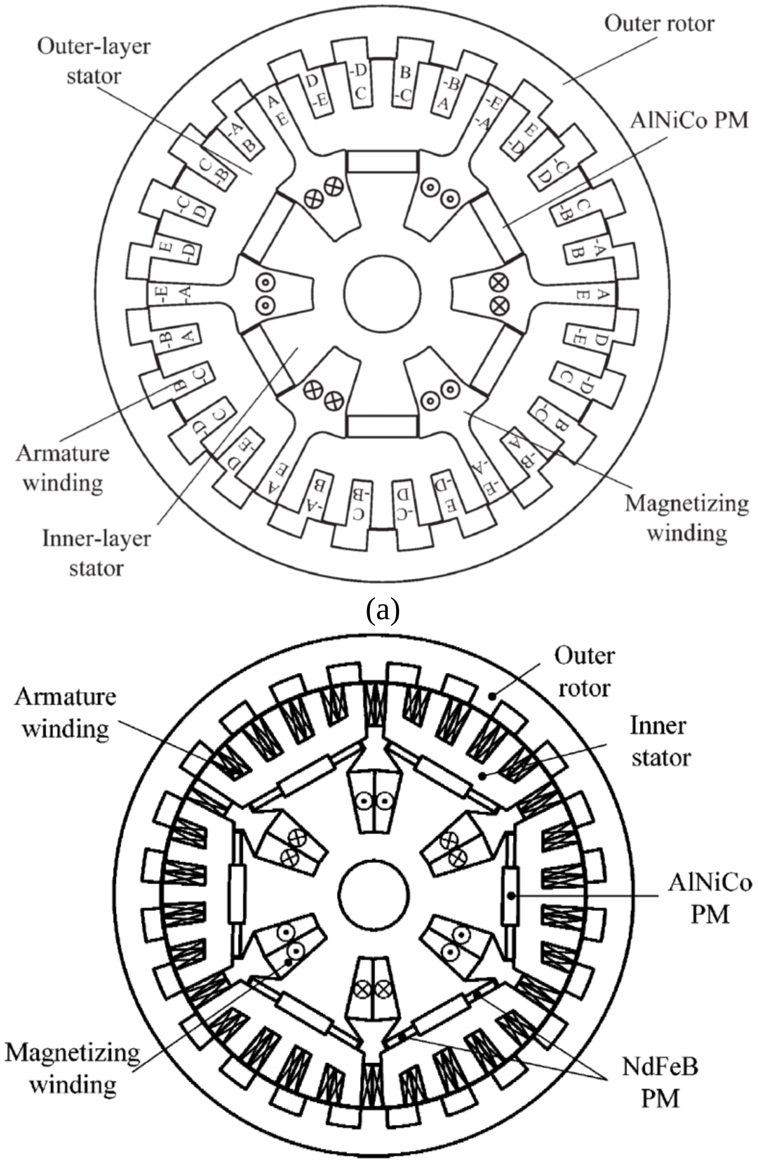

(a)

(b)

Figure 1.13 Configuration of DPR-MMs. (a) AlNiCo excited [54]. (b) AlNiCo and NdFeB excited [57].

Inspired by the configuration in Fig. 1.13, a new doubly salient flux-mnemonic machine is proposed [62, 63], which enjoys significantly expanded CPSR and increased efficiency with online flux control. With the increasing popularity of magnetic gear, magnetic-geared machines incorporated into flux-mnemonic concept [64-66] are also investigated by researchers. These machines can enjoy big torque density due to the magnetic gearing effect. But the mechanical structures are relatively complicated as there usually exist two air-gaps. The comparison between APR-MMs and DPR-MMs are summarized and given in Table 1.1.

Table 1.1 Comparison between APR-MMs and DPR-MMs

Items	APR-MMs	DPR-MMs
PM material	AlNiCo	AlNiCo
Torque density	Medium	Medium
Efficiency	High	High
Magnetizing/demagnetizing windings	Don't need	Need
Rotor robustness	Medium	Good
Rotor position sensor	Yes	No
Control	Difficult	Easy

1.3 REVIEW OF FLUX-MODULATED MACHINES

Flux-modulated machines are promising candidates to achieve high torque density. One of the outstanding features of flux modulated machine is that, the pole-pair number (PPN) of the stator and rotor can be designed different. Gear effect can be realized in flux-modulated machines which can contribute to torque improvement. Since the appearance of co-axial magnetic gear, various flux-modulated machines have been proposed. Here, the magnetic-geared machines, vernier PM machines and electrical continuously variable transmission (E-CVT) systems are reviewed.

1.3.1 Magnetic-geared machines

By directly connecting the outer rotor of a PM machine and the inner rotor of a MG, a MG integrated PM machine is invented[67], as shown in Fig. 1.14(a). The electromagnetic torque generated by the PM machine can be amplified, and the inner cave space of the MG can be fully utilized, and therefore this MG integrated PM machine can achieve very high torque density. The applications in EV propulsion and wind power generation are separately reported in [67] and [68], respectively. The major drawback of this MG integrated PM machine is its complicated mechanical structure. As can be seen from Fig. 1.14(a), there are three air-gaps in this MG integrated PM machine, which makes it very difficult to assemble. Fig. 1.14(b) shows another configuration of magnetic-geared machine[69], in which the outer rotor of PM machine and inner rotor of MG in Fig. 1.14(a) are eliminated. The armature field is directly coupled with the PM excitation field modulated by the modulation ring. This magnetic-geared machine has just one PM layer, therefore is referred as single-layer magnetic-geared PM(SL-MGPM) machine, and it can also be regarded as replacing the inner rotor of MG with a stator. Compared with the MG integrated PM machine shown in Fig. 1.14(a), the SL-MGPM machine in Fig. 1.14(b) has much simpler structure and is easy to manufacture.

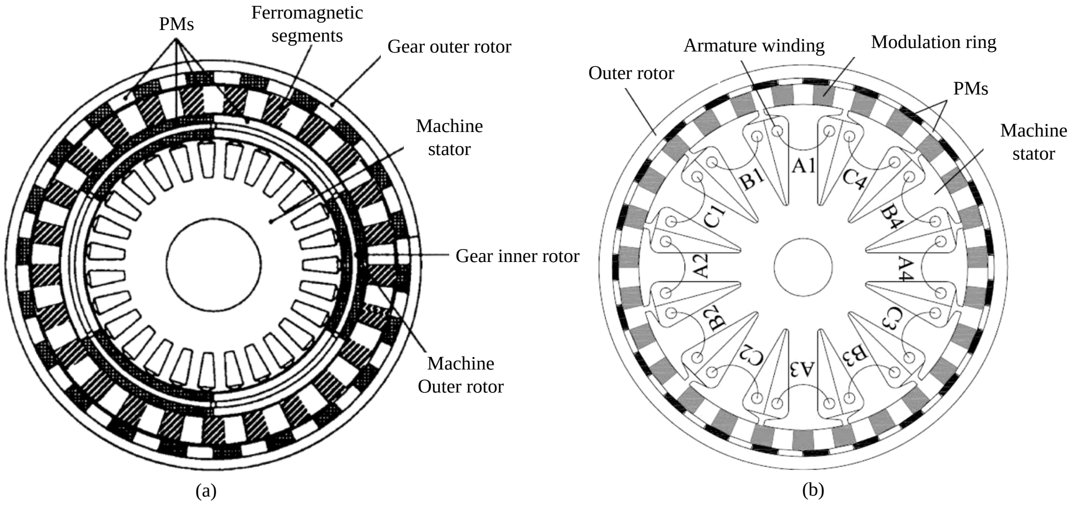

Figure 1.14 Configurations of magnetic-geared machines. (a) MG integrated PM machine[67]. (b) SL-MGPM machine[69].

The concept of MG can be further extended to linear machines. Through integrating a tubular linear PM (TLPM) machine and a tubular linear MG(TLMG), a TLMG integrated PM machine[70] is constructed as shown in Fig. 1.15(a). The principle of this TLMG integrated PM machine is very similar to that of the magnetic-geared machine shown in Fig. 1.14(a), and can be used in tidal energy conversion. The TLPM machine can be designed with high power density, and its thrust force can be amplified by the TLMG. The major drawback of this TLMG integrated PM machine is its complicated structure. Fig. 1.15(b) shows another configuration of the tubular linear magnetic-geared machine with sandwiched stator, which is referred as sandwiched stator tubular linear magnetic-geared(SS-TLMG) machine[71]. The stator housed with windings is sandwiched between the high-speed mover and low-speed mover. The high-speed mover and the stator work as a linear PM machine, while the high-speed mover, the stator and the low-speed mover function like a linear MG. Compared with the TLMG integrated PM machine shown in Fig. 1.15(a), the structure of the SS-TLMG machine shown in Fig. 1.15(b) is more compact and simple, and thus improved force density.

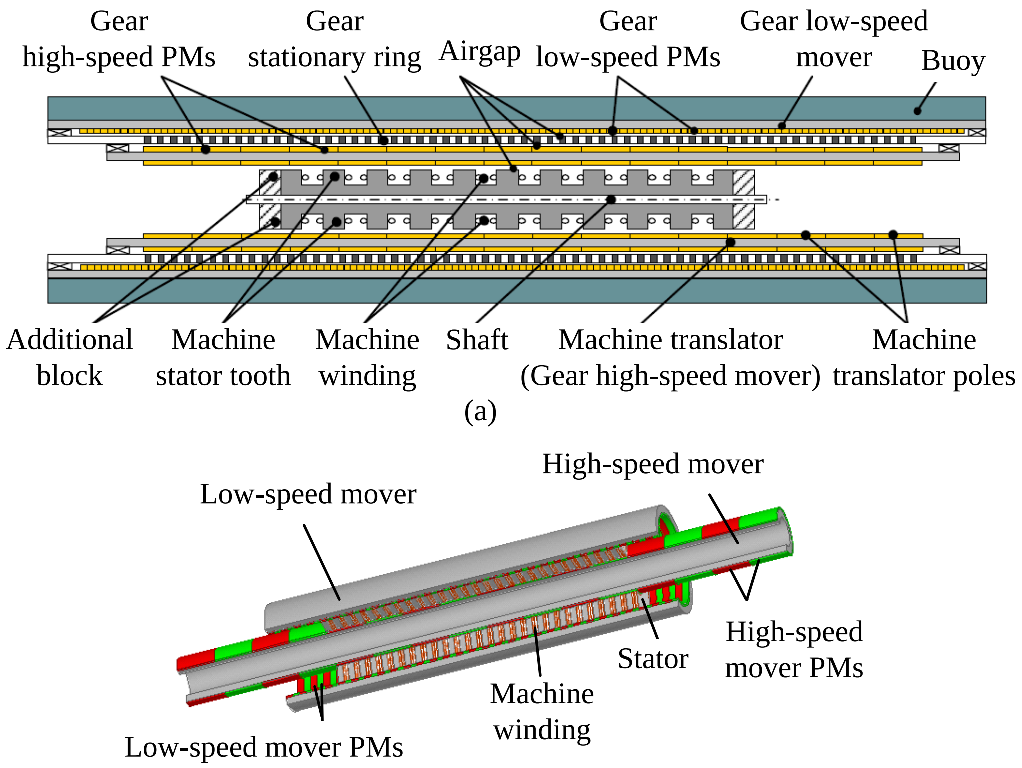

(a)

(b)

Figure 1.15 Configurations of linear magnetic-geared machines. (a) TLMG integrated PM machine[70]. (b) SS-TLMG machine[71].

1.3.2 Vernier PM machines

Vernier PM machines have attracted much attention in direct-drive applications and are recognized as good candidates to achieve high torque density due to the magnetic gearing effect. The half-cross-sectional view of the original vernier PM machine is shown in Fig. 1.16, which has simple structure. The PMs are surface mounted on the rotor, and the windings are housed in the stator slots. The stator is designed with open slots, which can function as the modulation segments in a MG and provide magnetic gearing effect. The PPN of armature winding p_a , PPN of rotor PMs p_o and stator slot number N_s are governed by

$$N_s = p_i + p_o \tag{1.2}$$

which is similar to the working principle of MG. The design and operating principle of vernier PM machine are analytically investigated in[72]. One of the major drawbacks of vernier PM machine is low power factor caused by heavy magnet flux leakage and low magnet utilization. Therefore, large-capacity converter is needed to drive the low-power-factor vernier PM machine, which will result in high cost.

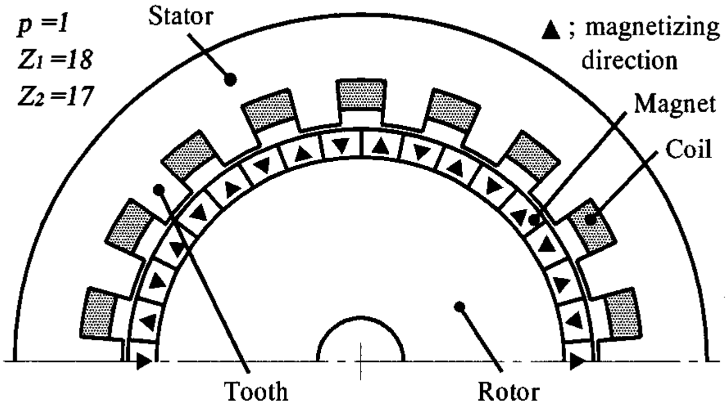

Figure 1.16 Configuration of the original vernier PM machine [73].

A new vernier PM topology which can overcome the shortcoming of low power factor of conventional vernier PM machines is proposed[74], as shown in Fig. 1.17. The novelty of this structure is that the inner stator teeth and outer stator teeth are displaced with half teeth pitch, and therefore the inner and outer teeth can compensate with each other. The leakage flux can be greatly reduced and the power factor is improved accordingly.

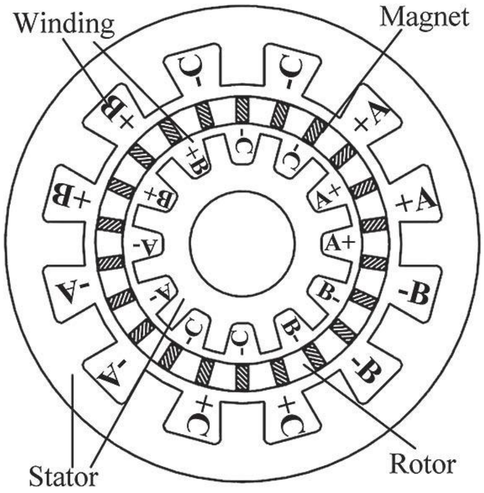

Figure 1.17 Configuration of vernier PM machine with high power factor[74].

1.3.3 E-CVT systems

E-CVT system is an important component and core technology in HEVs, which is a power-splitting unit. The energy flow among the internal combustion engine (ICE) and other energy sources, which usually are electrical machines, can be flexibly combined or split according to different operation requirements. Therefore, the ICE can operate at optimal conditions when the vehicle speed varies, the efficiency of the ICE is increased and the fuel economy of HEVs is improved consequently. One of the most popular and commercialized E-CVT is the one used in Toyota Prius, which is based on the planetary gear. Two sets of electrical machine systems are used, which can be separately controlled and are connected to the sun gear and ring gear, respectively. The crank shaft of ICE is linked to the planetary carrier. During start-up or climbing, the electrical machine will work as motor to help the ICE drive the vehicle. While during braking or downhill, when the output power of ICE exceeds the requirement of vehicle, the surplus power of ICE can be stored in the battery and the electrical machines are worked in generator mode in this case.

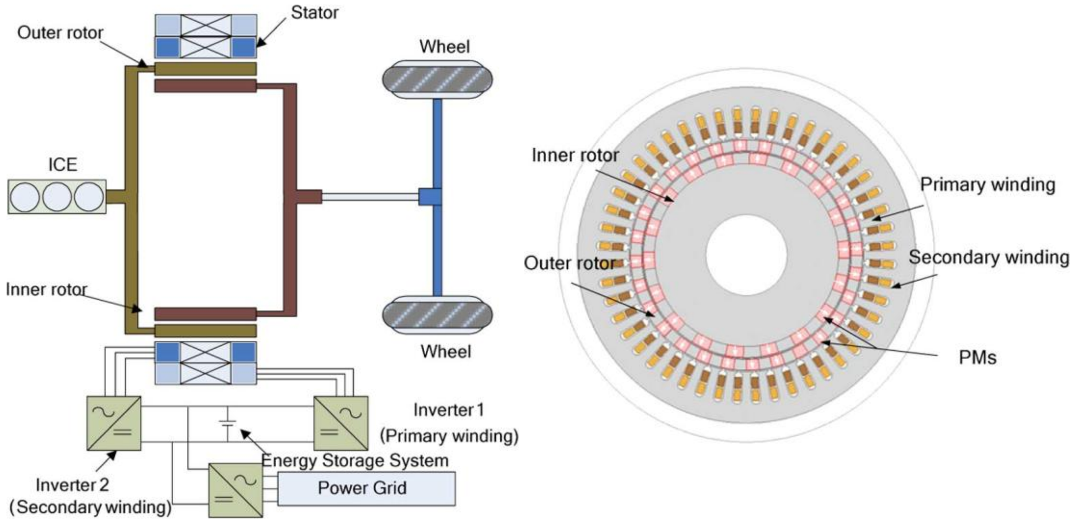

(a) (b)

Figure 1.18 Configuration of the DFDR-PM machine based E-CVT[75]. (a) E-CVT system. (b) DFDR-PM machine.

The Toyota Prius E-CVT system can well optimize the efficiency of ICE and reduce the fuel consumption, but the planetary gear still suffer from some mechanical drawbacks, such as friction, audible noise, and high maintenance. Moreover, the planetary gear based E-CVT system is also bulky and heavy due to its complex structure. Fig. 1.18 shows a novel E-CVT system based on flux modulating effect, which is called doubly-fed dual-rotor PM (DFDR-PM) machine based E-CVT system. The two electrical machines in the planetary gear based E-CVT system are combined into a single machine, namely, the novel DFDR-PM machine. Two rotors are employed, both of which consist of PMs and modulation segments. The inner rotor is linked to the crank shaft of ICE, and the outer rotor is connected to the drive shaft. There are two sets of windings housed in the stator slots, one is the primary winding and the other is secondary winding. The primary winding interacts with the two rotors through the flux modulating effect and form a dual-rotor flux modulated machine, and the secondary winding interacts with the outer rotor and forms a normal PM machine. This DFDR-PM based E-CVT system can realize power split and combination effectively. Compared with the planetary gear based E-CVT, the DFDR-PM based E-CVT has compact structure and no mechanical frictions. Besides the application in HEVs as reported in[76], the DFDR-PM based E-CVT can also be used in variable speed wind power generation[77, 78].

1.4 RESEARCH OBJECTIVES

Although flux-controllable machines and flux-modulated machines have been widely investigated separately, there is no systematic research which combines these two kinds of machines together. The objectives of this research are to comprehensively investigate the FCFM machines, which mainly includes the following parts:

a) Establish analytical model of FCFM machines;
b) Come up with a general design method for FCFM machines;
c) Propose novel FCFM machine concepts;
d) Electromagnetic simulation of the proposed FCFM machine concepts;
e) Make prototypes and conduct experimental verification.

1.5 THESIS OUTLINE

There are seven chapters in this thesis, the first chapter is the introduction part and the last chapter gives the conclusions and recommendations. The contents of the rest chapters are described as follows:

In chapter two, dual-stator magnetic flux-modulated mnemonic machines are proposed. Hybrid PM excitation is employed to achieve both high torque density and good flux regulating capability. The machine configurations and mechanical structures are firstly described, and design principle is discussed based on flux modulating effect. The electromagnetic performances are investigated and compared using FEM.

In chapter three, the flux-modulated memory machine is designed with five phases, so as to achieve fault tolerant capability. The machine configuration is similar to the machines in chapter two. Fault tolerant capability is specifically studied, which includes one phase open circuit and two phases open circuit. The results show that the proposed five phase machine can work stably under open circuit condition.

In chapter four, hybrid-excited dual PM machine is proposed, which is a progress based on the machines in chapter two. The outer stator and inner stator in the machines in chapter two are incorporated into one stator, therefore the mechanical structure is simplified. The air-gap field harmonics are investigated in detail to illustrate the working principle. FEM is firstly used to investigate the electromagnetic performances. A prototype is made and experimental tests are conducted to verify the electromagnetic design.

In chapter five, a hybrid excited flux bidirectional modulated machine is proposed for wind power generation. Compare with the dual PM machine proposed in chapter four, stator PM is removed and large field current can be applied without suffering the demagnetization risk of magnets. Tabu search algorithm coupled with FEM is used to optimal design the proposed machine. Both constant voltage control and maximum power point tracking (MPPT) control are investigated. The electromagnetic performances are firstly analyzed using FEM and verified through experimental investigations.

In chapter six, DC-coil-free hybrid-excited machines (DCF-HEMs) are proposed, which integrate armature winding and field winding into one single winding. DC bias current is injected into the winding to realize flux regulation. Compared with traditional HEMs with additional field windings, the proposed DCF-HEMs can achieve both higher torque density and wider field regulating range. The electromagnetic performances are studied and compared using FEM. A prototype with dual PM is manufactured and experimental investigations are conducted to verify its electromagnetic design.

CHAPTER 2 DUAL-STATOR MAGNETIC FLUX-MODULATED MNEMONIC MACHINES

2.1 INTRODUCTION

As mentioned in the last chapter, traditional PM machines are good candidates to achieve high torque density design but suffer from weak flux regulating capability due to their fixed PM excitation, which limits the wide use of PM machines in traction applications. Most of the time, flux weakening operation is achieved by applying negative d-axis current, which requires accurate detection of rotor position and reduces the efficiency.

In this chapter, two novel magnetic flux-modulated mnemonic (MFMM) machines with different topologies are proposed. The two machines are, namely, the dual-layer PM MFMM (DPM-MFMM) machine with PMs on both the rotor and the outer stator, and the single-layer PM MFMM (SPM-MFMM) machine with all the PMs on the outer stator. Hybrid PM excitation with both NdFeB and AlNiCo are employed, which can simultaneously facilitate large output torque at low speed and high flux-weakening at high speed. Configurations and working principles of these two machines are discussed in details. The electromagnetic performances of these two machines are comprehensively studied and quantitatively compared using FEM.

2.2 CONFIGURATION AND STRUCTURE

2.2.1 Machine configuration

Fig. 2.1(a) shows the configuration of the DPM-MFMM machine. It consists of one rotor and two stators. One cup shaped rotor is located between the inner stator and outer stator. Two sets of consequent-pole PMs are employed, one on the rotor using NdFeB PMs, and the other one on the outer stator using both NdFeB PMs and AlNiCo PMs. Both rotor PMs and stator PMs are radially magnetized. Each PM and its adjacent iron tooth/ferromagnetic segment form a pair of magnetic poles. The armature windings and dc field windings are housed, respectively, in the inner stator slots and outer stator slots. Since AlNiCo magnet inherently has a low coercivity, the air-gap flux can be strengthened or weakened readily by the application of dc current pulse in the field windings. Fractional-slot distributed winding can be used to reduce the end windings but due to the flux modulation effects of the machine, there would be increased harmonics in the back-EMF. In this study, the single-layer integral-slot distributed winding (1 slot per pole per phase with coil span of 2) is being employed in the inner stator, as it has a unity winding factor and yields a sinusoidal back-EMF.

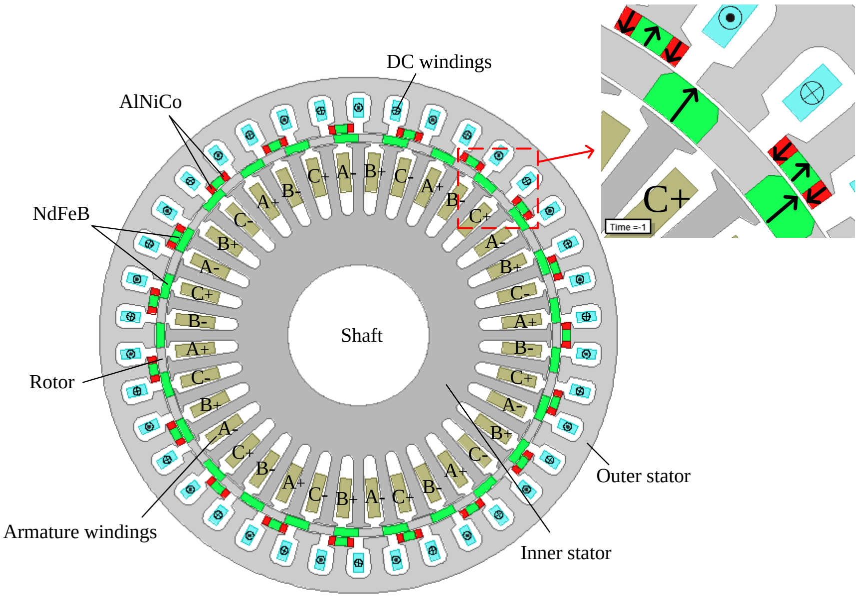

(a)

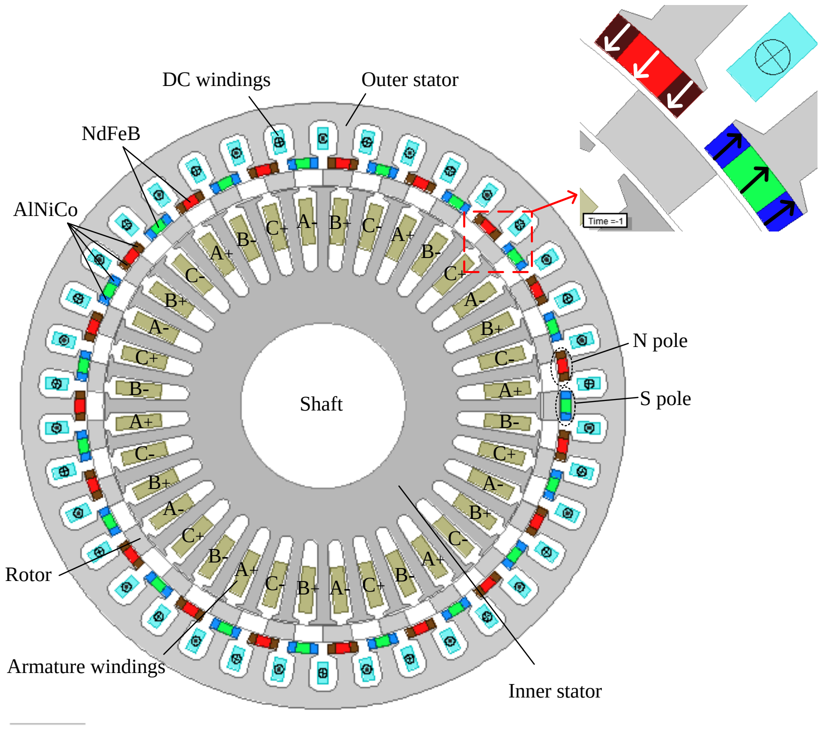

(b)

Figure 2.1 Configurations of the proposed machines. (a) DPM-MFMM machine. (b) SPM-MFMM machine.

Fig. 2.1(b) shows the configuration of the SPM-MFMM machine, which is also made up of three components, the inner stator, the outer stator and the rotor. Similar to the DPM-MFMM machine, both NdFeB magnets and AlNiCo magnets are employed on the outer stator, and dc windings are housed in the outer stator slots. With this design the air-gap flux can be regulated effectively with a dc field current pulse. The armature windings are located in the inner stator slots. The difference between the two machines is that this SPM-MFMM machine employs all the PMs on the outer stator, and the adjacent PMs are magnetized in opposite directions. As the rotor is only made up of ferromagnetic segments, the total amount of PMs in the

SPM-MFMM machine and DPM-MFMM machine are virtually the same.

2.2.2 Mechanical structure

The overall mechanical structures of the proposed two machines are almost the same, as shown in Fig. 2.2. The PMs on the outer stator are surface mounted using superglue. Since the rotor is sandwiched between the two stators, a cup rotor structure is artfully employed to facilitate the machine assembly. For the DPM-MFMM machine, PMs are glued inside the rotor slots. Since there exist big centrifugal forces when the rotor rotating at high speed, wedge structure is employed at the outer air-gap side to retain the rotor’s integrity. For the SPM-MFMM machine, since there is no PM on the rotor, the cup rotor is designed just like a squirrel cage.

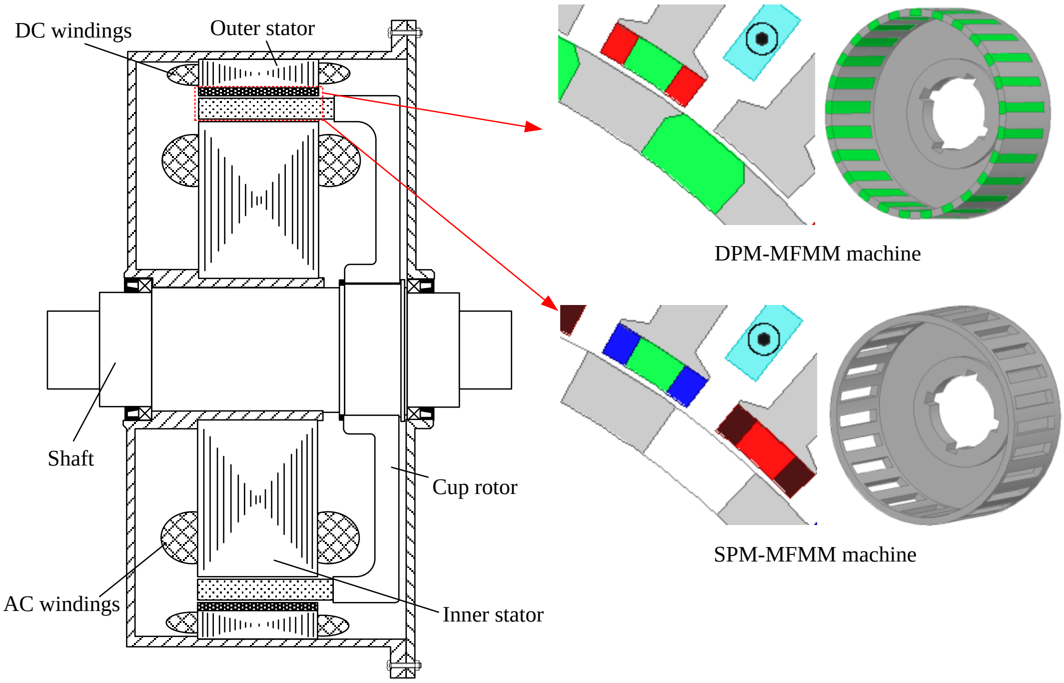

Figure 2.2 Mechanical structures of the proposed machines.

In order to regulate the magnetic flux in the outer stator, concentrated DC field windings are housed in the outer stator slots. The PPN of outer stator PMs should be equal to the PPN of DC field windings. The winding connections of DC field windings and armature windings are shown in Fig. 2.3. Basically the proposed machines have dual-stator and cup-rotor with two air-gaps, the construction of this type of machine has been investigated before in [79].

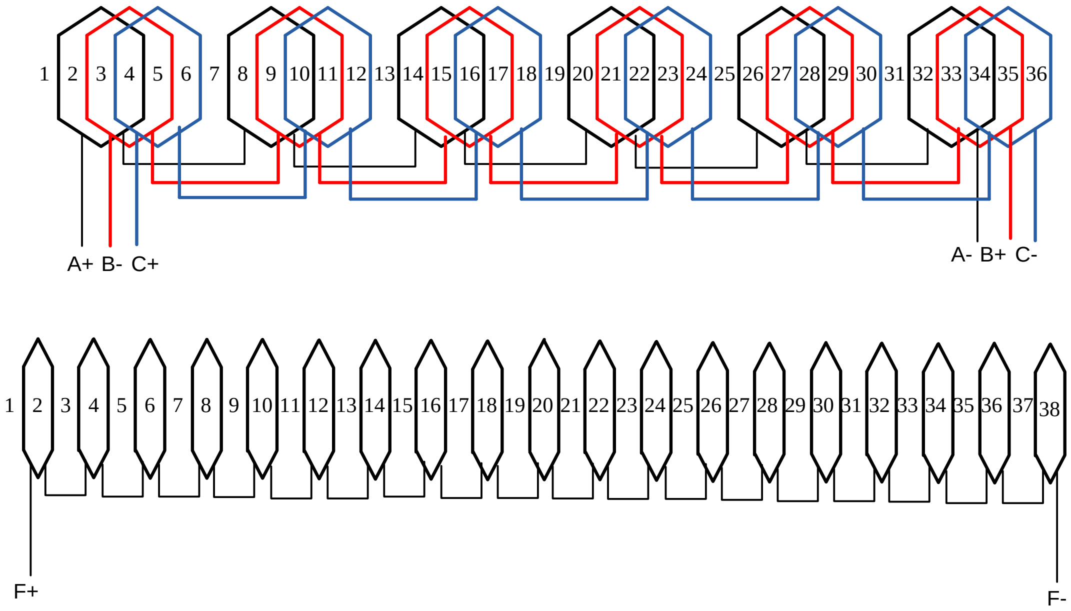

Figure 2.3 Winding connections of the proposed machines.

2.3 DESIGN PRINCIPLE

The working principle of both machines is based on the flux modulating effect. For the DPM-MFMM machine, both the rotor and the outer stator serve as the modulation ring, hence bi-directional field modulating effect can be achieved. For the SPM-MFMM machine, since all the PMs are located on the outer stator, only the rotor has field modulating poles. However, since the SPM-MFMM machine employs all the PMs on the outer stator, it offers better flux controllability than that of the DPM-MFMM machine.

In order to transmit steady torque at different speeds, the interacting magnetic harmonics should have the same pole-pairs and the same rotational speeds. Based on the flux modulating effect, the PPN of the outer stator PMs p_s, the PPN of the rotor p_r and the PPN of the armature windings p_a are governed by

$$p_r = p_s + p_a \tag{2.1}$$

To understand the working principle of these two machines clearly, the magnetic field excited by separate magnetic sources are studied. Firstly, the magnetic field excited only by the outer stator PMs is investigated. The pole-pair number of the magnetic field which is only excited by the outer stator PMs after being modulated by the rotor can be obtained from

$$\begin{aligned} p^{s,r}{}_{m,k} &= \left| mp_s + kp_r \right| \\ m &= 1,3,5,\ldots,\infty \\ k &= 0,\pm 1,\pm 2,\ldots,\pm\infty \end{aligned} \tag{2.2}$$

and the rotational velocities of the corresponding harmonics are

$$\Omega^{s,r}{}_{m,k} = \frac{kp_r}{mp_s + kp_r}\Omega_r \tag{2.3}$$

After the modulation effect of the rotor, a harmonic with the same pole pair number and same rotational speed as those of the armature field will be produced. This harmonic will couple with the armature field to produce a steady torque.

For the DPM-MFMM machine, the magnetic field excited by rotor PMs will also contribute to the torque transmission. The number of pole-pairs in the air-gap excited by the rotor is given by

$$
\begin{aligned}
p^{r,s}{}_{m,k} &= \left| mp_r + kp_s \right| \\
& m = 1,3,5,\ldots,\infty \\
& k = 0,\pm 1,\pm 2,\ldots,\pm\infty
\end{aligned}
\tag{2.4}
$$

The rotational velocities of the corresponding flux density space harmonics are given by

$$
\Omega^{r,s}{}_{m,k} = \frac{mp_r}{mp_r + kp_s}\Omega_r \tag{2.5}
$$

After the modulation effect of the outer stator, a harmonic with the same pole pair number and same rotational speed of those of the armature field will be produced, which will be coupled with the armature field to produce a steady torque. Therefore, the DPM-MFMM machine will have a higher torque density than that of SPM-MFMM machine.

The PMs are embedded in the rotor and they are all magnetized radially outward. The magnetizing winding is fed with DC current pulses to adjust the magnetization level of the stator PMs according to different loading conditions. As the AlNiCo PMs serve as a regulator for the air-gap flux density, the proposed MFMM machines can offer field-regulating effect due to the different magnetization levels of the AlNiCo PMs. The excitation loss is negligible since only DC current pulse is needed. Consequently, the MFMM machines can have higher efficiency than their exiting counterparts.

For DPM-MFMM machine and SPM-MFMM machine, DC magnetizing windings are used to adjust the magnetization level of AlNiCo magnets. Due to the large coercivity of NdFeB PMs, the small pulse current is impossible to change or regulate the magnetic flux of NdFeB PMs. When the AlNiCo magnets are magnetized to have the same magnetization direction with the NdFeB PMs, the magnetic fluxes are enforced. When the AlNiCo magnets are demagnetized and have the opposite magnetization direction with NdFeB PMs, the magnetic flux with the NdFeB PM will produce a flux leakage loop via the AlNiCo PM and not link with the inner stator coils [58].

To achieve flux controllability, the pole-pair number of DC windings p_d should be equal to the PPN of the outer stator PMs p_s .

$$p_d = p_s \tag{2.6}$$

and the number of the outer stator slots N_s is governed by

$$N_s = 2p_d \tag{2.7}$$

In this chapter, for both the DPM-MFMM machine and the SPM-MFMM machine, the rotor PPN is 25, pole-pair number of the outer stator PMs is 19 and the armature windings are single layer integral slot windings with 6 pole-pairs. It can be seen that both machines have almost the same PM material utilization. The periphery of the machines and rotor radii of both machines are the same. For a fair comparison, these two machines are designed to have the same coil structure and the same connections. The final design parameters are listed in Table 2.1.

TABLE 2.1 DESIGN SPECIFICATIONS

Items	DPM-MFMM	SPM-MFMM
Thickness of rotor	3.5mm	6mm
Thickness of outer stator PMs	3.5mm	3.5mm
Length of air-gap	0.6mm	0.6mm
Inner stator outside diameter	163.6mm	158.6mm
Outer stator outside diameter	200mm	200mm
Stack length	65mm	65mm
Number of phases	3	3
PPN of inner stator	6	6
PPN of rotor PMs	25	25
PPN of outer stator PMs	19	19
Number of inner stator slots	36	36
Number of ac conductors	28	28
Number of dc conductors	20	20
Number of outer stator slots	38	38

2.4 MAGNETIZATION TUNING THEORY

The key element for a memory machine is the use of AlNiCo PMs. Its low coercivity makes it an attractive material to achieve online magnetization/demagnetization. Furthermore, since AlNiCo owns nonlinear demagnetization characteristic, the recoil line will never superpose on the demagnetization curve. Therefore, when the demagnetization current is applied and then removed during flux weakening, the operating point of AlNiCo will move back along the recoil line and settle at a lower magnetization level, which means that the magnetization level is memorized. Besides the online magnetizing capability, AlNiCo

PM also owns high thermal stability and high chemical stability, which make it the natural choice for memory machines.

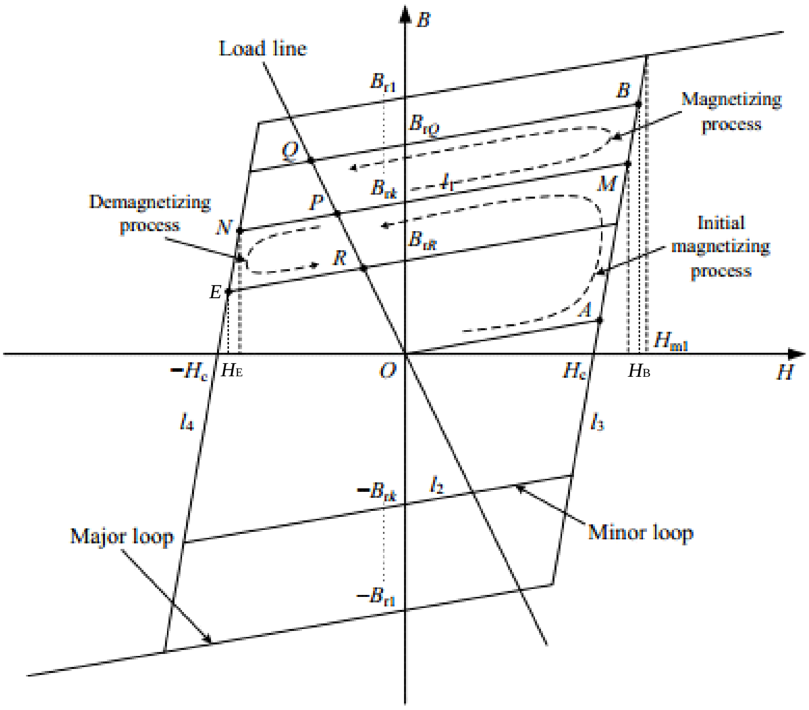

Figure 2.4 Linear hysteresis model of aluminum-nickel-cobalt (AlNiCo) [64].

The hysteresis modeling of AlNiCo magnet is an important issue to control its working point precisely. A linear hysteresis model of AlNiCo PM is proposed in [64] as illustrated in Fig. 2.4. In this model, it is assumed that the major hysteresis loop and all of the minor hysteresis loops own the same value of coercivity, but with different values of remanence. It can be seen that the intersection of the recoil line and the load line will uniquely determine the working points of the AlNiCo PM. During the initial magnetizing stage, the operating point will move along OAMP and settle at Point P with corresponding remanence B_{rk}. If a temporary positive magnetizing force H is applied, the operating point will move along PMBQ and settle at Q with corresponding remanence B_{rQ}. Otherwise, when a temporary negative demagnetizing force H is applied, the operating point will move along PNCR and settle at R with corresponding remanence B_{rR}.

As shown in Fig. 2.4, the equations of Lines l_1 *to* l_4, which represent the magnetizing and demagnetizing processes, can be respectively expressed as:

Line l_1:

$$B = \mu_{\mathrm{r}}\mu_0 H + B_{\mathrm{r}k}, k = 1, 2, 3... \tag{2.8}$$

Line l_2:

$$B = \mu_{\mathrm{r}}\mu_0 H - B_{\mathrm{r}k}, k = 1, 2, 3... \tag{2.9}$$

Line l_3:

$$B = \frac{\mu_{\mathrm{r}}\mu_0 H_{\mathrm{m1}} + B_{\mathrm{r1}}}{H_{\mathrm{m1}} - H_{\mathrm{c}}}\left(H - H_{\mathrm{c}}\right) \tag{2.10}$$

Line l_4:

$$B = \frac{\mu_{\mathrm{r}}\mu_0 H_{\mathrm{m1}} + B_{\mathrm{r1}}}{H_{\mathrm{m1}} - H_{\mathrm{c}}}\left(H + H_{\mathrm{c}}\right) \tag{2.11}$$

where μ_0 refers to the permeability of vacuum, μ_{r} is the relative permeability of the PM material, H_{m1} is the H value of saturation point of the major loop, H_{c} is the coercivity and $B_{\mathrm{r}k}$ (k = 1, 2, 3…) is the remanence of kth hysteresis loop. Obviously, for major loops, $k = 1$, while for minor loops, $k > 1$.

Therefore, starting from the initial operating Point P, if we want to magnetize AlNiCo to the operating Point Q with a remanence B_{rQ}, a positive magnetic intensity of H_B should be applied. By using Equations (2.8) and (2.10), replacing $B_{\mathrm{r}k}$ with B_{rQ}, the magnetizing magnetic intensity H_B can be solved:

$$\begin{cases} B = \mu_{\mathrm{r}}\mu_0 H_B + B_{\mathrm{r}Q} \\ B = \dfrac{\mu_{\mathrm{r}}\mu_0 H_{\mathrm{m1}} + B_{\mathrm{r1}}}{H_{\mathrm{m1}} - H_{\mathrm{c}}}\left(H_B - H_{\mathrm{c}}\right) \end{cases} \tag{2.12}$$

and H_B can be expressed as:

$$H_B = \frac{\left(H_{m1} - H_c\right) B_{rQ} + H_c\left(\mu_r\mu_0 H_{m1} + B_{r1}\right)}{\mu_r\mu_0 H_c + B_{r1}} \tag{2.13}$$

Otherwise, in order to demagnetize AlNiCo to the operating Point R with a remanence B_{rR}, a negative magnetic intensity of H_E should be applied. H_E can be solved in the same way. By using Equations (2.8) and (2.11), replacing B_{rk} with B_{rR}, the magnetizing magnetic intensity H_E can be solved:

$$\begin{cases} B = \mu_r\mu_0 H_B + B_{rR} \\ B = \dfrac{\mu_r\mu_0 H_{m1} + B_{r1}}{H_{m1} - H_c}\left(H_E + H_c\right) \end{cases} \tag{2.14}$$

and H_E can be expressed as:

$$H_E = \frac{\left(H_{m1} - H_c\right) B_{rR} - H_c\left(\mu_r\mu_0 H_{m1} + B_{r1}\right)}{\mu_r\mu_0 H_c + B_{r1}} \tag{2.15}$$

Both the H_B and H_E are excited by the DC current pulse. Since there are two air-gaps in the proposed machine, the relationship between the DC current I_{dc} and H is governed by:

$$H\left(L_{staorPM} + 4\delta\right) = NI_{dc} \tag{2.16}$$

where $L_{staorPM}$ and δ refer to the thickness of outer stator PMs and air-gap length. N is the number of turns of DC windings. Therefore, the amplitude of DC current pulse corresponding to H_B and H_E can be determined. It must be pointed out that this current is just an estimated value, since the magnetic circuit is nonlinear. The DC current needs to be adjusted in real time based on the actual magnetizing/demagnetizing level.

2.5 PERFORMANCE ANALYSIS

Using FEM, the electromagnetic performances of these two machines are investigated and quantitatively compared. The key of flux control is to re/de-magnetize AlNiCo using DC current pulse. Compared with AC vector control in a traditional PM machine, the flux control of the proposed MFMM machine is much simpler, as only the direction and magnitude of the DC current need to be controlled. The simplest way to achieve this purpose includes an H-bridge converter and a controllable voltage source as shown in Fig. 2.5, where the former functions to control the direction of DC currents while the latter serves to control the magnitude of the dc currents. When the power switches S1 and S4 are turned on, a magnetizing current is produced, whereas when the power switches S2 and S3 are turned on, a demagnetizing current is generated.

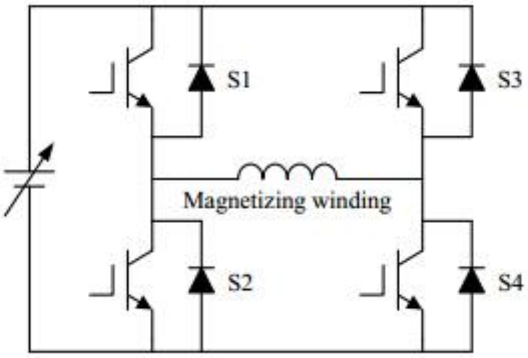

Figure 2.5 H-bridge converter topology for DC current control.

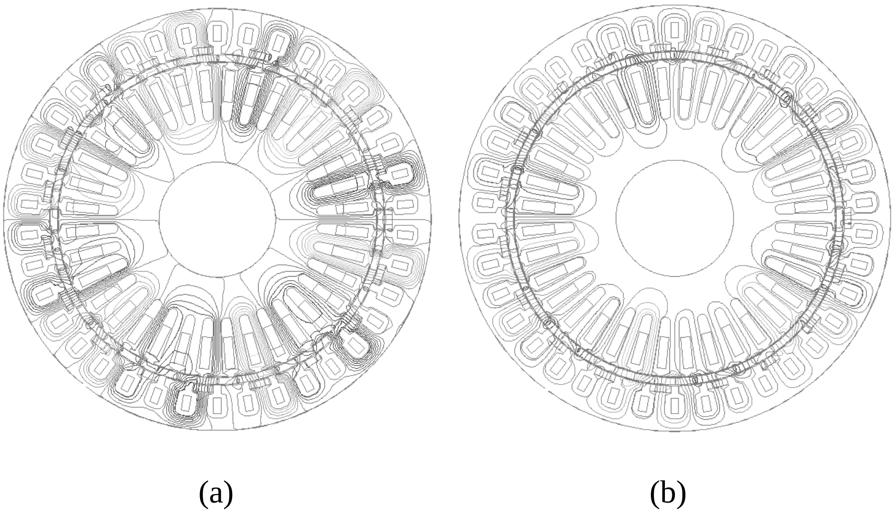

(a) (b)

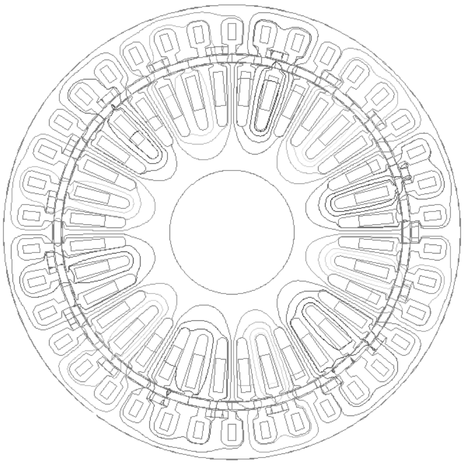

(c)

Figure 2.6 No load magnetic field distributions of the DPM-MFMM machine at different magnetization levels. (a) Full level. (b) Half level. (c) Weak level.

2.5.1 No load flux distributions

According to the magnitudes of magnetizing/demagnetizing current pulses, the magnetization level can be divided into three groups, which are full level using a magnetizing MMF of 2000 A-turn; half level using a demagnetizing MMF of 600 A-turn and weak level using a demagnetizing MMF of 1000 A-turn. The magnetic field distributions of these two machines under different magnetization levels are investigated, as shown in Figs. 2.6 and 2.7, which show the magnetic fields are varying distinctly as the magnetization levels vary.

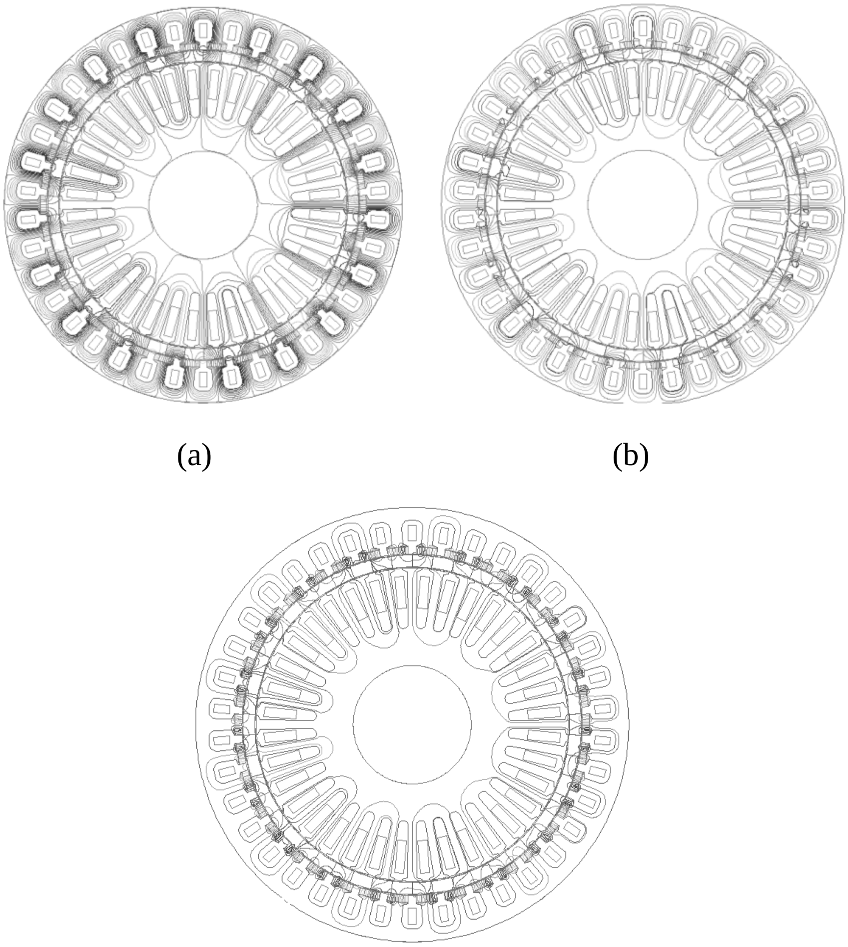

(a) (b)

(c)

Figure 2.7 No load magnetic field distributions of the SPM-MFMM machine at different magnetization levels. (a) Full level. (b) Half level. (c) Weak level.

2.5.2 Air-gap flux density and harmonic spectrum

Figs. 2.8 and 2.9 show the radial flux density and the corresponding harmonic spectrum in the outer air-gap and inner air-gap, respectively, with different magnetization levels of the AlNiCo magnets. It can be seen that there is a clear flux modulating effect of these two machines. Since the PPN of the outer stator PMs is 19, the field harmonic with 19 pole-pairs can be significantly modulated. For the DPM-MFMM machine, besides the fundamental field component with 19 and 25 pole-pairs, the field harmonic with 6 pole-pairs is also significant, which demonstrates a good flux modulating effect of the DPM-MFMM machine. The same phenomena can be observed in the SPM-MFMM machine.

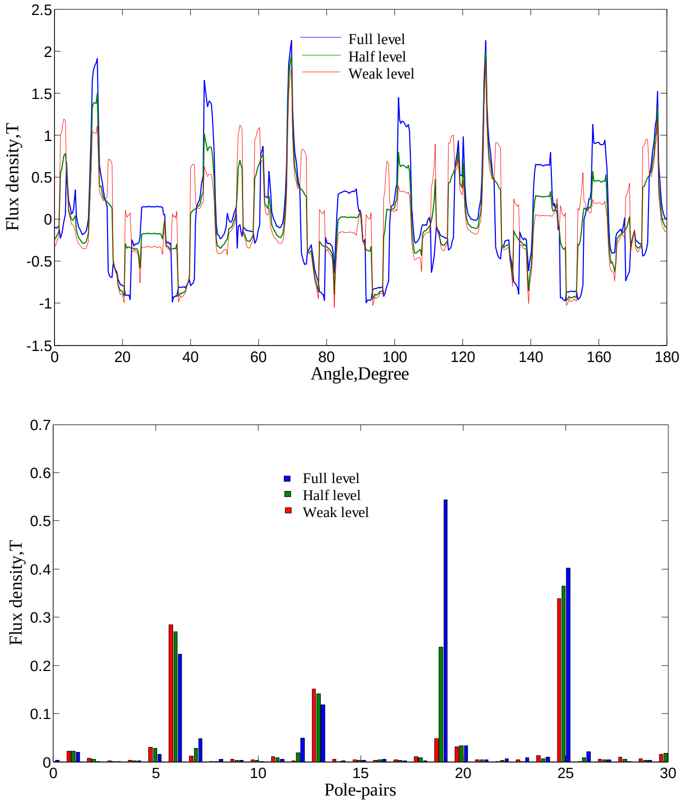

(a)

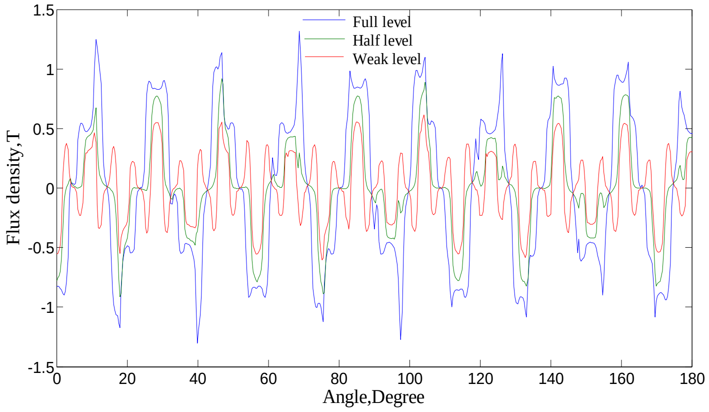

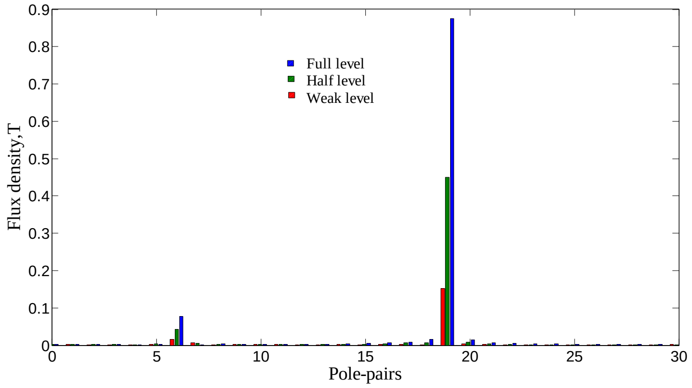

(b)

Figure 2.8 No load air-gap flux density and harmonic spectrum in the outer air-gap.

(a) DPM-MFMM machine. (b) SPM-MFMM machine.

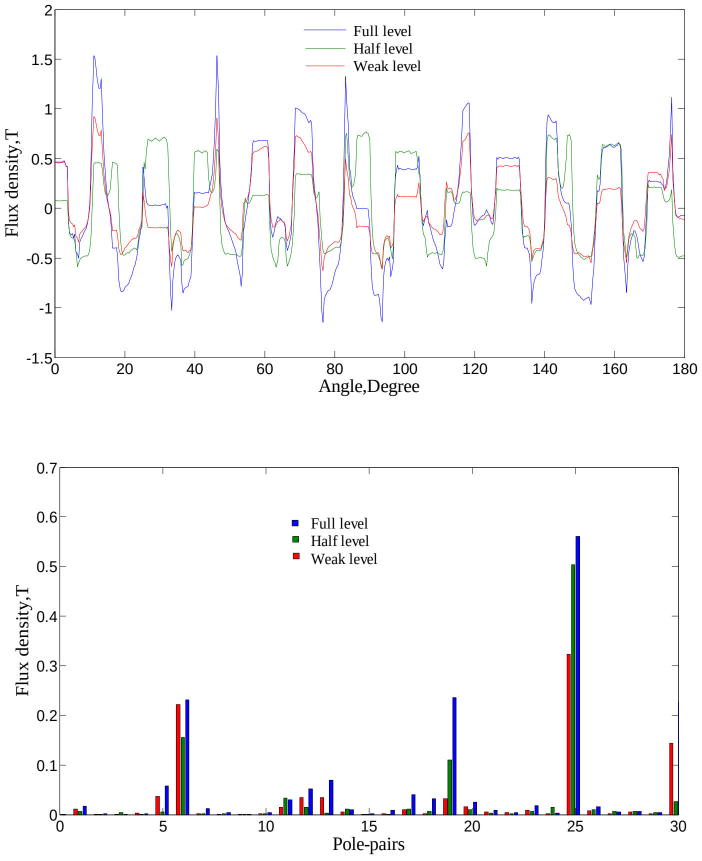

(a)

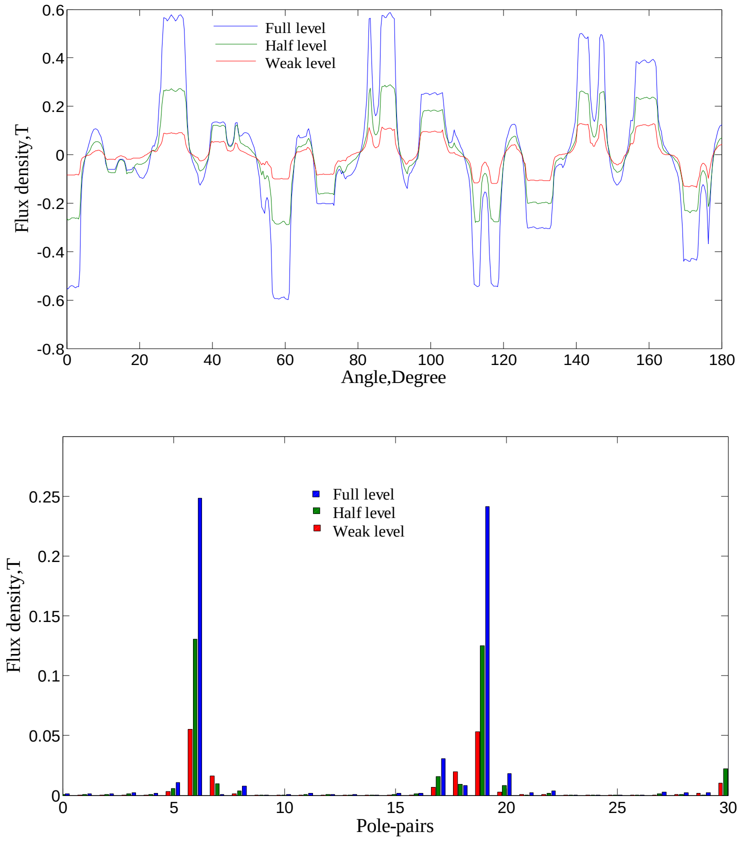

(b)

Figure 2.9 No load air-gap flux density and harmonic spectrum in the inner air-gap.

(a) DPM-MFMM machine. (b) SPM-MFMM machine.

2.5.3 Back EMF

Fig. 2.10 shows the no load back EMF waveforms of these two machines, when the machines run at rated speed 120rpm. It can be observed that both the two machines can generate balanced EMF waveforms. When changing the magnetization state of AlNiCo, the back EMF can be regulated effectively. The flux regulating ratio of SPM-MFMM machine is larger than that of DPM-MFMM machine, which is about 3.72 times. The reason behind this is that SPM-MFMM machine employs all the PMs on the outer stator side, which are easier to be regulated.

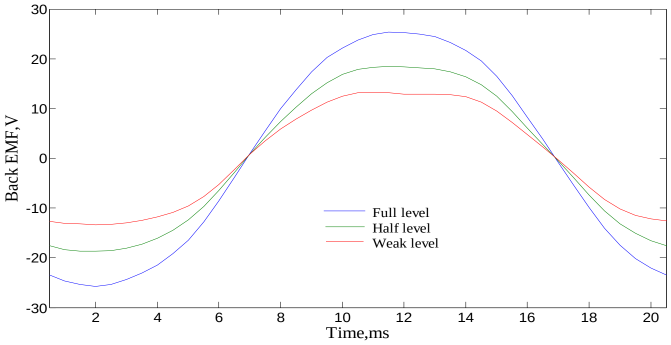

(a)

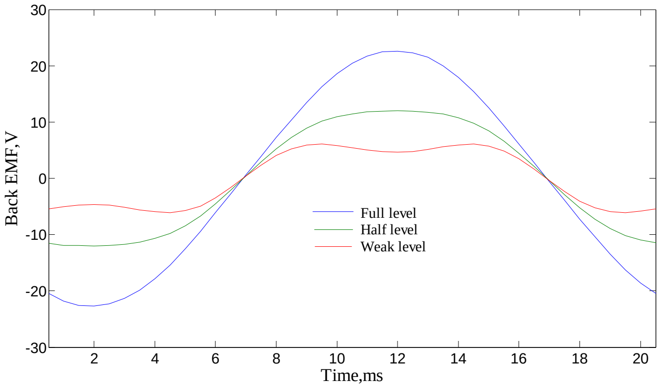

(b)

Figure 2.10 Back EMF waveforms at different magnetization levels. (a) DPM-MFMM machine. (b) SPM-MFMM machine.

2.5.4 Torque characteristics

Fig. 2.11 shows the torque-angle characteristics of these two machines when excited with a sinusoidal and balanced ac current whose RMS value is 50A. The maximum transmitted torque with the same current when the machine runs at its rated speed of 120rpm is shown in Fig. 2.12. The figures indicate that the output torque can be regulated flexibly by applying different magnitudes of current pulses. It can be seen that the DPM-MFMM machine can offer, respectively, 4.6%, 30% and 82.8% higher output torque than those of the SPM-MFMM machine at the three magnetization levels of AlNiCo PMs. In other words, the DPM-MFMM machine produces a higher torque than those from the SPM-MFMM machine.

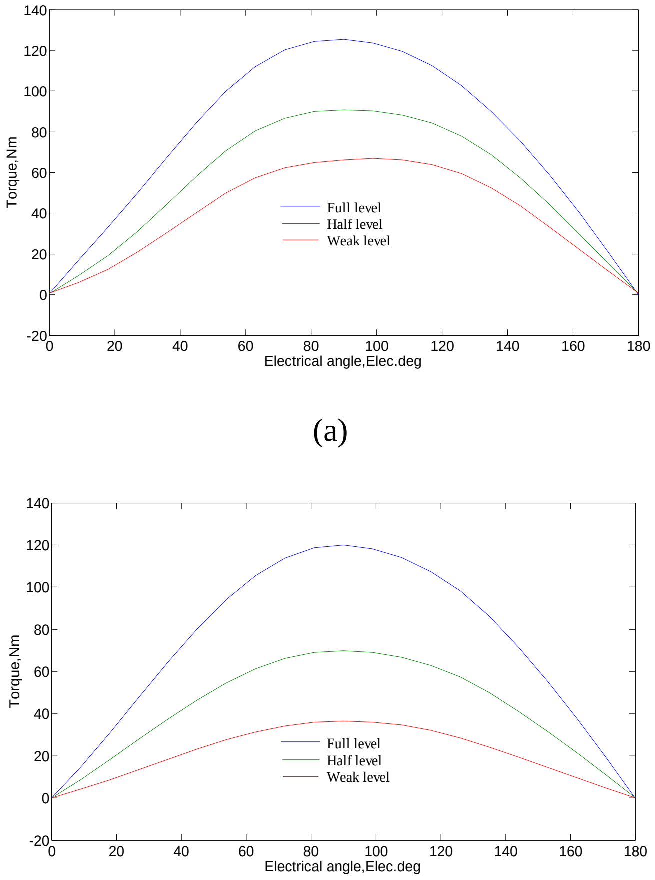

(a)

(b)

Figure 2.11 Torque-angle characteristics at different magnetization levels. (a) DPM-MFMM machine. (b) SPM-MFMM machine.

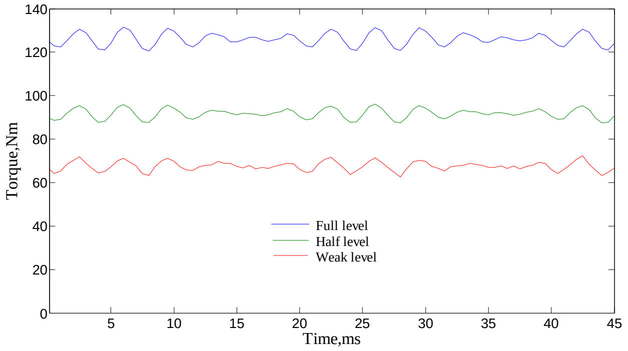

(a)

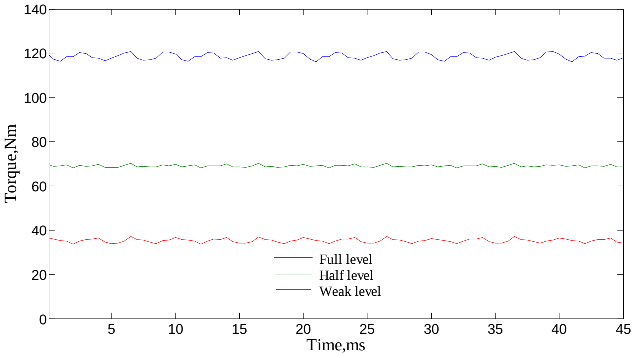

(b)

Figure 2.12 Torque versus time waveforms at different magnetization levels. (a) DPM-MFMM machine. (b) SPM-MFMM machine.

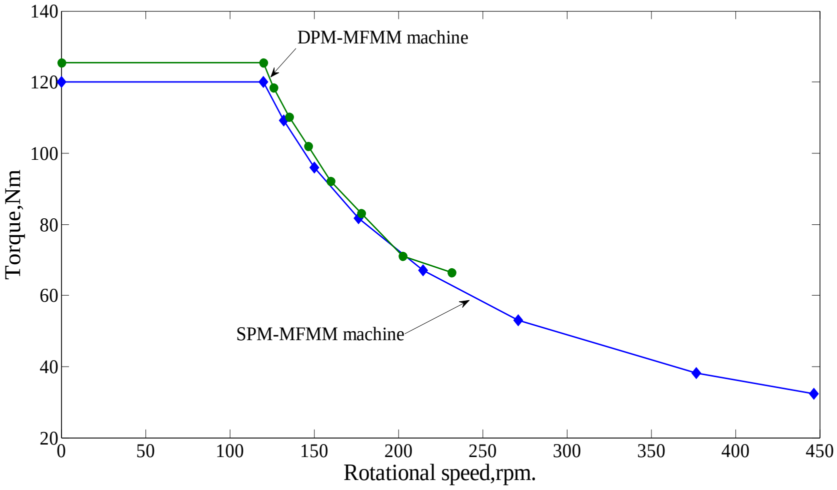

Figure 2.13 Torque versus speed waveforms.

The torque-speed waveforms are given in Fig. 2.13. It can be observed that both machines can realize constant power operation with high efficiency. For the DPM-MFMM machine, since there are NdFeB PMs glued on the rotor, whose magnetic flux cannot be regulated, and the usage of AlNiCo PMs is smaller than the SPM-MFMM machine, hence the flux regulating range of the DPM-MFMM is relatively narrower. Therefore, the maximum constant power rotational speed of the

DPM-MFMM machine is lower than that of the SPM-MFMM machine, which means the SPM-MFMM machine enjoys a better flux controllability. The detailed electromagnetic performances of the proposed MFMMs are given in Table 2.2.

TABLE 2.2 ELECTROMAGNETIC PERFORMANCES

Items	DPM-MFMM	SPM-MFMM
Rated speed	120rpm	120rpm
Rated torque	126Nm	120Nm
Rated power	1575W	1500W
Flux weakening times	2.4	3.72

2.6 SUMMARY

In this chapter, two novel MFMM machines are presented, analyzed and quantitatively compared using FEM. Both of these two machines exploit magnetic-gearing effect to ensure effective coupling between the magnetic fields excited by the armature windings and those excited by the PMs. The air-gap flux density can be regulated efficiently by applying a temporary dc current pulse with negligible excitation loss, hence the machine efficiency can be greatly improved. The comparison results show that the DPM-MFMM machine has higher power density and higher output torque than those of the SPM-MFMM machine. The SPM-MFMM machine however enjoys better flux controllability, which is reflected by its wider range of rated torque and back EMF when the AlNiCo magnets are magnetized from weak level to full level.

CHAPTER 3 FAULT-TOLERANT FLUX-MODULATED MEMORY MACHINE

3.1 INTRODUCTION

In this chapter, a novel fault-tolerant flux-modulated memory (FTFM) machine is proposed, which can not only realize effective flux regulation with reduced power losses, as well as improved fault tolerance ability, but also produces high torque density due to the stator and rotor dual PM design. In the FTFM machine, NdFeB PMs are located in the rotor side to produce torque effectively, and AlNiCo PMs are housed in the outer stator, which enables a flexible and direct flux-tuning capability. The air-gap flux can be regulated effectively by applying a temporary DC current pulse, so the constant power region can be expanded, and the machine efficiency under flux weakening control will be increased because of the negligible DC excitation losses. This machine is designed with five phase armature windings, which can effectively reduce the torque ripple, improve fault tolerance ability and increase the design freedoms of armature windings. The configuration and working principle of this machine is discussed in this chapter. The electromagnetic performance is analyzed using FEM. As one of the most important properties of multiphase PM machines, the fault tolerance capability of the proposed machine is investigated in detail.

3.2 MACHINE CONFIGURATION

Fig. 3.1 shows the configuration of the proposed machine, which is made up of three components, one inner stator, one outer stator and one rotor sandwiched between two stators. Two sets of consequent pole PMs are employed, one on the outer stator using AlNiCo PMs and the other on the rotor using NdFeB PMs. Both rotor PMs and stator PMs are radially magnetized. Each PM and its adjacent iron tooth/ferromagnetic segment will form a pair of magnetic poles. PMs on the outer stator are surface mounted using superglue. Since the rotor is sandwiched between the two stators, the cup rotor structure is artfully used to facilitate the machine assembly. The rotor PMs are glued inside the rotor slots, as there exists great centrifugal force when the rotor is rotating at a high speed, and the wedge structure is employed at the outer air-gap side to keep the rotor's integrity.

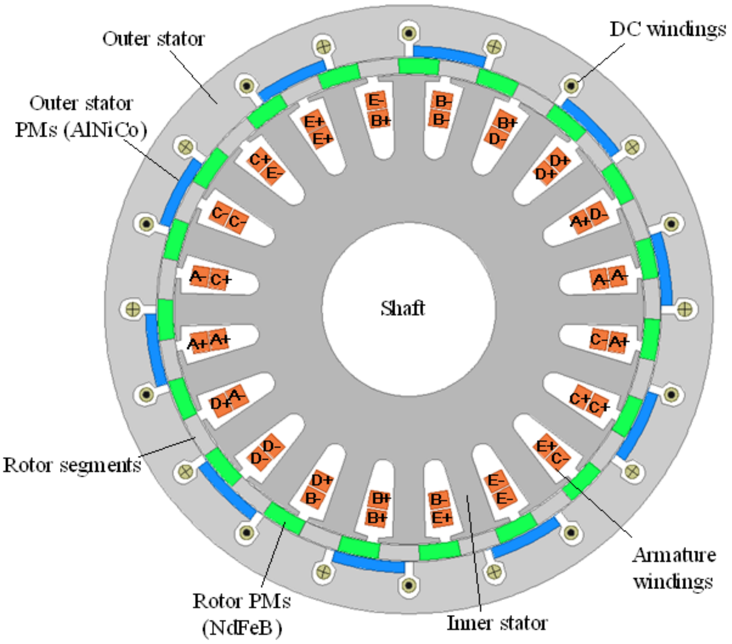

Figure 3.1 Configuration of the proposed FTFM machine.

The design of the FTFM machine is inspired by magnetic gear (MG), but the rotating magnetic field previously provided by inner rotor PMs in MG is now replaced by the five-phase stationary armature windings in the inner stator, while the outer stator magnetic flux in the MG is replaced by the outer stator employed with both DC windings and AlNiCo PMs. The middle modulation ring, which is comprised of ferromagnetic segments and NdFeB PMs, can serve as the rotor in the machine. Similar to the modulation ring in the triple magnet MG in [80], the difference of permeability between the PMs and steel segments allows both the rotor and outer stator to produce field modulation, namely bi-directional field modulation, which is the key to ensure effective magnetic coupling among the magnetic fields excited by the armature windings and the two sets of PMs. The five-phase armature windings are housed in the inner stator slots and DC field windings in outer stator slots.

The working principle and field regulating method of the proposed FTFM machine is the same as the machines discussed in chapter two. The major difference is that FTFM machine proposed in this chapter has five-phase windings and fault-tolerant capability.

Table 3.1 DESIGN PARAMETERS OF FTFM MACHINE

Items	Value
Thickness of rotor PMs	8 mm
Thickness of outer stator PMs	7 mm
Inner stator outside diameter	216 mm
Outer stator outside diameter	280 mm
Stack length	80 mm
Number of phases	5
Number of inner stator pole-pairs	10
Number of rotor pole-pairs	19
Number of outer stator pole-pairs	9
Number of inner stator slots	20
Number of outer stator slots	18
Number of AC conductors	20
Number of DC conductors	20

3.3 ELECTROMAGNETIC PERFORMANCE ANALYSIS

A finite element model of the proposed FTFM machine is established using Maxwell package, with the design parameters shown in Table 3.1. The electromagnetic performances are investigated using FEM.

3.3.1 Mutual coupling

The DC external circuit of the proposed machine is shown in Fig. 3.2, which is used for re-/de-magnetizing the AlNiCo PMs. Since there exists mutual coupling between the AC windings and DC windings, a rectifying circuit is integrated into the DC external circuit to reduce the mutual coupling effect. By setting the AC voltage in the DC external circuit to zero, the current in the DC windings with and without the rectifying components (capacitor C1 and inductance L) is calculated, as shown in Fig. 3.3. The result shows that there indeed exists mutual coupling between the AC windings and DC windings, but the amplitude of this current can be greatly reduced after the use of rectifying components.

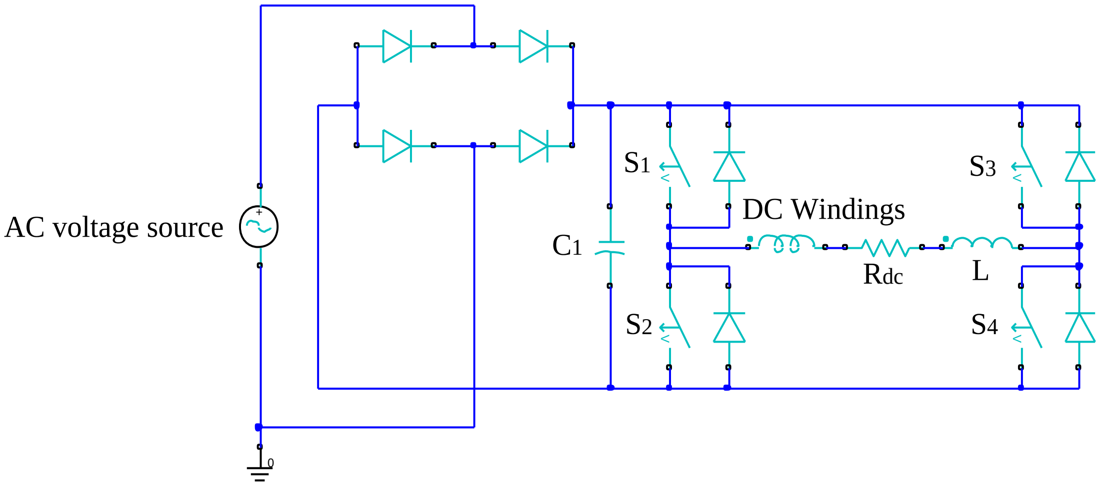

Figure 3.2 External circuit of DC windings.

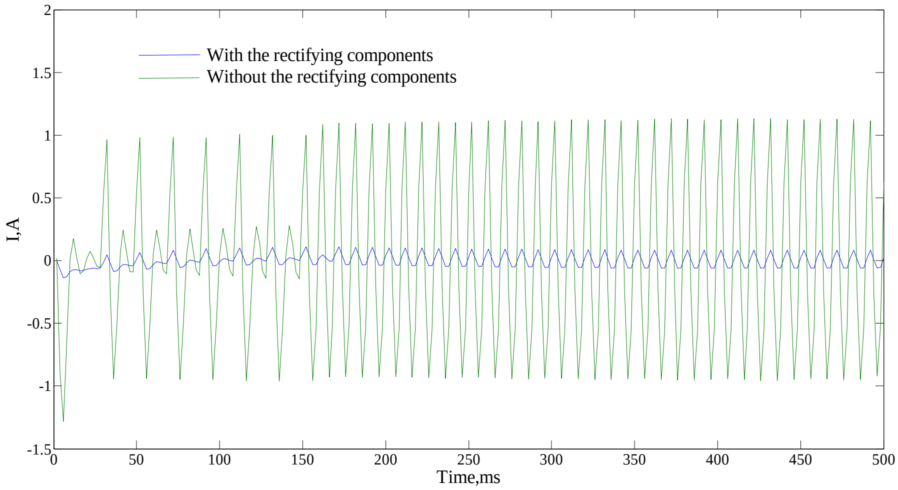

Figure 3.3 Mutual current waveforms of the DC windings.

3.3.2 No load flux distributions

When the power switches S1 and S4 are turned on, a magnetizing current is produced, while when the power switches S2 and S3 are turned on, a demagnetizing current is generated. According to the magnitudes of magnetizing/demagnetizing current pulses, the magnetization level can be divided into three groups, which is a full level using a magnetizing MMF of 2000 A-turns, then a half level using a demagnetizing MMF of 600 A-turns and a weak level using a demagnetizing MMF of 1000 A-turns. Firstly, the magnetic field distributions of the proposed FTFM machine under different magnetization levels are investigated, as shown in Fig. 3.4. One can see clearly that the magnetic flux line distribution is densest when a magnetizing current (Fdc = +2000 A-turns) is applied, and it becomes sparsest when a demagnetizing current (Fdc = −1000 A-turns) is applied. This phenomenon is especially significant in the outer stator and reflects a good field regulating effect.

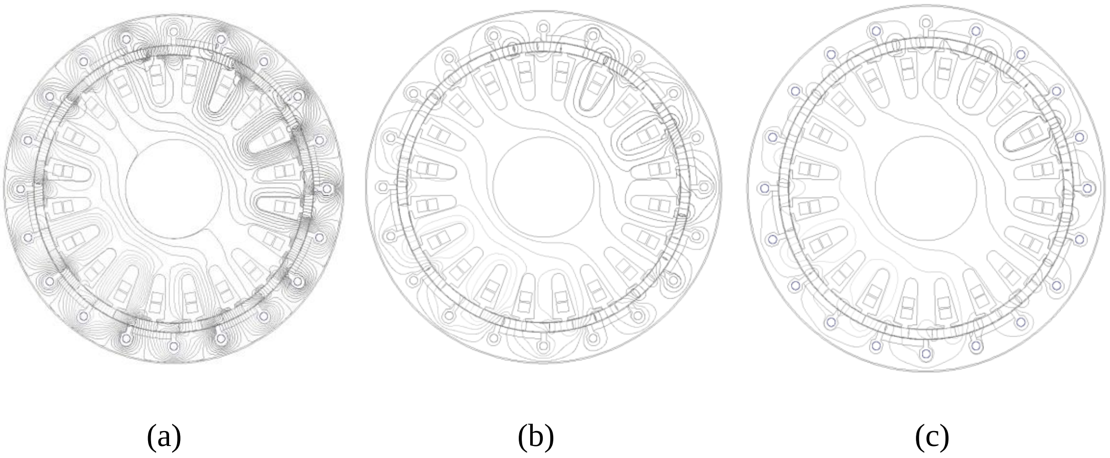

Figure 3.4 No-load magnetic field distributions of the FTFM machine at different magnetization levels. (a) Full level. (b) Half level. (c) Weak level.

3.3.3 Air-gap flux density

The corresponding air-gap flux density distributions in the air-gap are shown in Fig. 3.5, illustrating that an air-gap flux regulation range of 2.5-times can be realized. Since all of the PMs are magnetized in the same direction, the flux density waveforms are not symmetrical.

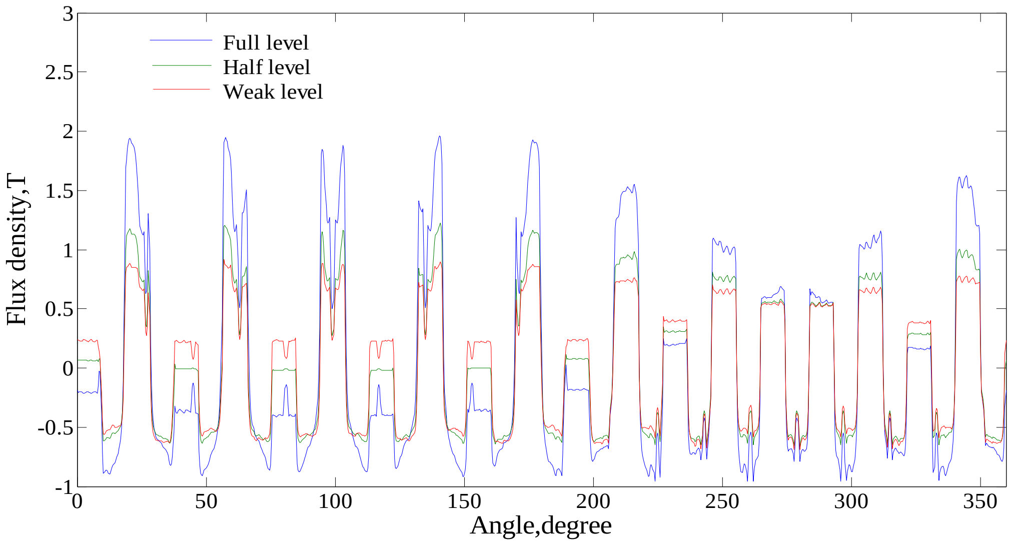

(a)

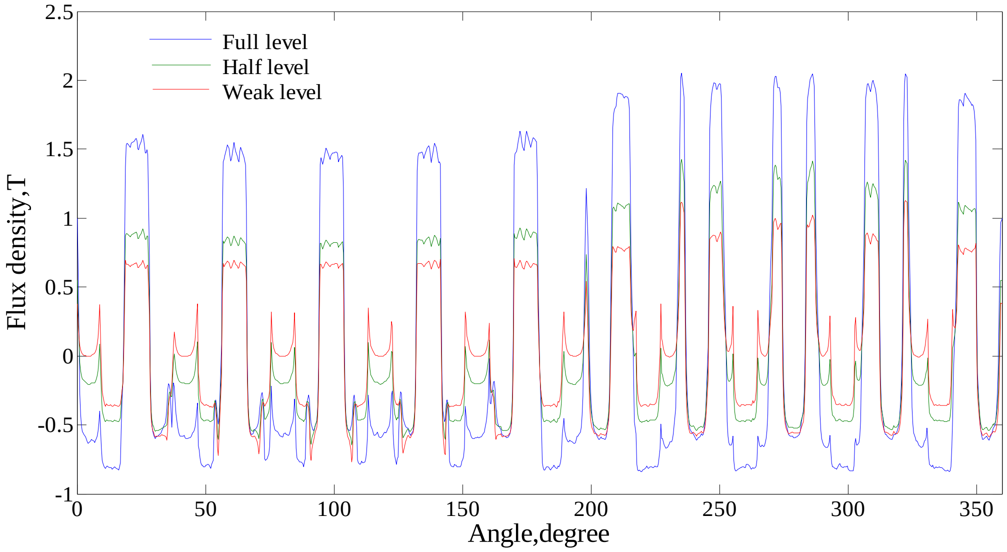

(b)

Figure 3.5 Air-gap flux density distributions under different magnetizing level. (a) Inner air-gap. (b) Outer air-gap.

3.3.4 Back EMF

The back EMF of the proposed FTFM machine without flux control is shown in Fig. 3.6(a), in which the machine speed is 287 rpm. It can be seen that balanced five-phase EMF waveforms can be reduced in the armature windings. The A-phase back EMF with flux control is shown in Fig. 3.6(b), which illustrates that the back EMF can be regulated effectively. Transient analysis of back EMF from rated operation to flux weakening operation is also studied, the transient back EMF of Phase A is depicted and shown in Fig. 3.6(c), which also shows a good flux regulating effect, and good dynamic responses.

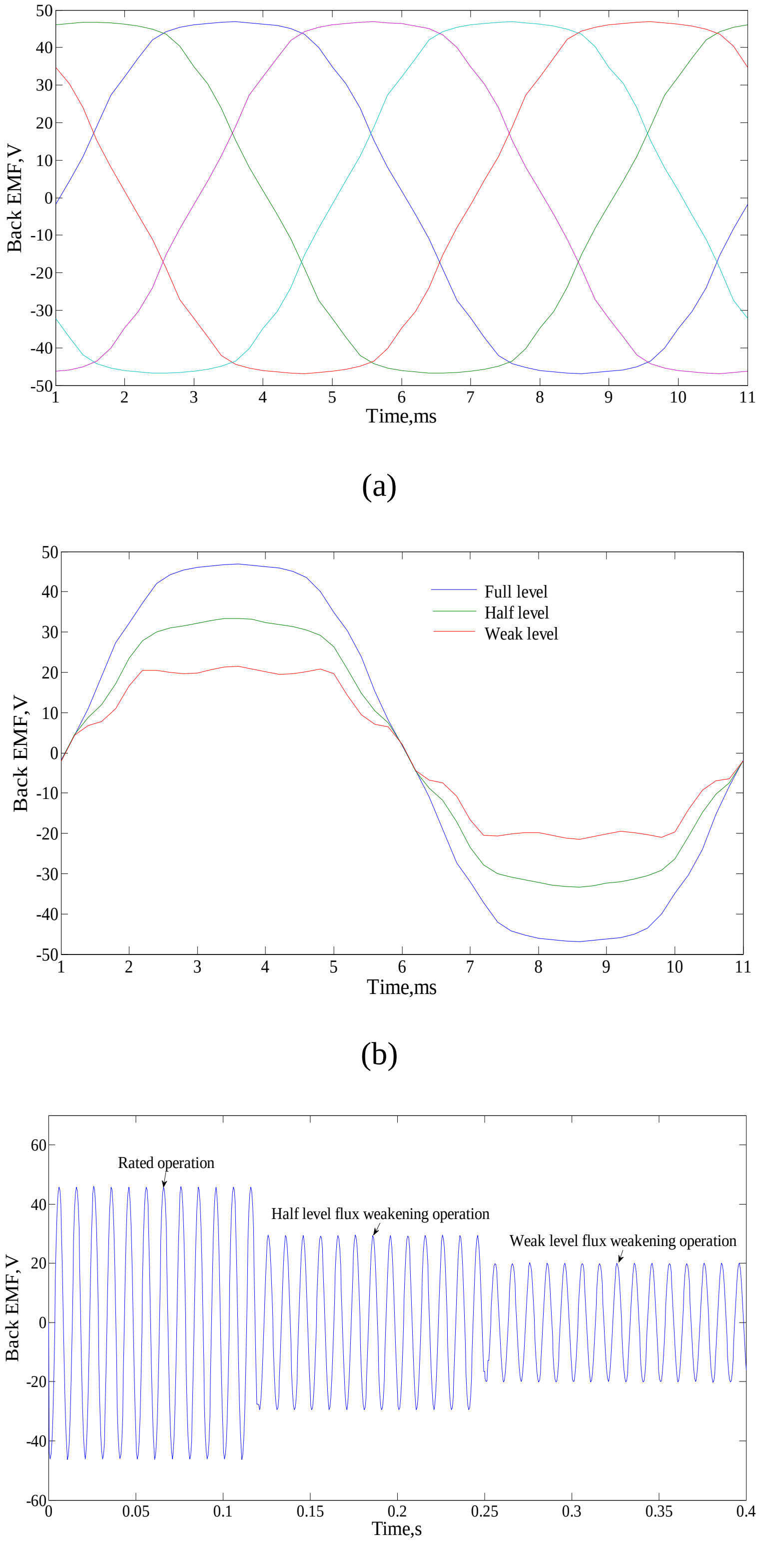

(a)

(b)

(c)

Figure 3.6 Back EMF of the proposed machine. (a) Five-phase back EMF. (b) Back EMF of Phase A with flux control. (c) Transient back EMF of Phase A.

3.3.5 Demagnetization analysis

One of the concerns for memory machines with AlNiCo excitation is the demagnetization issue. Feasible designs should make AlNiCo PMs immune from the demagnetization risk of armature currents, and the magnetization state of AlNiCo PMs only affected by DC current pulse. Fig. 3.7 shows the flux line distribution generated by the full load AC current and rotor PMs, in which the AlNiCo PMs are replaced with air during simulation. It can be seen that only very few flux lines pass through the area of AlNiCo PMs, and most of the flux lines pass through the outer stator teeth instead since the reluctance of AlNiCo PMs is much larger than the stator teeth. Therefore, the AlNiCo PMs will not be demagnetized by the armature reaction field during the machine operation.

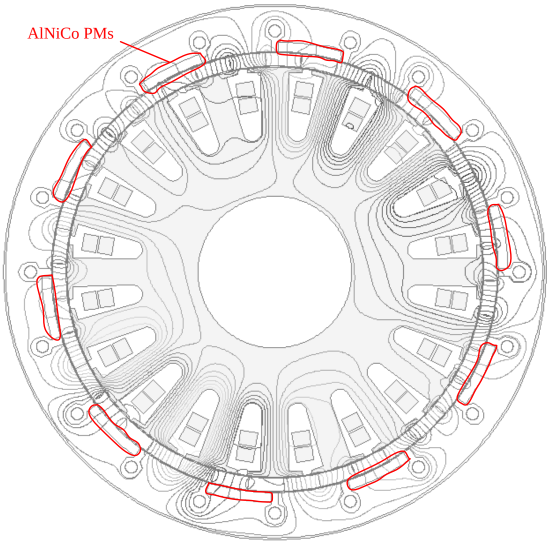

Figure 3.7 Flux line distribution.

3.3.6 Torque characteristics

Fig. 3.8(a) shows the torque-angle characteristics of the proposed machine with and without flux control when excited with a 40-A sinusoidal and balanced AC current. One can see a clear regulation effect on the torque. The maximum torque reaches 157 Nm when applied with a magnetizing current of +2000 A-turns. The maximum transmitted torque with the same current when the machine runs at the rated speed of 500 rpm are shown in Fig. 3.8(b), and the torque ripple is 6.64 Nm, 4.66 Nm and 5.1 Nm, corresponding to the three magnetizing level, respectively, which is very small compared to the maximum transmitted torque.

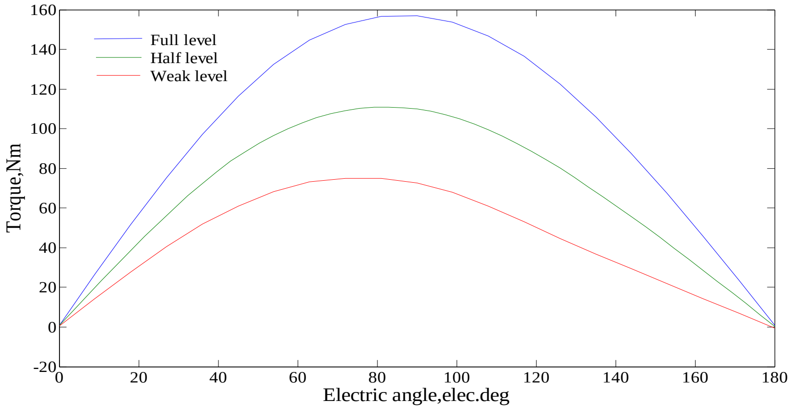

(a)

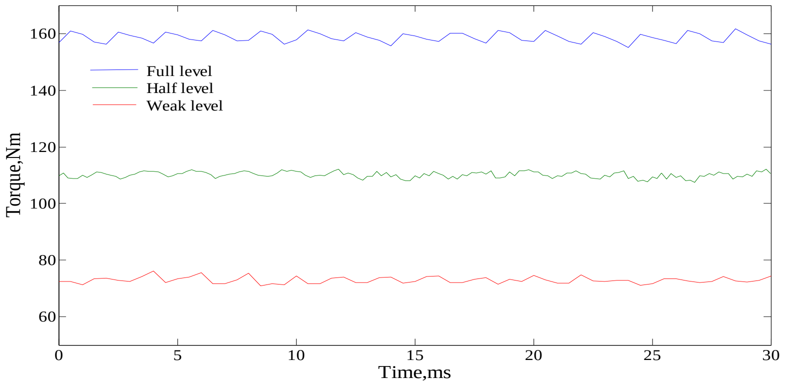

(b)

Figure 3.8 Torque characteristic of the proposed machine. (a) Torque-angle waveforms. (b) Torque-time waveforms.

3.4 FAULT TOLERANT ANALYSIS

Fault-tolerant capability is one of the most important features of multiphase machines, which means that they can continue to operate in a satisfactory manner even under fault conditions. As the machine output torque is proportional to its interacting field, so the same torque can be maintained as long as the rotating MMF produced by the variations of all five-phase currents keeps unchanged in both time and space.

3.4.1 One phase open-circuit

When one-phase open-circuit (for example, Phase A is open-circuit), to maintain a proper operating condition, the magnetic field produced by the remaining four healthy phases should remain unchanged. The MMF is produced by the remaining four phases:

$$\mathrm{MMF}_t'(\theta,t)=\mathrm{MMF}_\mathrm{b}'(\theta,t)+\mathrm{MMF}_\mathrm{c}'(\theta,t)+\mathrm{MMF}_\mathrm{d}'(\theta,t)+\mathrm{MMF}_\mathrm{e}'(\theta,t) \tag{3.1}$$

For the sake of getting a unique solution and to guarantee that the summation of four current phases is zero, the phase currents are governed by:

$$i'_\mathrm{b}=-i'_\mathrm{d},\qquad i'_\mathrm{c}=-i'_\mathrm{e} \tag{3.2}$$

and the new phase currents can be expressed as:

$$\begin{cases} i'_\mathrm{a}=0 \\ i'_\mathrm{b}=1.382I_\mathrm{m}\cos\left(\omega t+\dfrac{\pi}{5}\right) \\ i'_\mathrm{c}=1.382I_\mathrm{m}\cos\left(\omega t+\dfrac{4\pi}{5}\right) \\ i'_\mathrm{d}=1.382I_\mathrm{m}\cos\left(\omega t-\dfrac{4\pi}{5}\right) \\ i'_\mathrm{e}=1.382I_\mathrm{m}\cos\left(\omega t-\dfrac{\pi}{5}\right) \end{cases} \tag{3.3}$$

It can be seen that the remediation is to regulate the Phase B current retarded by 36° and the Phase E current advanced by 36°, while keeping the angles of Phase C and Phase D currents unchanged. Furthermore, the current amplitudes of all the remaining phases are increased to 1.382 times their pre-fault values. Fig. 3.9 shows the output torque and armature current waveforms at full load when under one-phase open-circuit condition, where we can see that this machine can still output steady torque when one-phase open-circuit, but the torque ripple is relatively higher.

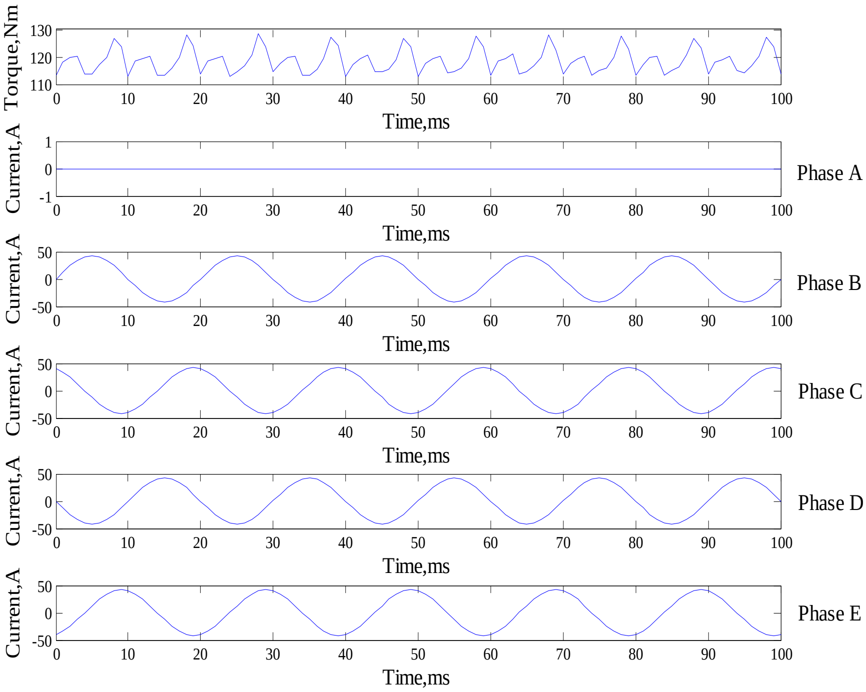

Figure 3.9 Output torque and armature current waveforms under one-phase open-circuit condition.

3.4.2 Two phase open-circuit

When two adjacent phases open-circuit (for example, both Phase A and Phase B are open-circuit), the MMF will be generated by the remaining three healthy phases:

$$MMF_t''(\theta,t) = MMF_c''(\theta,t) + MMF_d''(\theta,t) + MMF_e''(\theta,t) \tag{3.4}$$

and the current of the remaining three phases are purposely governed by:

$$i''_c + i''_d + i''_e = 0 \tag{3.5}$$

Therefore, the current of the remaining three phases can be expressed as:

$$\begin{cases} i''_{\mathrm{c}} = 2.236 I_{\mathrm{m}} \cos\left(\omega t + \dfrac{2\pi}{5}\right) \\ i''_{\mathrm{d}} = 3.618 I_{\mathrm{m}} \cos\left(\omega t - \dfrac{4\pi}{5}\right) \\ i''_{\mathrm{e}} = 2.236 I_{\mathrm{m}} \cos(\omega t) \end{cases} \tag{3.6}$$

It can be seen that the angles of Phase C and Phase E currents are regulated to that of the pre-fault Phase B and Phase A currents, respectively, while the angle of Phase D current is unchanged. The current amplitudes of Phase C and Phase E are 2.236 times and Phase D is 3.618 times their pre-fault values. The output torque and armature current waveforms when the machine works at full load are shown in Fig. 3.10. Again, we can find that this machine can work well under two-phase open-circuit operation. For the case of two nonadjacent phases open-circuit, the corresponding analysis is similar to that of two adjacent phases that are open-circuit.

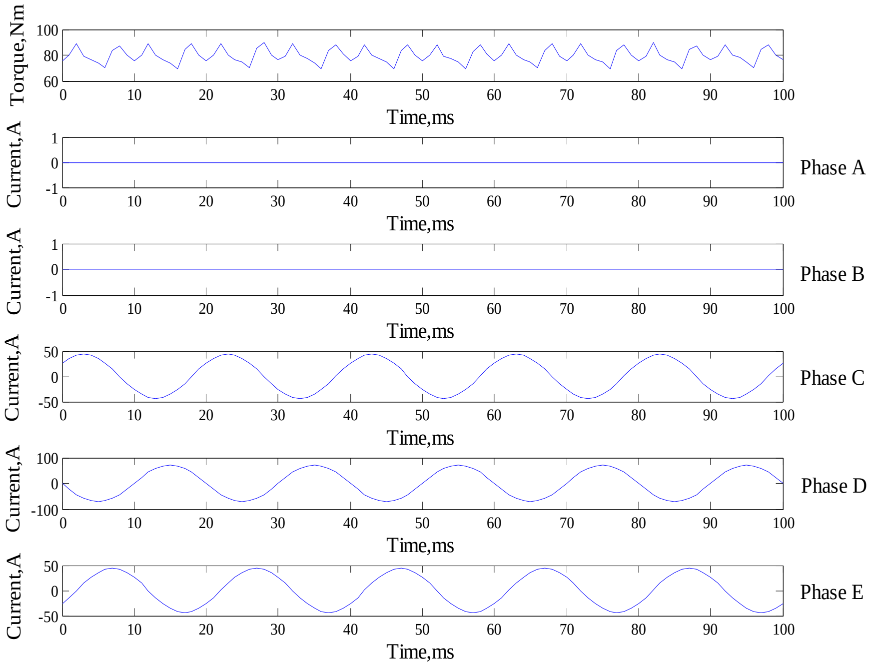

Figure 3.10 Output torque and armature current waveforms under two-phase open-circuit condition.

3.4.3 Torque comparison and field harmonics

The torque characteristic of the proposed machine under fault-tolerant operation are investigated and compared with torque when working at normal conditions, as shown in Fig. 3.11, which show that the torque density decreases during fault-tolerant operation; the maximum torque is 157 Nm, 119 Nm and 81 Nm for normal condition, one-phase open circuit condition and two-phase open circuit condition, respectively. However, the torque ripple increases during fault-tolerant operation; the torque ripple is 4.9 Nm 15.8 Nm and 19.5 Nm for these three conditions, respectively.

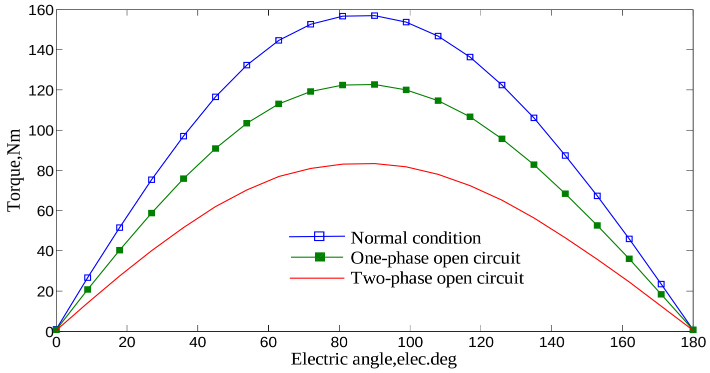

(a)

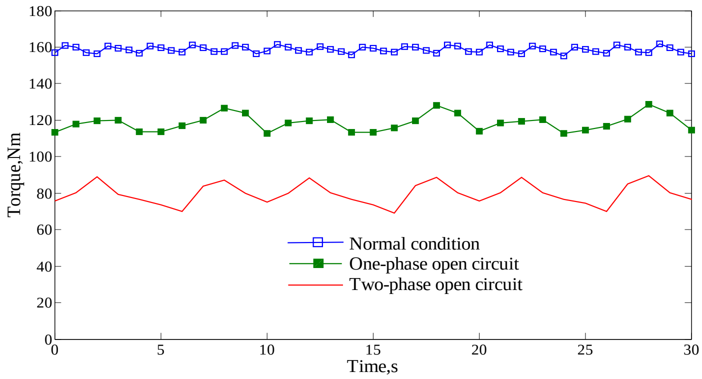

(b)

Figure 3.11 Torque characteristic of the FTFM machine at normal condition and fault conditions. (a) Torque-angle waveforms. (b) Maximum torque-time waveforms.

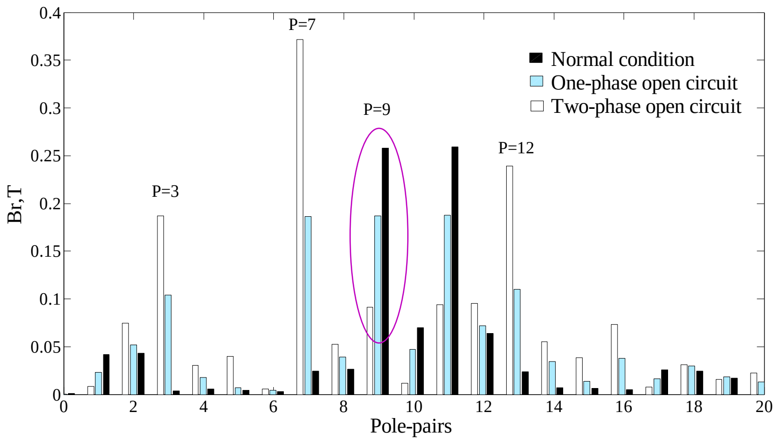

(a)

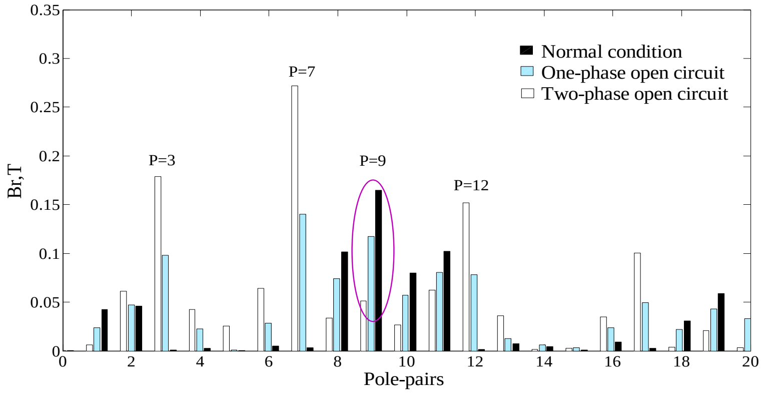

(b)

Figure 3.12 Field harmonics excited only by armature windings when working at normal condition and fault conditions. (a) Inner air-gap. (b) Outer air-gap.

In this proposed machine, the armature windings are designed with 9 pole-pairs, which will contribute to the average torque; other harmonics will cause the torque ripple. The field harmonics excited only by the armature windings in both normal condition and open circuit conditions are investigated, as shown in Fig. 3.12. One can see clearly that the dominant harmonic component in generating average torque with 9 pole-pairs is weakened during fault-tolerant operation, which leads to the reduction of the torque density; while other harmonics with 3, 7 and 12 pole-pairs, which will not contribute to the average torque, but only causes torque ripple, are strengthened during fault-tolerant operation, which is responsible for the increase of the ripple torque when one or two phases open circuit.

3.5 SUMMARY

In this chapter, a novel fault-tolerant flux-modulated memory PM machine is proposed. By using consequent-pole PMs on both the rotor and the outer stator, this machine can realize bi-directional field modulation, which is the foundation to ensure the effective magnetic coupling and flux regulation in the air-gap. Hence, the proposed machine can enjoy a large torque density, and a torque density of 32kNm/m^3 can be achieved. The magnetic flux consists of magnetic fields excited by the two sets of PMs and those excited by the armature windings. The air-gap flux density can be regulated readily by applying a temporary DC current pulse with negligible excitation loss; hence, the machine operating region can be expanded, and the machine efficiency can also be improved. The fault-tolerant capabilities of the proposed machine are studied in detail. The results show that this machine can maintain good operation state under open-circuit situations. The detailed electromagnetic performances of the proposed machine are shown in Table 3.2.

Table 3.2 ELECTROMAGNETIC PERFORMANCES

Items	FTFM
Power	7.8 kW
Rated speed	500 rpm
Efficiency	>90%
Maximum torque	157 Nm
Maximum torque when one-phase open-circuited	119 Nm
Maximum torque when two-phase open-circuited	81 Nm

CHAPTER 4 HYBRID-EXCITED DUAL PM MACHINE

4.1 INTRODUCTION

HEMs with both PM and field coil excitations have been investigated to improve the flux weakening performance, the efficiency of the HEMs can be optimized as reported in [81]. Currently, the existing HEMs employ only one set of PMs, which are either located on the rotor or the stator. The torque capability of these machines is limited, as the PM usage is restricted to the available space in rotor or stator. The memory machines proposed in chapters two and three have dual PM excitation, but their structure is relatively complicated due to their double air-gaps.

In this chapter, a novel hybrid-excited dual PM machine (HEDPM) is proposed, which is developed from the machines in chapters two and three. The machine structure is simplified with single air-gap. The configuration of the proposed machine is firstly discussed. Then the working principle is investigated through analytically studying the air-gap field harmonics after flux modulation. The electromagnetic performances of the proposed machine are studied using time-stepping FEM (TS-FEM). A prototype is made and experimental tests are conducted to verify the proposed design.

4.2 MACHINE CONFIGURATION

Fig. 4.1(a) shows the configuration of the proposed machine. It consists of one rotor and one stator. PM excitations are employed on both the rotor and the stator. All the PMs are radially outward magnetized. Each PM and its adjacent iron tooth form a pair of magnetic poles. Two sets of windings are employed and both housed in the stator slots. One is the armature winding, which is used to produce the rotating magnetic field. The other is the DC field winding, which is used for field regulation.

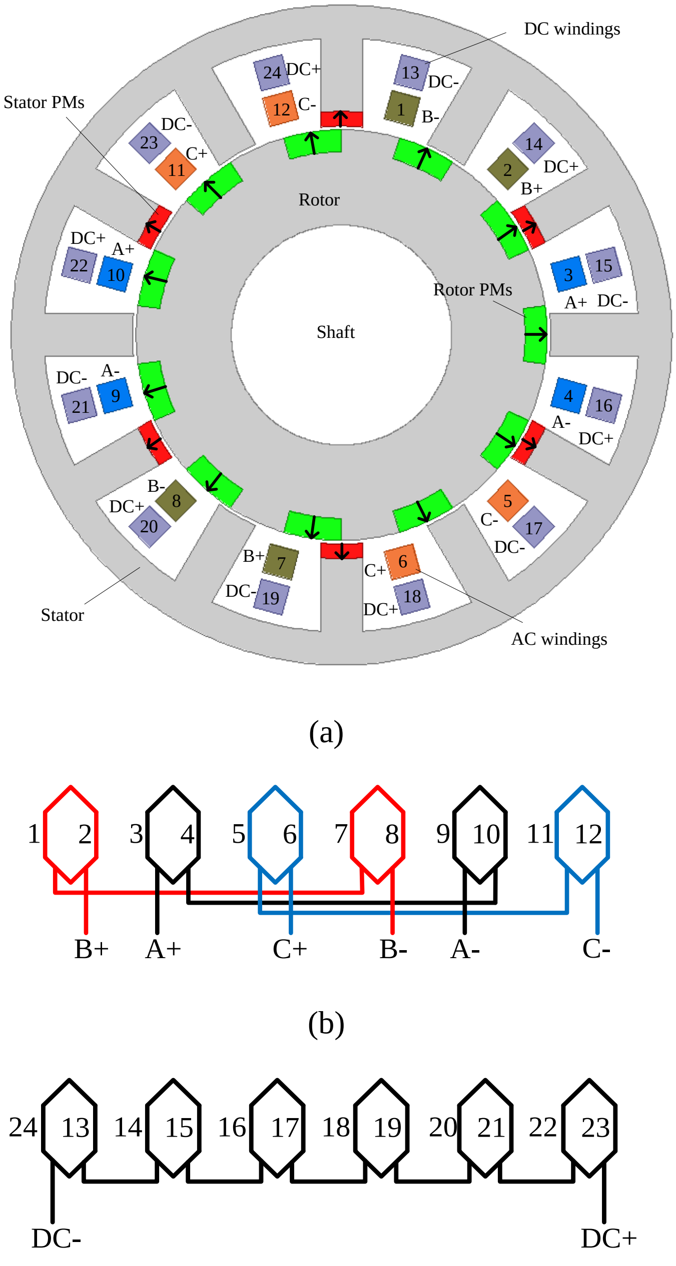

(a)

(b)

(c)

Figure 4.1 Configuration and winding connection of the proposed machine. (a) Configuration. (b) Armature winding connection. (c) DC field winding connection.

The winding connections of AC and DC windings are given in Fig. 4.1 (b) and (c). The proposed HEDPM machine offers many advantageous features:

- *Dual-PM excitation.* Both the rotor and the stator own PM excitations. The permeance difference between PMs and iron tooth enables both the rotor and the stator good flux modulating effect, which is referred as dual-magnetic gearing effect in [82]. Numbers of synchronous harmonics with the same pole-pairs and rotating velocities are generated and contribute to the effective electromagnetic torque production.
- *Concentrated armature windings and field windings as shown in Fig. 4.1 (b) and (c).* This design can shorten the end-winding and reduce the copper loss, thus improve the utilization of both copper and iron materials.
- *Good flux regulating capability.* By controlling the direction and magnitude of DC field current, the air-gap flux can be regulated effectively. Therefore, the constant power operating region can be expanded.

4.3 WORKING PRINCIPLE

Since both the stator and the rotor have flux modulating effect, bidirectional flux modulating can be achieved in the proposed machine, which guarantees effective coupling among different magnetic sources. In order to reveal the working principle of the proposed HEDPM, the field harmonics excited by different magnetic sources are investigated in detail..

4.3.1 Flux density of stator PMs

The air-gap magnetomotive force (MMF) generated by the stator PMs accounting for the stator saliency is assumed to be square wave with air-gap circumferential position θ [83], as shown in Fig. 4.2. The Fourier series expansion $F_{PMs}(\theta)$ is given by

$$F_{PMs}(\theta) = \sum_{n=1,3,5...}^{\infty} \frac{4F_{PMs}}{n\pi} \sin np_s \frac{\theta_s}{2} \cos np_s\theta \tag{4.1}$$

where θ_s refers to the arc of stator teeth, which is also equal to the arc of the stator PMs, p_s and F_{PMs} refer to the pole-pair number of stator PMs and the value of stator PM MMF, respectively.

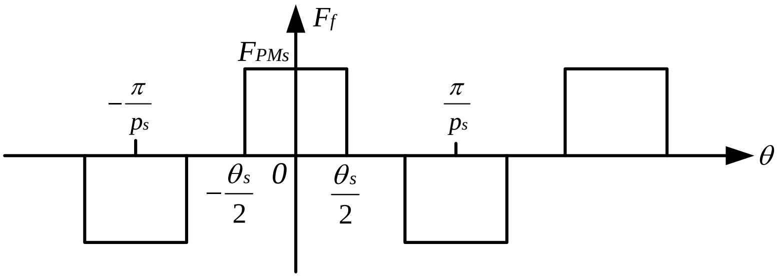

Figure 4.2 Air-gap MMF produced by stator PMs.

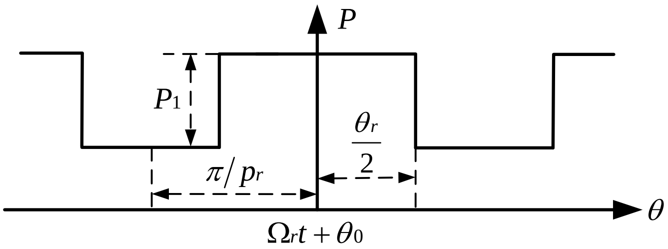

Figure 4.3 Air-gap permeance model of rotor.

The air-gap permeance model of rotor accounting for rotor saliency is presented in Fig. 4.3, and the permeance function of rotor can be expressed by its Fourier series.

$$P_r(\theta,t) = P_0 + \sum_{k=1}^{\infty} \frac{2P_1}{k\pi} \sin kp_r \frac{\theta_r}{2} \cos kp_r(\theta - \Omega_r t - \theta_0) \tag{4.2}$$

where P_0 and P_1 are the dc component and peak-peak value of permeance waveform in Fig. 4.3. θ_r, Ω_r, θ_0 and p_r are the rotor pole arc, the rotor speed in radian per second, the initial rotor teeth position and the rotor pole-pair number. As reported in [84], the flux density excited by the stator PMs $B_{PMs}(\theta,t)$ can be obtained by multiplying $F_{PMs}(\theta)$ and $P_r(\theta,t)$.

$$\begin{cases} B_{PMs}(\theta,t) \\ = F_{PMs}(\theta)P_r(\theta,t) \\ = \dfrac{4F_{PMs}P_0}{\pi}\displaystyle\sum_{n=1,3,5...}^{\infty} A_n\cos np_s\theta + \dfrac{4F_{PMs}P_1}{\pi^2}\displaystyle\sum_{n=1,3,5...}^{\infty}\sum_{k=1}^{\infty} A_nB_k(\cos\alpha_1+\cos\alpha_2) \\ \alpha_1 = (np_s+kp_r)\left[\theta - \dfrac{kp_r(\Omega_r t+\theta_0)}{np_s+kp_r}\right] \\ \alpha_2 = (np_s-kp_r)\left[\theta + \dfrac{kp_r(\Omega_r t+\theta_0)}{np_s-kp_r}\right] \\ A_n = \dfrac{1}{n}\sin\left(np_s\dfrac{\theta_s}{2}\right), B_k = \dfrac{1}{k}\sin\left(kp_r\dfrac{\theta_r}{2}\right) \end{cases} \tag{4.3}$$

From Eq.(4.3), we can see that the flux density excited by the stator PMs can be divided into three groups. The static harmonics with np_s pole-pairs are the original harmonics of stator PMs. The rotating harmonics with np_s+kp_r and np_s-kp_r pole-pairs, rotate at angular speed of $kp_r\Omega_r/(np_s+kp_r)$ and $-kp_r\Omega_r/(np_s-kp_r)$, respectively. The negative notation means these harmonics rotate opposite to the rotor direction. Both the two rotating harmonic groups are generated by the modulating effect of the rotor. The harmonic pole-pair number and angular velocity of air-gap field excited by the stator PMs accounting for rotor modulation are listed in Table 4.1.

Table 4.1 Magnetic Field Harmonics Excited by the Stator PMs

No.	Pole-pairs	Amplitude	Angular speed
1	np_s	$\frac{4F_{PMs}P_0}{\pi}A_n$	0
2	np_s+kp_r	$\frac{4F_{PMs}P_1}{\pi^2}A_nB_k$	$kp_r\Omega_r/(np_s+kp_r)$
3	np_s-kp_r	$\frac{4F_{PMs}P_1}{\pi^2}A_nB_k$	$-kp_r\Omega_r/(np_s-kp_r)$

4.3.2 Flux density of DC field current

Since the DC flux owns the same magnetic path as the stator PM flux and the pole-pairs of DC field p_{dc} is equal to the pole-pairs of stator PMs. The flux density excited by the DC field winding can be obtained in exactly the same way, and can be expressed as

$$B_{dc}(\theta,t)=-\frac{4N_{dc}I_{dc}P_0}{\pi}\sum_{n=1,3,5...}^{\infty}A_n\cos np_s\theta-\frac{4N_{dc}I_{dc}P_1}{\pi^2}\sum_{n=1,3,5...}^{\infty}\sum_{k=1}^{\infty}A_nB_k\left(\cos\alpha_1+\cos\alpha_2\right) \quad (4.4)$$

where N_{dc} and I_{dc} are the coil turns and current value of DC windings. The DC field harmonics own the same pole-pairs and angular velocity with the stator PM field harmonics, but with different amplitudes. Therefore, the DC field winding can act as a regulator of air-gap flux and is open-circuit if flux regulation is not needed.

4.3.3 Flux density of rotor PMs

Similarly, the MMF produced by the rotor PMs is assumed to be square wave, as shown in Fig. 4.4. The Fourier series expansion $F_{PMr}(\theta,t)$ is given by

$$F_{PMr}(\theta,t)=\sum_{n=1,3,5}^{\infty}\frac{-4F_{PMr}}{n\pi}\sin np_r\frac{\theta_r}{2}\cos np_r\left(\theta-\Omega_r t-\theta_0\right) \quad (4.5)$$

where F_{PMr} refers to the rotor PM MMF.

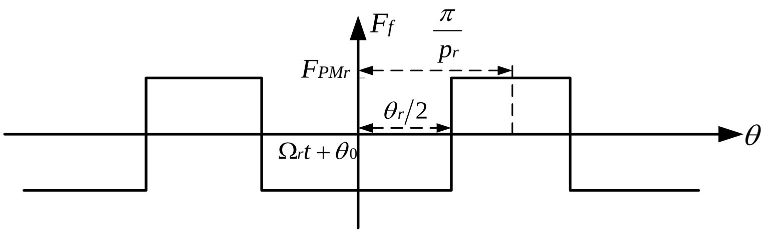

Figure 4.4 Air-gap MMF produced by rotor PMs.

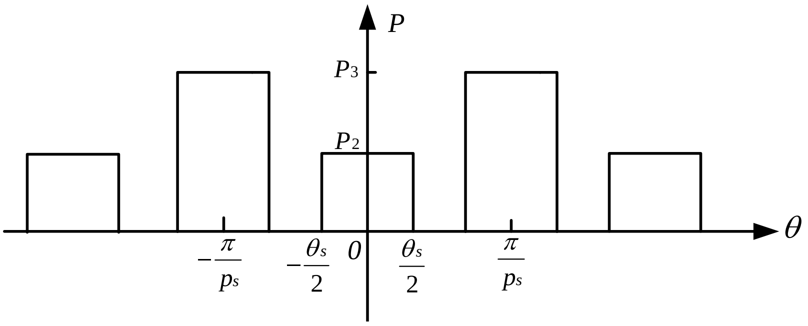

Figure 4.5 Air-gap permeance model of stator.

The air-gap permeance model of stator accounting for stator saliency is presented in Fig. 4.5, and its Fourier series can be used as the stator permeance function.

$$P_s(\theta)=\frac{P_2+P_3}{2}-\sum_{k=1}^{\infty}\frac{2(P_3-P_2)}{k\pi}\sin kp_s\frac{\theta_s}{2}\cos kp_s\theta \tag{4.6}$$

where P_2 and P_3 are the value of stator permeance corresponding to the position of stator PMs and stator tooth. By multiplying $F_{PMr}(\theta,t)$ and $P_s(\theta)$, the flux density excited by the rotor PMs $B_{PMr}(\theta,t)$ after the modulation of stator can be obtained.

$$\begin{cases} B_{PMr}(\theta,t)=F_{PMr}(\theta,t)P_s(\theta) \\ =-\dfrac{2F_{PMr}(P_2+P_3)}{\pi}\displaystyle\sum_{n=1,3,5}^{\infty}C_n\cos np_r(\theta-\Omega_r t-\theta_0) \\ \quad+\dfrac{4F_{PMr}(P_3-P_2)}{\pi^2}\displaystyle\sum_{n=1,3,5\ldots}^{\infty}\sum_{k=1}^{\infty}C_nD_k(\cos\alpha_3+\cos\alpha_4) \\ \alpha_3=(np_r+kp_s)\left[\theta-\dfrac{np_r(\Omega_r t+\theta_0)}{np_r+kp_s}\right] \\ \alpha_4=(np_r-kp_s)\left[\theta+\dfrac{kp_r(\Omega_r t+\theta_0)}{np_r-kp_s}\right] \\ C_n=\dfrac{1}{n}\sin\left(np_r\dfrac{\theta_r}{2}\right),D_k=\dfrac{1}{k}\sin\left(kp_s\dfrac{\theta_s}{2}\right) \end{cases} \tag{4.7}$$

From Eq.(4.7), we can find that the flux density excited by the rotor PMs also contains three groups. One is the original harmonics of the rotor PMs, with np_r pole-pairs and rotates with the same speed of rotor. The other two groups are $np_r + kp_s$ and $np_r - kp_s$ pole-pair harmonics, with angular speeds of $np_r\Omega_r/(np_r + kp_s)$ and $np_r\Omega_r/(np_r - kp_s)$,respectively. These two harmonic groups are produced by the modulating effect of the stator. The detailed harmonic pole-pairs and corresponding angular velocities are listed in Table 4.2.

Table 4.2 MAGNETIC FIELD HARMONICS EXCITED BY THE ROTOR PMS

No.	Pole-pairs	Amplitude	Angular speed
1	np_r	$\frac{2F_{PMr}(P_2+P_3)}{\pi}C_n$	Ω_r
2	$np_r + kp_s$	$\frac{4F_{PMr}(P_3-P_2)}{\pi^2}C_nD_k$	$np_r\Omega_r/(np_r + kp_s)$
3	$np_r - kp_s$	$\frac{4F_{PMr}(P_3-P_2)}{\pi^2}C_nD_k$	$np_r\Omega_r/(np_r - kp_s)$

4.3.4 Flux density of armature current

At last, the flux density excited by the armature currents is investigated. The MMF produced by each phase of armature current without considering stator modulation is shown in Fig. 4.6.

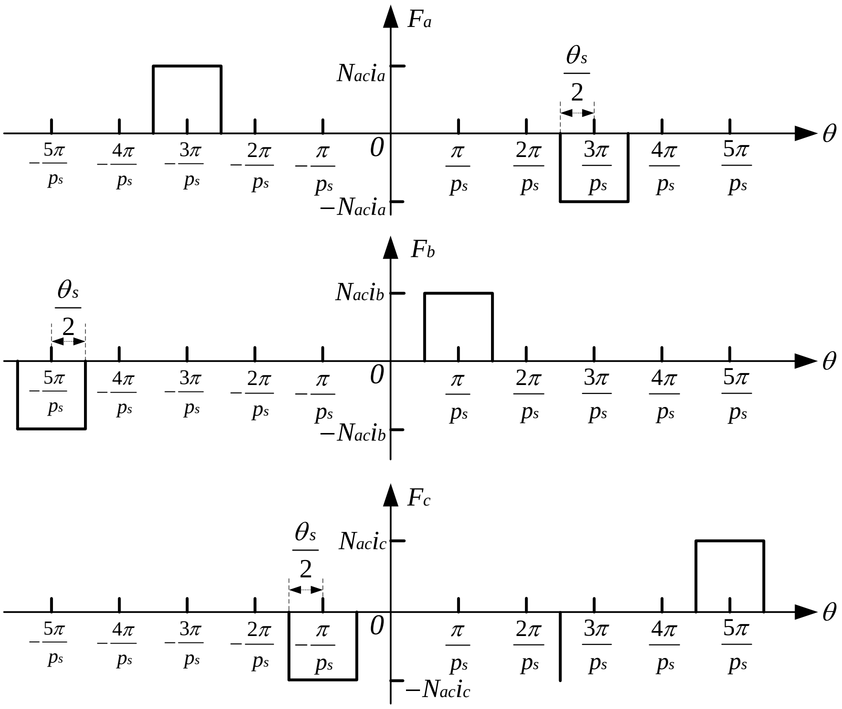

Figure 4.6 Air-gap MMF produced by armature current of the proposed machine.

The Fourier series expansion of each phase MMF is given by

$$\begin{cases} F_a(\theta)=\sum\limits_{n=1,3,5...}^{\infty}(-1)^{\frac{n+1}{2}}\dfrac{4N_{ac}i_a}{n\pi}\sin\left(\dfrac{np_s\theta_s}{12}\right)\sin\left(n\dfrac{p_s}{6}\theta\right) \\ F_b(\theta)=\sum\limits_{n=1,3,5...}^{\infty}(-1)^{\frac{n+1}{2}}\dfrac{4N_{ac}i_b}{n\pi}\sin\left(\dfrac{np_s\theta_s}{12}\right)\sin\left[n\left(\dfrac{p_s}{6}\theta-\dfrac{2\pi}{3}\right)\right] \\ F_c(\theta)=\sum\limits_{n=1,3,5...}^{\infty}(-1)^{\frac{n+1}{2}}\dfrac{4N_{ac}i_c}{n\pi}\sin\left(\dfrac{np_s\theta_s}{12}\right)\sin\left[n\left(\dfrac{p_s}{6}\theta-\dfrac{4\pi}{3}\right)\right] \end{cases} \tag{4.8}$$

where i_a, i_b and i_c are the current of each phase, respectively. N_{ac} refers to the turns of each coil. The armature windings are fed with balanced three phase sinusoidal current, the complete MMF waveform in the air-gap excited by the armature currents can be obtained by spatially combining the MMF waveforms of all the phase currents, as given below

$$\begin{cases} F_{ac}(\theta,t)=\sum_{j=1,5,7\ldots}^{\infty}\frac{3}{2}E_j\sin\left(j\frac{p_s}{6}\theta-h\omega t\right) \\ E_j=(-1)^{\frac{j+1}{2}}\frac{4N_{ac}I_{ac}}{j\pi}\sin\left(\frac{jp_s}{12}\theta_s\right) \\ h=\begin{cases} 1 & j=6i-1, \quad i=0,1,2\ldots \\ -1 & j=6i+1, \quad i=0,1,2\ldots \end{cases} \end{cases} \tag{4.9}$$

where I_{ac} and ω refer to the peak value and angular velocity of the armature current, respectively. Since both the stator and the rotor own field modulating effect, the armature field will be modulated twice. By multiplying the MMF of armature current $F_{ac}(\theta,t)$, the permeance function of stator $P_s(\theta)$ and the permeance function of the rotor $P_r(\theta,t)$, the flux density excited by the armature current can be obtained [65, 85].

$$\begin{cases} B_{ac}(\theta,t) \\ =F_{ac}(\theta,t)P_s(\theta)P_r(\theta,t) \\ =\frac{3P_0(P_2+P_3)}{4}\sum_{j=1,5,7\ldots}^{\infty}E_j\sin\left[j\frac{p_s}{6}\left(\theta-\frac{h\omega}{j\frac{p_s}{6}}t\right)\right] \\ \quad -\frac{3P_0(P_3-P_2)}{2\pi}\sum_{j=1,5,7\ldots}^{\infty}\sum_{k=1}^{\infty}E_jD_k\sin\left[\left(j\frac{p_s}{6}\theta\pm kp_s\right)\left(\theta-\frac{h\omega}{\left(j\frac{p_s}{6}\pm kp_s\right)}t\right)\right] \\ \quad +\frac{3P_1(P_2+P_3)}{4\pi}\sum_{j=1,5,7\ldots}^{\infty}\sum_{k=1}^{\infty}E_jB_k\sin\left[\left(j\frac{p_s}{6}\theta\pm kp_r\right)\left(\theta-\frac{(h\omega t\pm kp_r\Omega_r)}{\left(j\frac{p_s}{6}\pm kp_r\right)}t\right)\pm kp_r\theta_0\right] \\ \quad -\frac{3P_1(P_3-P_2)}{2\pi^2}\sum_{j=1,5,7\ldots}^{\infty}\sum_{k_1=1}^{\infty}\sum_{k_2=1}^{\infty}E_jD_{k1}B_{k2}\sin\left[\left(j\frac{p_s}{6}\theta\pm k_1p_s\pm k_2p_r\right)\left(\theta-\frac{(h\omega t\pm k_2p_r\Omega_r)}{\left(j\frac{p_s}{6}\pm k_1p_s\pm k_2p_r\right)}t\right)\pm k_2p_r\theta_0\right] \end{cases} \tag{4.10}$$

As given in Eq.(4.10), the flux density excited by the armature current can be categorized into four groups. The first group is the original harmonics without the modulation of neither the stator nor the rotor, the second and the third groups are the armature fields modulated by the stator and the rotor, respectively, the last group is harmonics modulated by both the stator and the rotor. The detailed harmonic pole-pairs and corresponding velocities are listed in Table 4.3.

Table 4.3 Magnetic Field Harmonics Excited by the Armature Current

No.	Pole-pairs	Amplitude	Angular speed
1	$jp_s/6$	$\frac{3P_0(P_2+P_3)}{4}E_j$	$\frac{h\omega}{j\frac{p_s}{6}}$
2	$j\frac{p_s}{6}\pm kp_s$	$\frac{3P_0(P_3-P_2)}{2\pi}E_jD_k$	$\frac{h\omega}{\left(j\frac{p_s}{6}\pm kp_s\right)}$
3	$j\frac{p_s}{6}\pm kp_r$	$\frac{3P_1(P_2+P_3)}{4\pi}E_jB_k$	$\frac{(h\omega\pm kp_r\Omega_r)}{\left(j\frac{p_s}{6}\pm kp_r\right)}$
4	$j\frac{p_s}{6}\pm k_1p_s\pm k_2p_r$	$\frac{3P_0P_1(P_3-P_2)}{2\pi^2}E_jD_{k1}B_{k2}$	$\frac{(h\omega\pm k_2p_r\Omega_r)}{\left(j\frac{p_s}{6}\pm k_1p_s\pm k_2p_r\right)}$

4.3.5 Slot-pole combination

In order to produce stable electromagnetic torque, the two interacted field harmonics should have the same pole-pair number and the same rotating velocity. It can be found that if

$$\begin{cases} j\dfrac{p_s}{6}+k_1p_s=k_2p_r \\ \omega=\Omega_rp_r \end{cases} \tag{4.11}$$

where both k_1 and k_2 are positive integers, the harmonic group 1 in Table 4.3 is synchronous with the harmonic group 3 in both Table 4.1 and Table 4.2 when $k=h=1$. The harmonics with $j\frac{p_s}{6}+kp_s$ pole-pairs in group 2 of Table 4.3 is also synchronous with the harmonic group 1 in Table 4.2. The harmonics with $j\frac{p_s}{6}-kp_r$ pole-pairs in group 3 of Table 4.3 and the harmonic group 1 in Table 4.1 own the same pole-pair number and rotational velocity as well. Therefore, all of these synchronous harmonics will contribute to the electromagnetic torque production.

The $j\frac{p_s}{6}$ is also referred as the pole-pair number of armature field p_{ac}. As shown in Fig. 4.1, the rotor slot number N_r is equal to the pole-pair number of rotor PMs p_r. Since each stator PM is separated by one stator tooth, the total stator slot number N_s should be twice the pole-pair number of the stator PMs.

$$N_s = 2p_s \tag{4.12}$$

Therefore, the slot-pole combination of the proposed machine can be determined. If the pole-pair number of stator PMs is chosen as 6, then the stator slot number is 12, the pole-pair number of armature field is 5 or 7 corresponding to $j=5$ and $j=7$, hence the rotor PM pole-pairs is 11 or 13, respectively. There are also some other slot-pole combinations. With the stator PM pole-pairs is chosen as 12, the stator slot number, the armature field pole-pairs and the rotor PM pole-pairs are 24, 10 or 14, and 22 or 26, respectively. A general equation group associated with the slot-pole combination is given by

$$\begin{cases} p_{ac} + p_s = p_r \\ p_{ac} = j\dfrac{p_s}{6} \qquad j = 5 \quad or \quad 7 \\ N_s = 2p_s \\ N_r = p_r \end{cases} \tag{4.13}$$

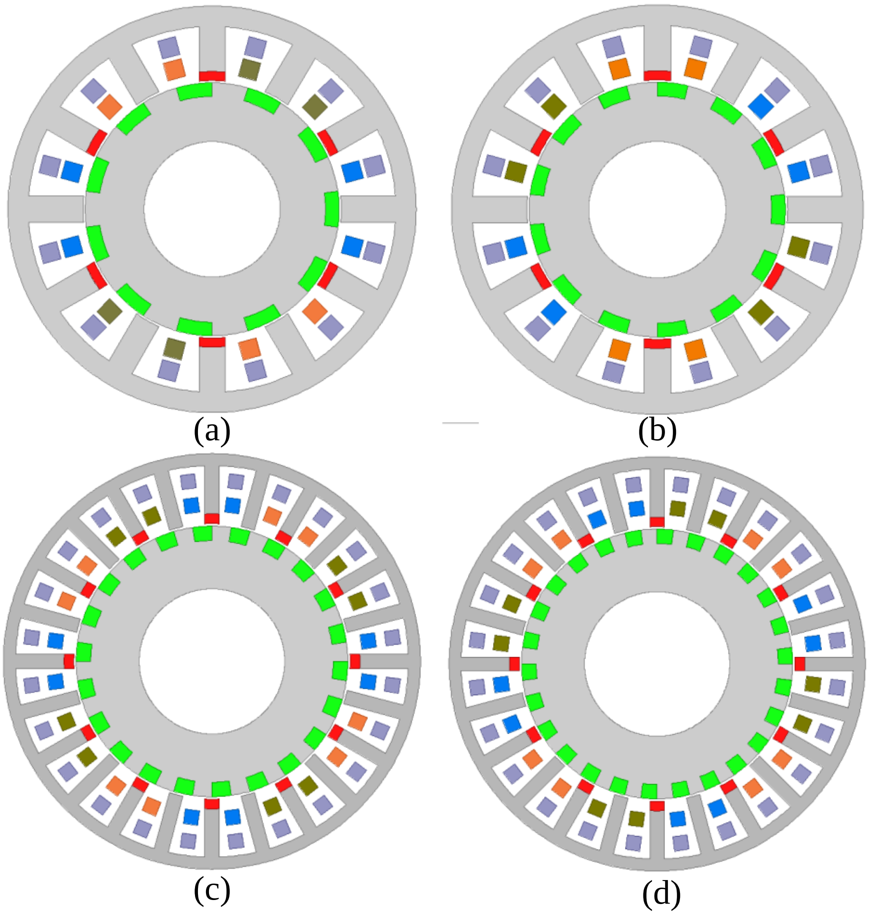
(a) (b) (c) (d)

Figure 4.7 Machine configurations with different pole/slot combinations. (a) 5/6/11. (b) 7/6/13. (c) 10/12/22. (d) 14/12/26.

Because there are various stator and rotor pole-pair combinations for the proposed machine, one of the preliminary design work is to chose the most feasible $p_{ac} / p_s / p_r$ to achieve better electromagnetic performances. According to Eq.(4.13), the pole-pairs of stator PM is multiple of 6. When the stator PM has 6 pole-pairs, the pole-pair combination of the proposed machine can be 5/6/11 and 7/6/13. When the stator PM has 12 pole-pairs, the pole-pair combination of the proposed machine can be 10/12/22 and 14/12/26. The machine configurations having different pole-pair combinations are shown in Fig. 4.7. Unbalanced magnetic pull (UMP), cogging torque, d axis inductance and torque capability of these four machines are simulated and compared in Table 4.4. For a fair comparison, the overall dimensions and the PM volumes as well as the copper losses are the same. One can find that UMP exists in the 5/6/11 and 7/6/13 machine configurations, in which the UMP of the 5/6/11 machine is smaller. The 10/12/22 and 14/12/26 machines have no UMP, because as reported in [86], when the winding structure can be regarded as a duplication of another structure, no UMP will be resulted. Cogging torque and the maximum electromagnetic torque of these four machines are also simulated, among which the 5/6/11 machine has the lowest torque ripple rate (the ratio of peak-peak value of cogging torque to the maximum average torque). Therefore, the chosen pole-pair combination of the proposed machine is 5/6/11.

Table 4.4 PERFORMANCE COMPARISON

Items	5/6/11	7/6/13	10/12/22	14/12/26
UMP	400N	446N	0	0
Cogging torque	0.3Nm	0.28Nm	0.43Nm	0.41Nm
d-axis inductance	33mH	31mH	45mH	46mH
Maximum torque	4.1Nm	3.15Nm	4.64Nm	3.74Nm

4.4 PERFORMANCE ANALYSIS

The electromagnetic performances of this proposed HEDPM machine are studied using TS-FEM. The pole-pair number of stator PMs and rotor PMs are 6 and 11, respectively. The detailed design parameters of the proposed HEDPM machine are given in Table 4.5.

TABLE 4.5 DESIGN PARAMETERS

Stator outside diameter	90 mm
Stator inside diameter	57 mm
Rotor outside diameter	56 mm
Rotor inside diameter	30 mm
Length of air-gap	0.5 mm
Stack length	80 mm
Thickness of stator PMs	2 mm
Thickness of rotor PMs	3 mm
Arc of stator tooth/PMs	11.7 °
Arc of rotor PMs	16.36 °
Number of stator PM pole-pairs	6
Number of rotor PM pole-pairs	11
Number of armature winding pole-pairs	5
Number of DC winding pole-pairs	6
Number of stator slots	12
Number of phases	3
Turns of ac conductors	160
Turns of dc conductors	160
Remanence of NdFeB	1.2T
Relative permeability of NdFeB	1.05

4.4.1 Magnetic Flux

The no load and full load flux distributions are investigated, as well as the flux distributions at different DC excitations, as given in Fig. 4.8. We can find that both flux strengthening and flux weakening can be achieved by controlling the DC currents. The air-gap field distributions and harmonic spectrums when excited by the stator PMs, rotor PMs and armature currents are given in Fig. 4.9. One can find a good agreement between the simulated results and the results derived in section 4.3.

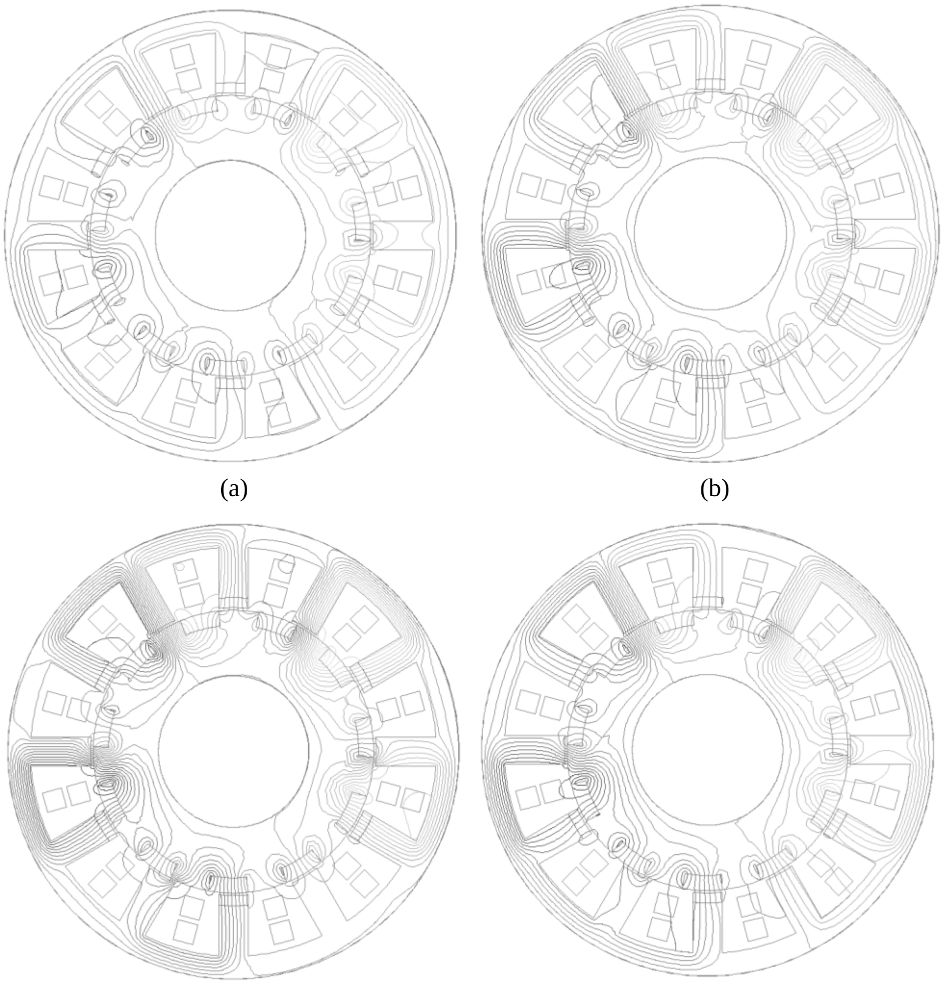

(a) (b)

(c) (d)

Figure 4.8 Flux distributions. (a) $I_{dc} = 3A$, $I_{ac} = 0A$. (b) $I_{dc} = 0A$, $I_{ac} = 0A$. (c) $I_{dc} = -3A$, $I_{ac} = 0A$. (d) $I_{dc} = 0A$, $I_{ac} = 2A$.

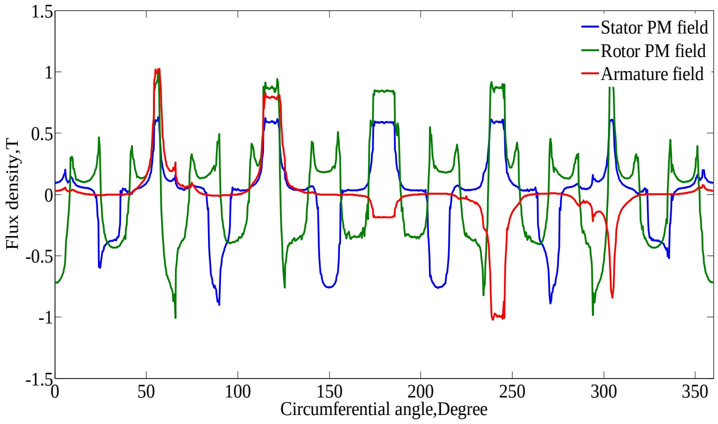

(a)

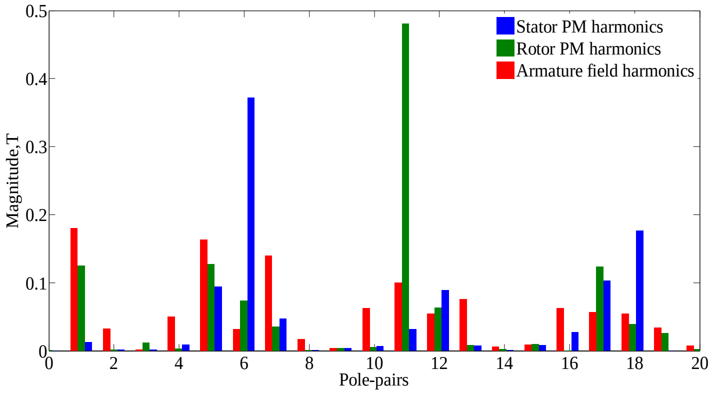

(b)

Figure 4.9 Air-gap flux density distributions and harmonic spectrums. (a) Flux density distributions. (b) Harmonics.

Fig. 4.10(a) and Fig. 4.10(b) show the flux density distributions and harmonics with and without DC currents, when excited only by the stator PMs and the rotor PMs, respectively. The working harmonics should have the same pole-pairs and the same rotating speeds as the harmonics generated by the armature current. For the field excited by the stator PMs, the working harmonics are 5th, 6th, 7th, 16th, 17th and 18th harmonics, while for the field excited by the rotor PMs, the working harmonics are 1th, 5th, 6th, 7th, 11th, 17th and 18th harmonics. Both flux strengthening and flux weakening can be achieved by changing the polarity of DC current.

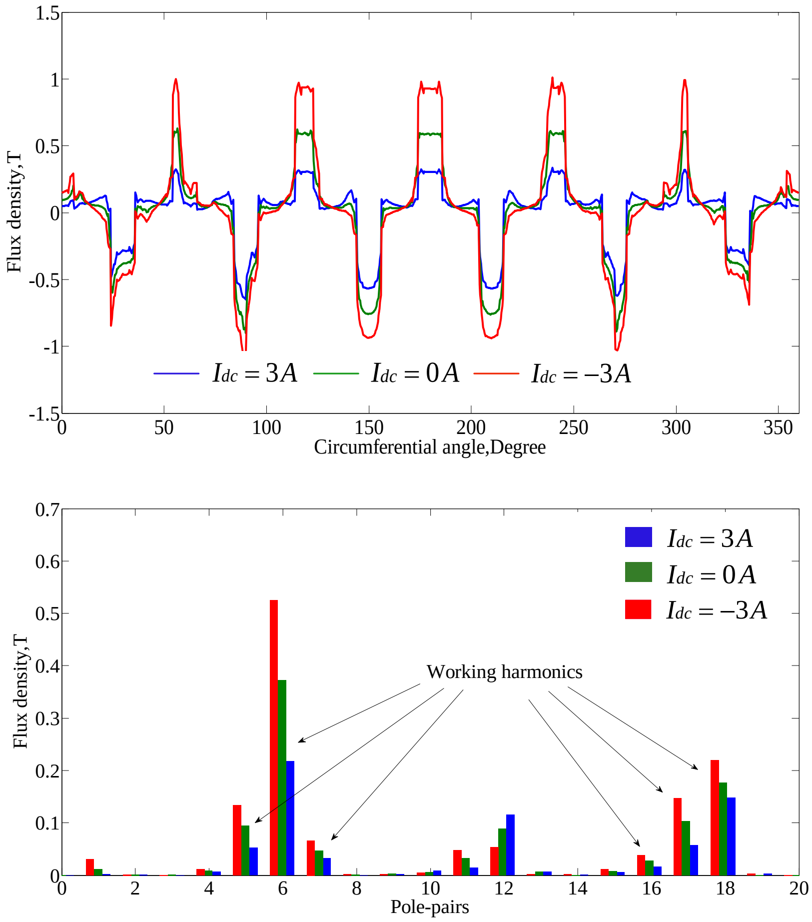

(a)

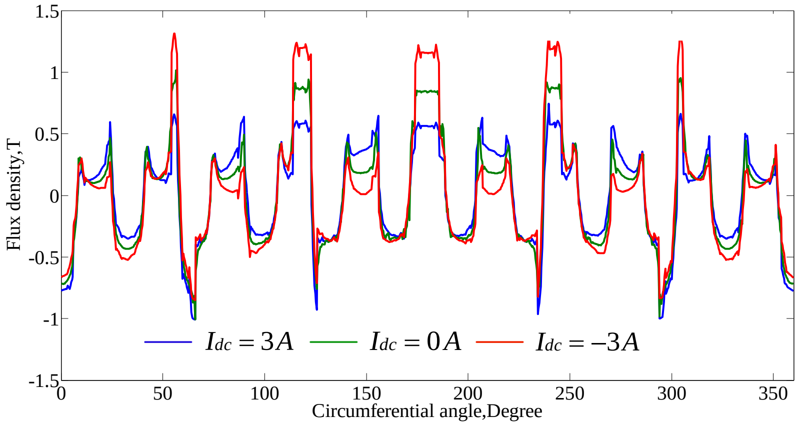

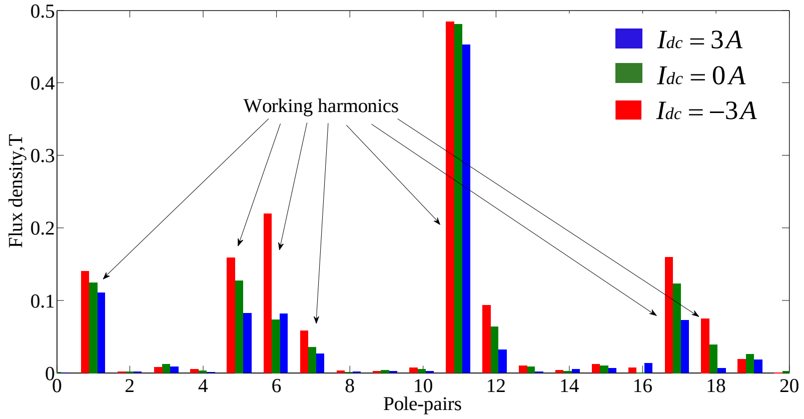

(b)

Figure 4.10 Air-gap flux density distributions and harmonic spectrums. (a) Stator PM field. (b) Rotor PM field.

4.4.2 Flux linkage and back EMF

The open-circuit flux linkage of phase A and the harmonics are given in Fig. 4.11. The flux linkage waveforms are sinusoidal with small DC components. By applying DC current, the flux linkage can be effectively regulated. Fig. 4.12 shows the back EMF when the machine runs at 800rpm. Again, balanced back EMF can be obtained.

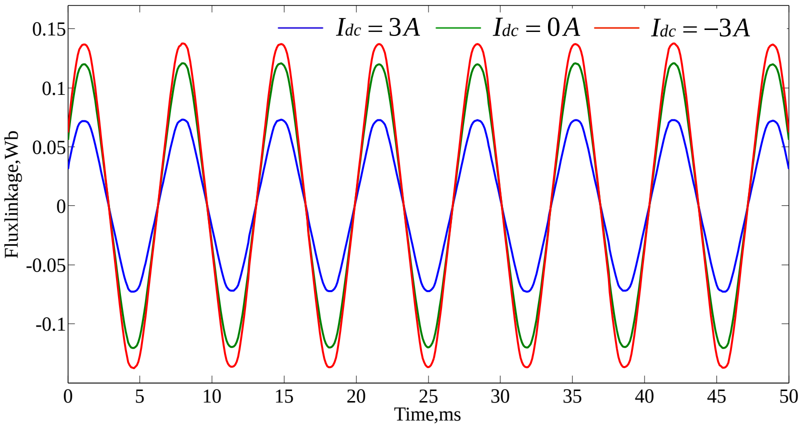

(a)

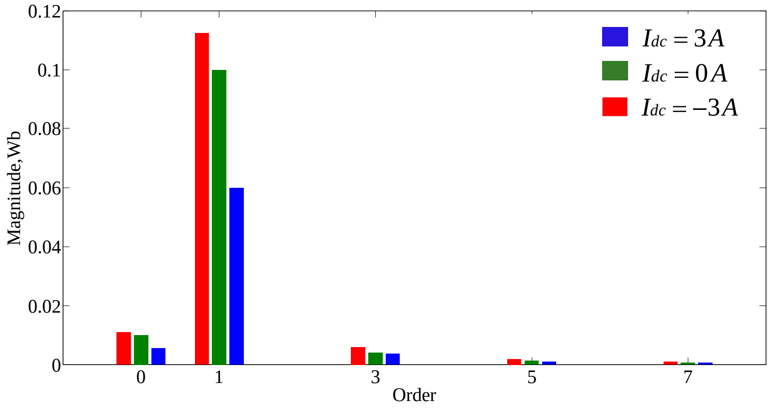

(b)

Figure 4.11 Flux linkage and harmonics. (a) Flux linkage. (b) Harmonics.

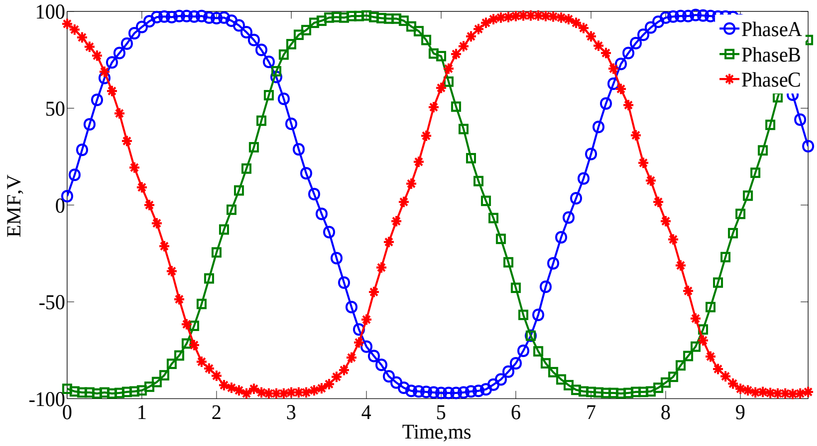

Figure 4.12 Back EMF when the machine runs at 800rpm.

4.4.3 Torque characteristics

The torque angle characteristics when the stator PMs and rotor PMs are magnetized in both the same direction and the opposite direction are investigated, as given in Fig. 4.13. The output torque when the stator PMs and rotor PMs are magnetized in the same direction is larger than the torque when the PMs are magnetized in the opposite direction. Both the stator PMs and the rotor PMs can contribute to the torque production. The frozen permeability method given in [87] can be used to accurately calculate the torque produced by the stator PMs and rotor PMs. The torque characteristics of the proposed dual PM machine, the rotor PM machine when the stator PMs are removed and the stator PM machine when the rotor PMs are removed are separately simulated and compared, as shown in Fig. 4.14. One can find that the proposed machine can also operate well with either stator PM excitation or rotor PM excitation, actually, the proposed machine can be regarded as combination of a stator PM excited machine and a rotor PM excited machine.

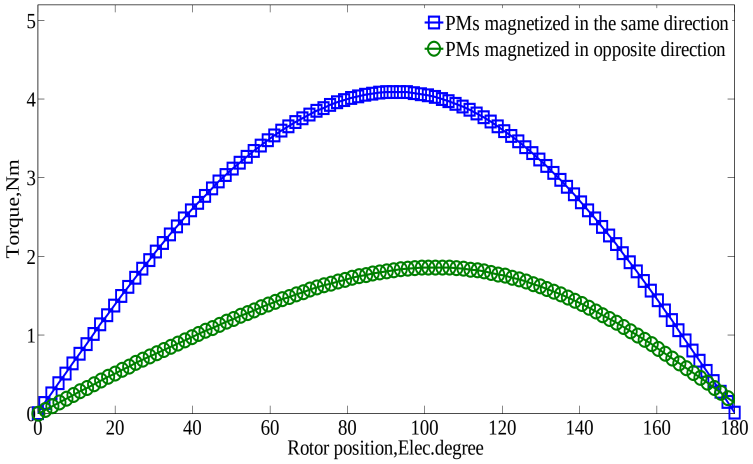

Figure 4.13 Stationary torque. (a) Stator PMs and rotor PMs are magnetized in the same direction. (b) Stator PMs and rotor PMs are magnetized in opposite direction.

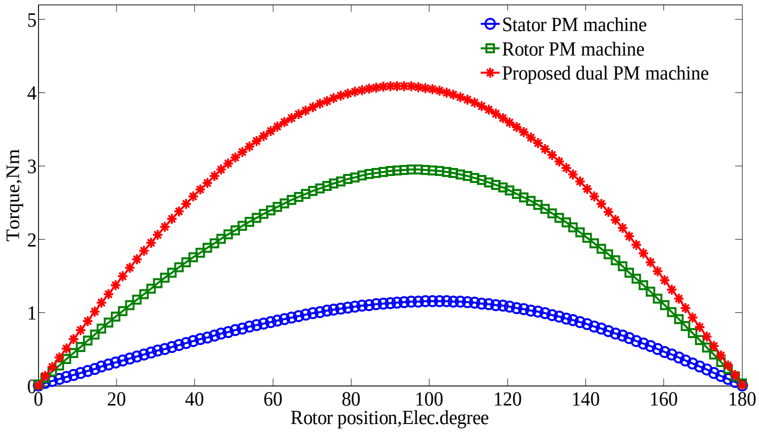

(a)

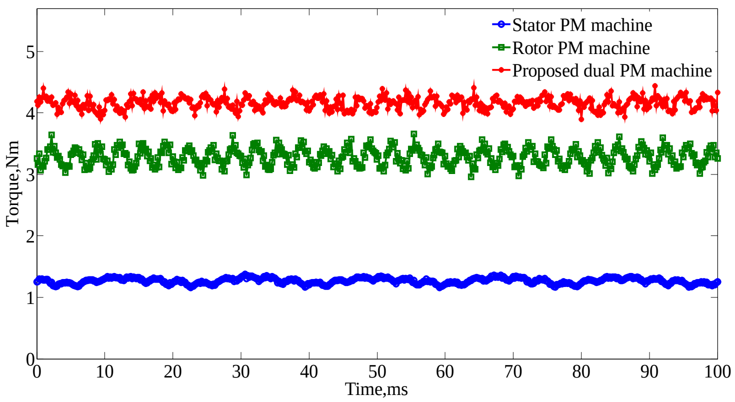

(b)

Figure 4.14 Torque characteristics. (a) Torque-angle waveforms. (b) Steady state torque.

As the field windings will inevitably reduce slot areas for armature windings, and cause torque reduction. To fully investigate the torque capability of the proposed machine, the torque density and "T/PMV" of the proposed machine when the field windings are replaced by the armature windings, which is referred as dual-PM machine, are simulated and compared with SPM and IPM as shown in Table 4.6. We can find that when excited by the same current density, the proposed dual-PM machine can achieve higher torque capability than the SPM and IPM.

TABLE 4.6 COMPARISON OF TORQUE CAPABILITY

Current density[A/mm^2]	Torque density[kNm/m^3]			T/PMV[Nm/L]		
	DPM	SPM	IPM	DPM	SPM	IPM
3.63	13	8.47	10.5	276	252	268
20	63.5	42	51	1348	1250	1302

4.4.4 PM demagnetization analysis

Since the DC excitation inevitably circulates through the stator PMs, the stator PMs may suffer from demagnetization risk. The demagnetization of PMs is influenced by both the demagnetizing force and the working temperature. At lower temperatures, the BH curves are linear and the knee point doesn't appear in the second quadrant of hysteresis loop, the PMs will not be demagnetized at these temperatures unless the demagnetizing force is larger than the coercivity. However, the risk of demagnetization increases at higher temperatures due to the nonlinear BH characteristics of the magnet.

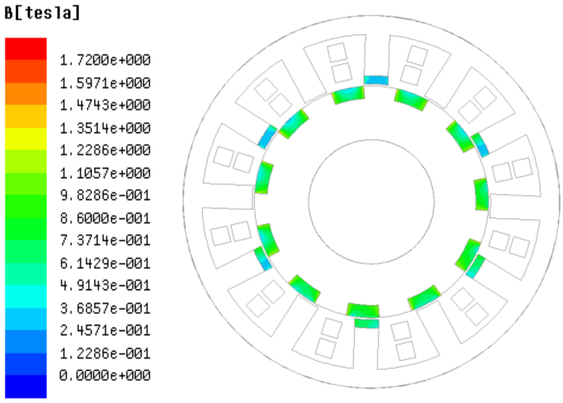

(a)

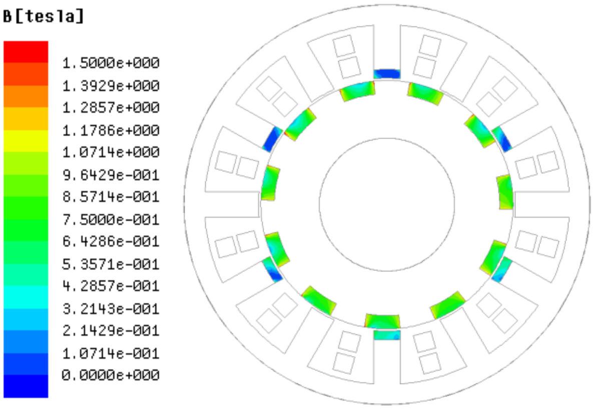

(b)

Figure 4.15 Flux density distributions. (a) $I_{dc} = 4A$. (b) $I_{dc} = 10A$.

Fig.4.15 shows the flux density distributions of the stator PMs and rotor PMs when the machine runs at full load, with DC currents of 4A and 10A, respectively. We can see that when the stator PMs aligns with the rotor teeth, the stator PMs have higher risk of demagnetization because the magnetic reluctance is very small in this case. In [88], the demagnetization curves of NdFeB from room temperature to 200℃ are investigated, which shows the knee point flux density of NdFeB at 180℃and 200℃ are 0.3T and 0.4T, respectively.

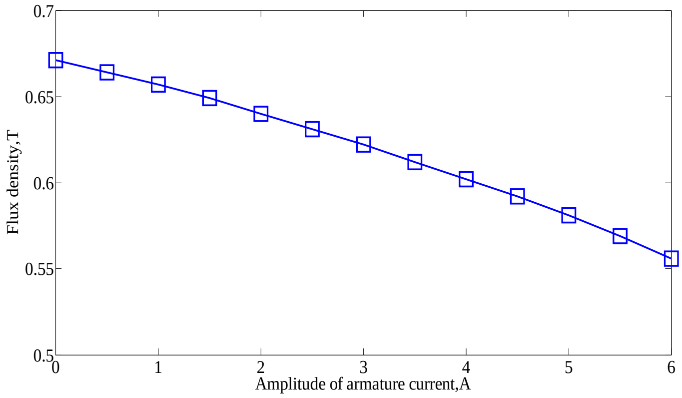

(a)

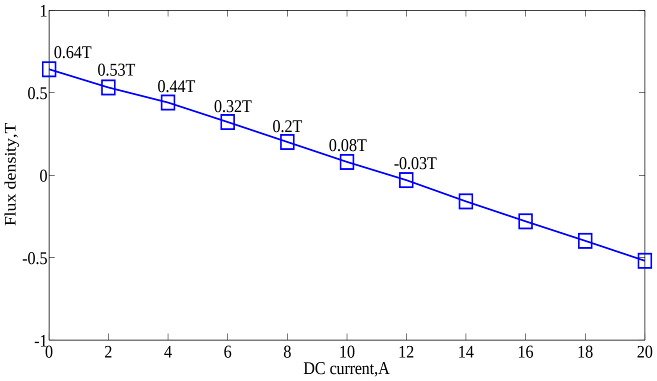

(b)

Figure 4.16 Minimun PM flux density with different armature currents and DC currents. (a) Influence of armature current. (b) Influence of DC current.

The influence of the armature current on the stator PMs are investigated and shown in Fig. 4.16 (a). We can find that the flux density of the working point decreases with the increase of armature currents. As long as the flux density of the working point is larger than the flux density of the knee point, the PMs will not have demagnetization risk. Take 180℃ as reference, the flux density of the knee point is 0.3T at 180℃. The stator PMs will not be demagnetized by the armature fields because the minimum flux density of the working point is 0.557T when the armature current is 6A, which is still larger than the flux density of the knee point. The minimum flux density of stator PMs when applied with rated armature current and different DC currents are given in Fig. 4.16(b), which shows the stator PMs will not be demagnetized if the DC current is lower than 6A at 180℃.

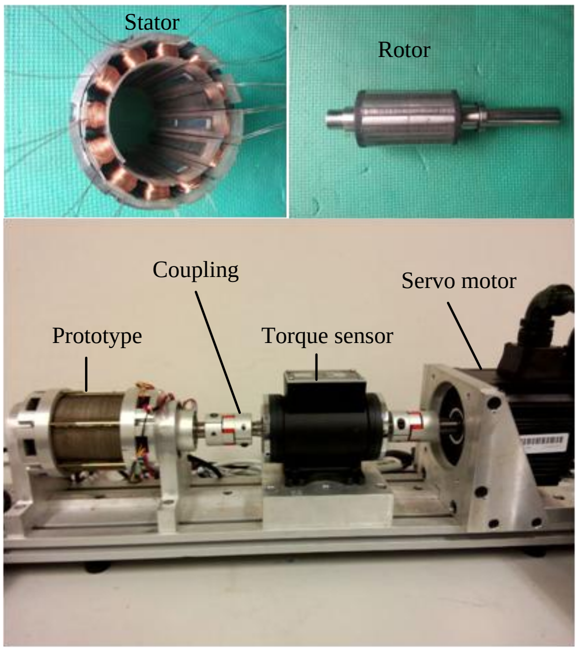

Figure 4.17 Prototype of the proposed HEDPM machine and test bench.

4.5 EXPERIMENTAL VERIFICATION

4.5.1 Test bench

For further investigation and verification of the proposed machine concept, a prototype of the proposed HEDPM machine is fabricated and tested. A 1.5 kW servo machine connected to a Siemens 1212C PLC controller is used to provide adjustable load torque. Torque sensor is used to test the electromagnetic torque, and an oscilloscope is used to display the tested waveforms. The stator, rotor and test bench are shown in Fig. 4.17. The main dimensions of the proposed machine is given in Table 4.5, which are the same as the model dimensions used in previous finite element analysis.

4.5.2 Torque measurement

Firstly, the torque values corresponding to different rotor positions are tested and compared with the simulated results, as shown in Fig. 4.18. One can find good agreement between the results of FEM and experimental test. The steady state electromagnetic torque T_e and cogging torque T_c are tested and given in Fig. 4.19, the peak-peak value of cogging torque is 0.3Nm, which is 7.3% of the maximum average torque and which is acceptable for practical applications.

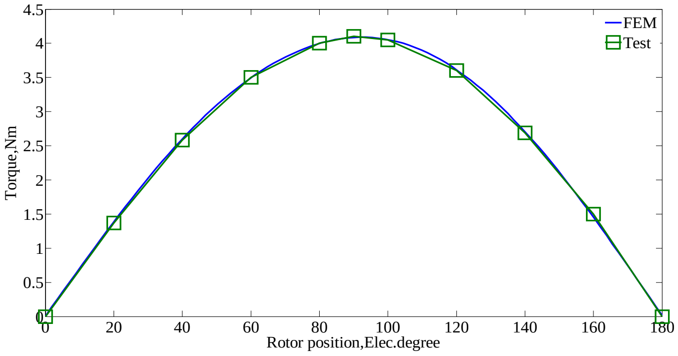

Figure 4.18 Torque angle waveform.

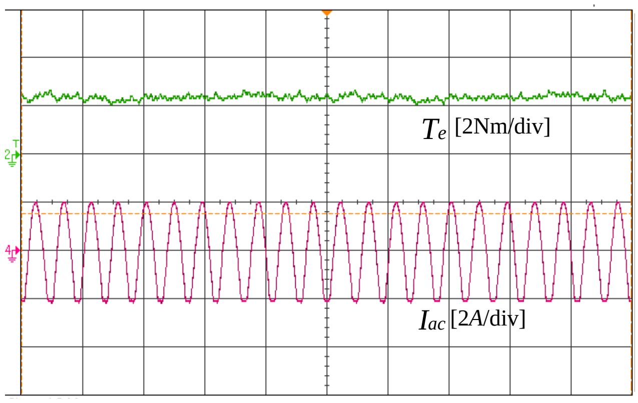

(a)

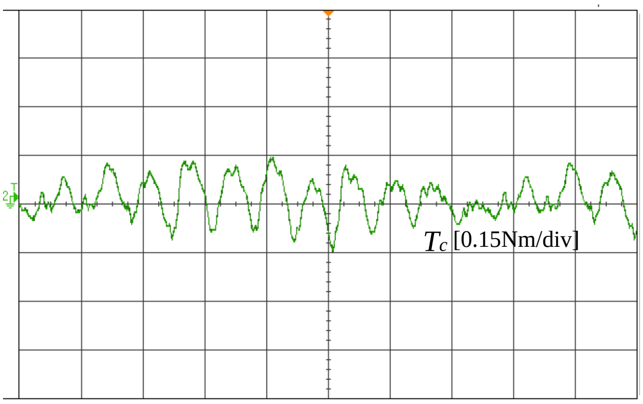

(b)

Figure 4.19 Steady state electromagnetic torque and Cogging torque. (a) Steady electromagnetic torque. (b) Cogging torque.

4.5.3 Back EMF measurement

Fig. 4.20(a) shows the no load back EMF of phase A with and without DC currents when the machine runs at 800rpm. The no load back EMF of phase B and phase C are the same, but with 120 degree and 240 degree lagging angle, respectively. Again, we can see good agreement between the results of experimental tests and finite element calculations. The no load back EMF can be regulated effectively by applying DC current.

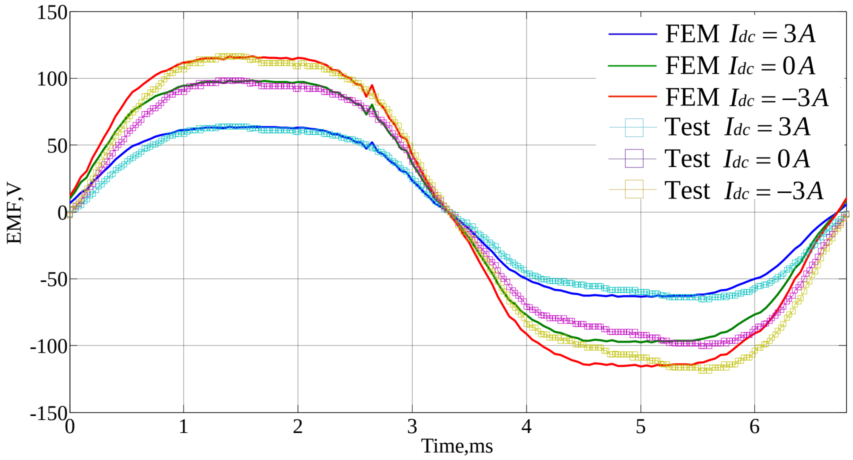

(a)

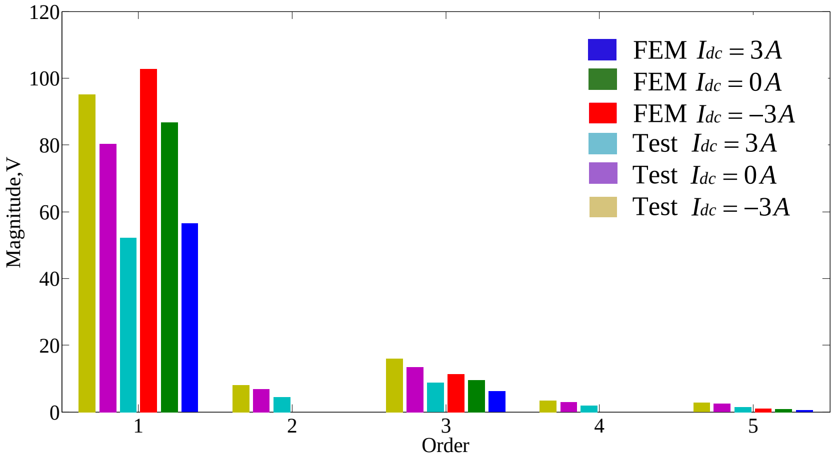

(b)

Figure 4.20 Back EMF with and without flux weakening. (a) EMF waveforms. (b) Harmonics.

Harmonics of the back EMF waveforms are given in Fig. 4.20(b). One can find that the tested EMFs have even-order harmonics with small magnitudes, which causes the difference between the FEA results and test results. The reason behind this may be that the PMs of the prototype are not so well evenly magnetized, so there are more field harmonics in the air-gap of the prototype and the induced voltage is then affected accordingly. The machining error and assembling error can also affect the tested EMFs.

4.5.4 Efficiency map

Fig. 4.21 shows the efficiency maps of the proposed machine when using DC flux control and I_d flux control. One can find that when using DC flux control, the operating region of the proposed machine is expanded, an additional flux strengthening region can be obtained, which allows the proposed machine operates under larger load torque. The efficiency at flux strengthening region is reduced due to the additional DC excitation copper loss. Compared with I_d flux control, the flux weakening region is also expanded and higher efficiency can be obtained when using DC flux control, which means the DC field regulation method of the proposed machine is effective.

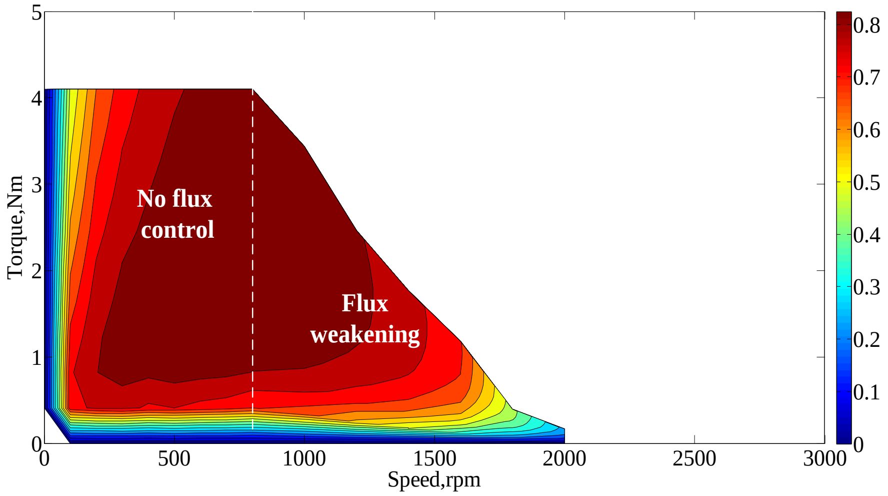

(a)

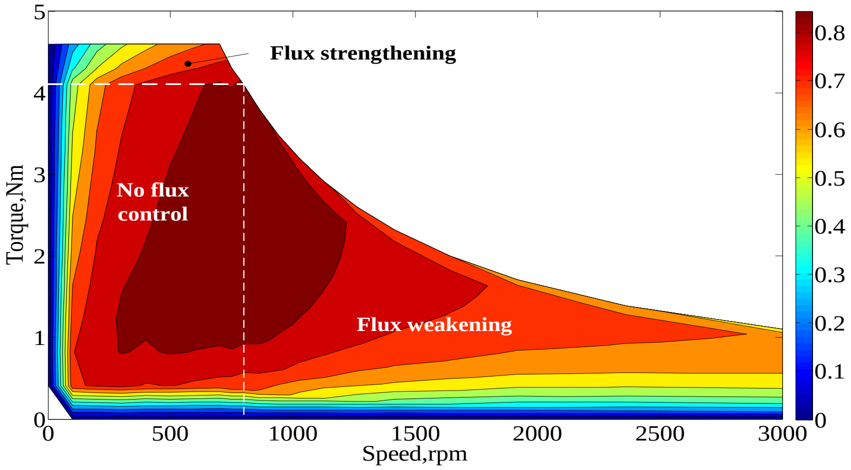

(b)

Figure 4.21 Efficiency map. (a) I_d flux control. (b) DC flux control.

The power-speed curve of the proposed machine is given in Fig. 4.22. One can find that the proposed machine can maintain constant power operation over a wide speed range. The detailed machine specifications are given in Table 4.7.

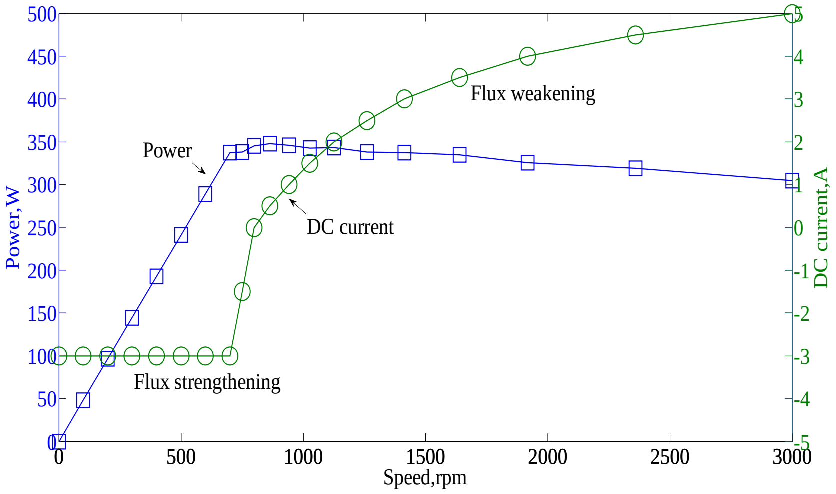

Figure 4.22 Power-speed and DC field current.

TABLE 4.7 MACHINE SPECIFICATIONS

Items	Values
Rated power	340 W
Rated current	1.4 A
Rated torque	4.1 Nm
Rated speed	800 rpm
Armature windings resistance	5.3 Ω
Field windings resistance	5.3 Ω
d-axis inductance	33 mH
q-axis inductance	31 mH

4.6 SUMMARY

In this paper, a novel hybrid-excited dual-PM machine incorporated with flux modulating effect is proposed. Both the armature windings and DC field windings are housed in the stator slots. The air-gap flux can be both strengthened and weakened by controlling the DC currents. Both the stator and rotor own PM excitations, the magnetic fields excited by the stator PMs, rotor PMs and armature windings can be coupled efficiently due to the flux modulating effect of the rotor and stator. Besides the original fundamental harmonics, many other synchronous harmonics are generated and contribute to the effective electromagnetic torque production.

The working principle of the proposed machine is deeply discussed through analyzing the modulating effect of the stator and rotor. The air-gap field harmonics excited by different magnetic sources are investigated. FEM is used to analyze the machine performances and verified by experimental tests. The results show that both the stator PMs and the rotor PMs can contribute to the electromagnetic torque generation, high torque capability can be achieved. Both flux strengthening and flux weakening can be realized by controlling the DC field current. During flux strengthening, the output torque can be enhanced, but the efficiency is reduced as the DC current will introduce additional copper loss. The flux weakening enables the proposed machine to run at high speeds. Compared with I_d flux control, the DC flux control is effectively enlarge the constant power speed range of the proposed machine.

CHAPTER 5 APPLICATION OF HYBRID EXCITED FLUX BIDIRECTIONAL MODULATED MACHINE IN WIND POWER GENERATION

5.1 INTRODUCTION

Since fossil energy is nonrenewable and will cause environmental pollution, the development of clean energy systems is on an accelerating pace. Wind power as an environmentally clean and cost-effective energy source, has attracted much attention in recent decades [89-92]. According to the statistic data provided by the Global Wind Energy Council(GWEC), the global annual installed wind capacity has increased from 3.76GW at 2000 to 63.467GW at 2015, and the growth trend will continue in the future [93]. Fig. 5.1 shows of the global wind capacity from 2015 to 2020, one can see that the wind power systems are growing fast and enjoy good potential for further sustained development.

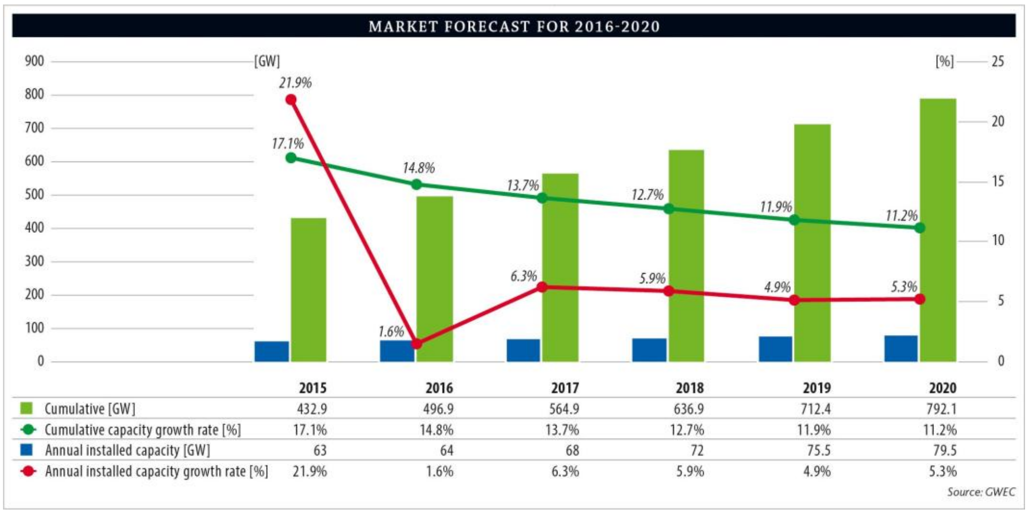

	2015	2016	2017	2018	2019	2020
🟩 Cumulative [GW]	432.9	496.9	564.9	636.9	712.4	792.1
● Cumulative capacity growth rate [%]	17.1%	14.8%	13.7%	12.7%	11.9%	11.2%
🟦 Annual installed capacity [GW]	63	64	68	72	75.5	79.5
● Annual installed capacity growth rate [%]	21.9%	1.6%	6.3%	5.9%	4.9%	5.3%

Source: GWEC

Figure 5.1 Global wind power capacity[93].

Motivated by the increasing contribution of wind power generation systems

(WPGSs), the wind generator (WG) as a key component of WPGS, is developed rapidly [77, 78, 94-96]. The squirrel cage induction generator (SCIG) is a popular machine in WPGS due to its robust construction, low cost and mechanical simplicity. No brushes are needed for the operation of SCIG, and little maintenance is required [97]. The SCIG is mainly suitable for constant speed WPGS, when the SCIG is used in variable speed WPGS, a full-scale back-to-back converter is needed to connect the SCIG and the grid, which will increase the cost and reduce the efficiency. Another widely used WG is the doubly fed induction generator (DFIG), which is suitable for variable speed WPGS [98-100]. The stator of the DFIG is directly connected to the grid while the rotor is connected to the grid through a back-to-back converter. The DFIG can perform well in a wide speed range from super-synchronous to sub-synchronous speeds. Brushes or slip rings are needed in the DFIG, which is one of the main drawbacks of DFIG, and may result in electrical losses and machine failures. Both the SCIG based WPGS and the DFIG based WPGS cannot achieve direct drive, because it is difficult to design the SCIG and DFIG with multipole low-speed and high torque capability. Gearboxes are usually used together with the SCIG and DFIG to reduce the speed and amplify the output torque, which inevitably reduce the efficiency and need routine maintenance. Therefore, direct-drive WPGS is more attractive due to the increased reliability.

In last chapter, HEDPM is proposed and investigated. In order to protect the stator PMs from demagnetizing, the applied field current cannot be too large as discussed in section 4.4.4. In wind power generation system which needs to adjust air-gap flux frequently, HEDPM has some limitations since the stator PMs may be demagnetized by the field current. In this chapter, a new machine for wind power generation is studied which removes the stator PMs from the HEDPM, and is referred as hybrid excited flux bidirectional modulated generator (HE-FBMG). The configuration and design considerations are firstly discussed. The control strategies including constant voltage control and maximum power point tracking (MPPT) control are studied. In order to achieve better overall performances, an improved Tabu search(ITS) algorithm[101] is used to optimal design the proposed generator, and its electromagnetic performances are investigated using FEM. Finally, the prototype is manufactured and its performances are studied through experimental tests. The proposed HE-FBMG based WPGS is suitable for DC power supply, such as battery charging.

5.2 CONFIGURATION

Fig. 5.2 (a) shows the configuration of the HE-FBMG based WPGS, and the proposed HE-FBMG is directly connected to the wind blade. The armature winding is connected to the load through a three-phase rectifying circuit, and the field winding is connected to a DC power supply. This system has simple structure and no mechanical gearbox is involved, which can improve the efficiency and reliability. With the merit of hybrid excitation, the back EMF and electromagnetic torque can be effectively controlled by the field current, which can simplify the control process.

Meanwhile, thyristor based controlled rectifier in traditional WPGSs can be replaced with diode based uncontrolled rectifier in the proposed HE-FBMG based WPGS, and the cost of hardware can be reduced consequently.

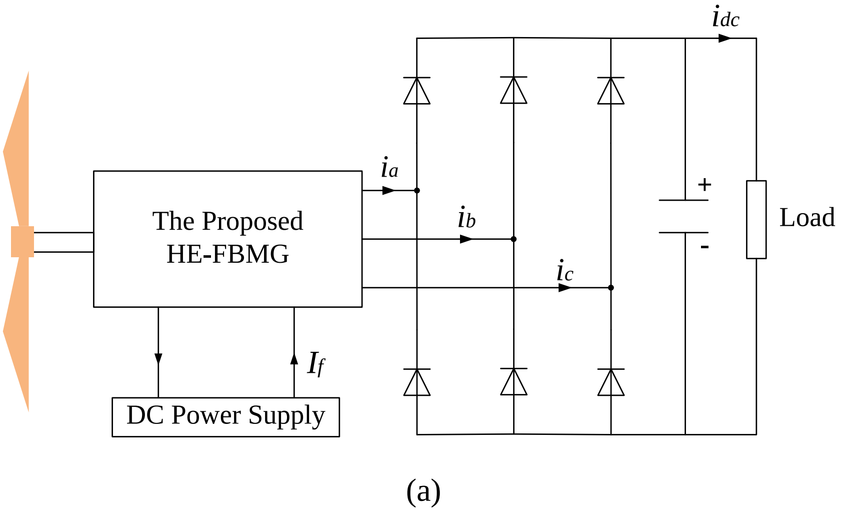

(a)

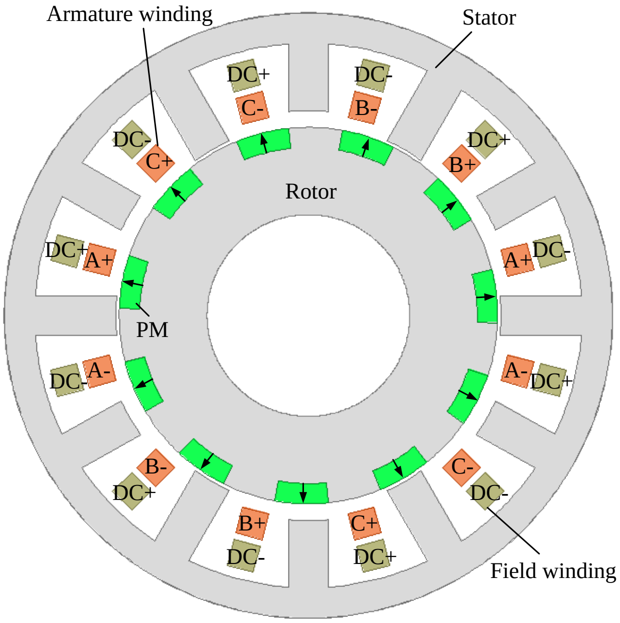

(b)

Figure 5.2 Configuration of the HE-FBMG based WPGS. (a) HE-FBMG based WPGS. (b) Structure of the proposed HE-FBMG.

The structure of the proposed HE-FBMG is shown in Fig. 5.2 (b). Compared with the HEDPM proposed in chapter 4, only stator PMs are removed. Bidirectional flux modulating effect is still incorporated in the design of HE-FBMG.

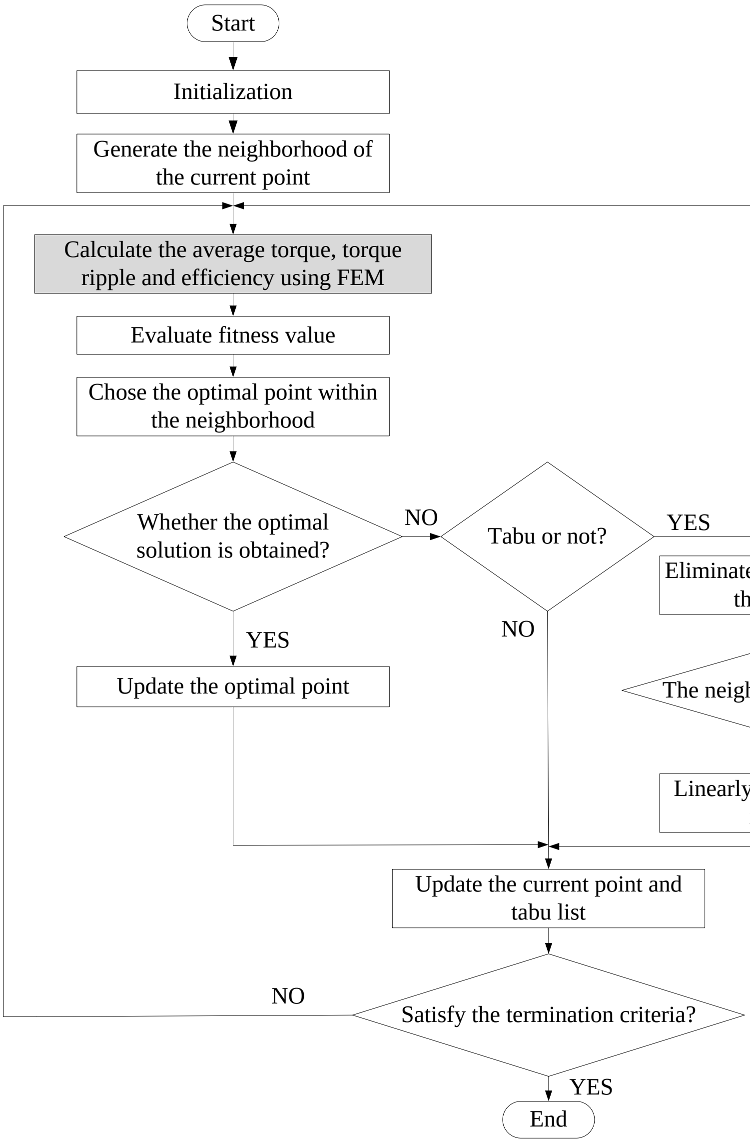

Figure 5.3 Flowchart of the ITS-FEM coupled method.

5.3 DESIGN OPTIMIZATION

5.3.1 ITS-FEM coupled method

An improved Tabu search algorithm coupled with FEM, which is the so-called ITS-FEM coupled method, is used to optimal design the HE-FBMG. The flowchart of ITS-FEM coupled method is shown in Fig. 5.3. Firstly, an initial solution is randomly generated. Starting from a current solution x, a series of neighborhood solutions $x_1, x_2, ..., x_p$ will be generated around x by the algorithm, and the best solution x^* will be chosen from these neighborhood solutions. This best solution x^* is labeled as the new current solution and begins a new cycle of iterations. This optimization process will continue until a stop criterion is satisfied.

In traditional stochastic optimization algorithms, the current solution x changes into the next solution x^* if the value of the objective function is getting better. In this case, the optimization tends to get trapped easily to the local best solution rather than the global best. In this paper, the used ITS algorithm chooses the local best solution instead of the global best solution as the new current one, so as to avoid falling into a local best solution. Moreover, an adaptive step vector is used in the implementation of moves. All the variables are normalized and a standard step vector h with a controlled step-size is set in different directions

$$h_i = h_{i-1} / c_k (c_k = L^{\frac{1}{n-1}}, h_1 = 1), \qquad i = 1, 2, ..., n \tag{5.1}$$

Where L refers to the user-defined step size level, which stipulates a minimal step-size $1/L$ in h. And the update principle is given as

$$x_j^* = x_j + r p_j h_i \tag{5.2}$$

where r is randomly generated within [-1,1], p_j is the coefficient vector p in the j th direction and can be expressed as

$$p_j = \left(b_j - a_j\right)/2, \qquad j = 1, 2, ..., n \tag{5.3}$$

where b_j and a_j refer to the range of p_j. It should be noted that $h_1 = 1$ is always defined to guarantee the global searching ability. The adaptively controlled step size can effectively improve the searching efficiency and accelerate the convergence.

Three objectives are investigated, which include the average output torque f_1, the torque ripple ratio f_2 and the efficiency f_3. The optimal design problem is formulated as

$$\min\{-f_1(x), f_2(x), -f_3(x)\}, \qquad x \in F \tag{5.4}$$

where x refers to the design parameters, F refers to the constraints of the design parameters, and f_2 can be expressed in Eq. (5.5), where $T_{\max}$ and $T_{\min}$ are the maximum value and minimum value of the steady torque, respectively.

$$f_2(x) = \frac{T_{\max} - T_{\min}}{f_1(x)} \tag{5.5}$$

TABLE 5.1 OPTIMIZED VARIABLES

Variables	Lower limit	Upper limit
Inner diameter of stator (mm)	64	55
Rotor PM ratio	80%	30%
Thickness of rotor PM (mm)	5	2
Width of stator teeth (mm)	8	5
Height difference of stator teeth (mm)	5	2

5.3.2 Multi-objective optimization

The parameterized FE model of the proposed HE-FBMG is built using Maxwell package. During optimization, the overall diameter and stack length are fixed at 90 mm and 80 mm, respectively. The variables been optimized and their limits are given in Table 5.1.

The optimization results of the torque ripple ratio and the average output torque are given in Fig. 5.4. One can hardly discover identical relationships between the torque ripple ratio and the average torque. Fig. 5.5 shows the relationship between the efficiency and the average output torque, it can be easily observed that the efficiency is positive correlated with the average output torque. The point with maximum average torque also has the maximum efficiency, and therefore the efficiency and the average output torque can be combined into one single objective during optimization.

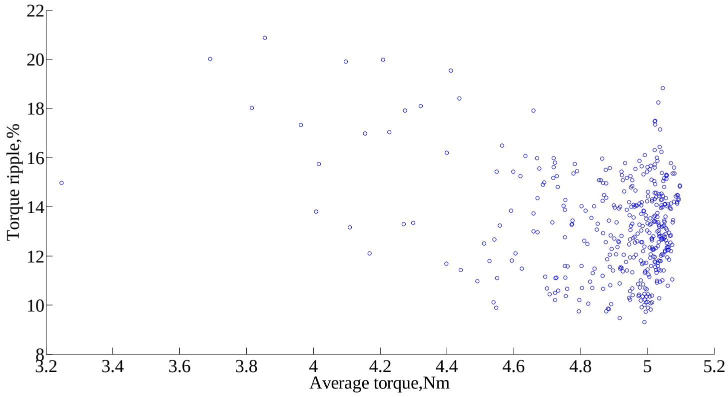

Figure 5.4 The relationship between the torque ripple ratio and average torque.

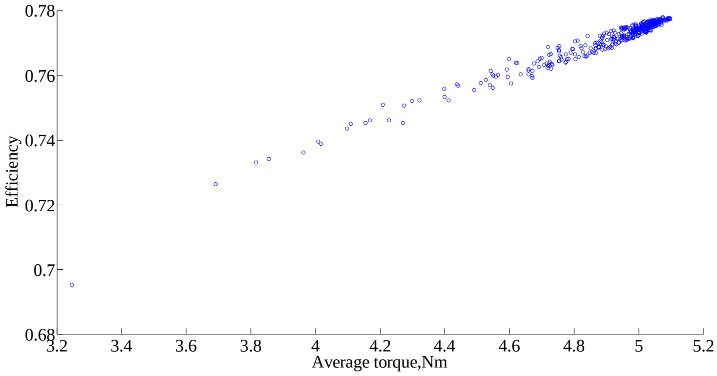

Figure 5.5 The relationship between the efficiency and average torque.

5.3.3 Single-objective optimization

After the aforementioned multi-objective optimization, the proposed HE-FBMG is optimized through single objective optimization, and the objective is to achieve the largest output torque when the excitation current density is fixed at 8 A/mm^2. The constraint during optimization is that the torque ripple ratio should lower than 15%. Fig. 5.6 shows the average output torque and torque ripple ratio at different iterative number. It can be observed that the optimization can converge within 20 iterations and all the torque ripple ratios are lower than 15%, which consists with the constraint and shows the effectiveness of the optimization method. One can find that the proposed machine can achieve good overall performances after optimization. The final design parameters can be obtained and output by the optimization algorithm, which are listed in Table 5.2.

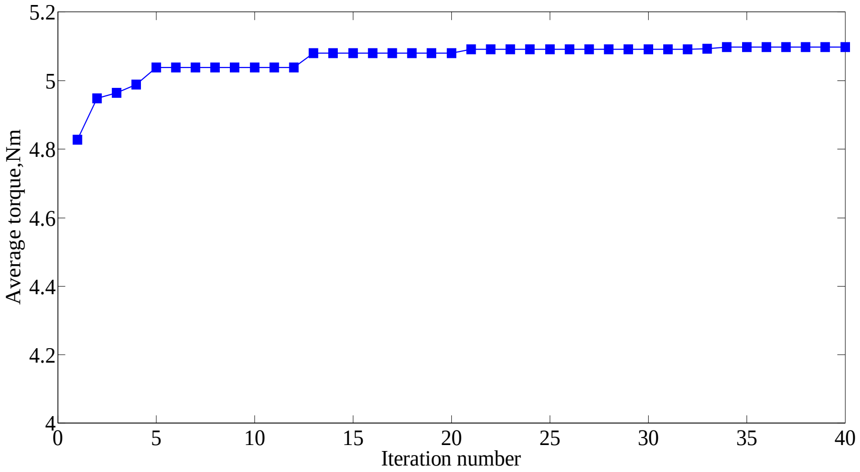

Figure 5.6 Average output torque at different iterative number.

TABLE 5.2 DESIGN PARAMETERS

Parameters	Value
Stator outside diameter(mm)	90
Stator inside diameter(mm)	59.2
Rotor outside diameter(mm)	58.2
Rotor inside diameter(mm)	30
Length of air-gap(mm)	0.5
Stack length(mm)	80
Height difference of stator teeth(mm)	2.5
Width of stator teeth(mm)	5.5
Rotor PM ratio	0.5
Thickness of rotor PMs(mm)	4.1
PPN of armature winding	5
PPN of field winding	6
PPN of rotor PMs	11
Number of stator slots	12
Number of phases	3
Remanence of NdFeB(T)	1.2
Relative permeability of NdFeB	1.05

5.4 CONTROL STRATEGY

In traditional WPGS, the output power of the generator should be rectified by the thyristor based controlled rectifier, which is the hardware basis of the control process. In the proposed HE-FBMG based WPGS, the control process can be achieved by controlling the field current, which is much simpler and thyristor based controlled rectifier in traditional WPGSs can be replaced with diode based uncontrolled rectifier, so the cost of rectifier can be reduced accordingly.

5.4.1 Constant voltage control

Fig. 5.7 shows the control block of constant voltage control, which is suitable for variable speed constant voltage applications. The output power of the armature winding is rectified for DC power charging. The DC charging voltage is a feedback and compared with the reference DC charging voltage in the constant voltage controller. According to the error of reference and feedback DC charging voltage, the constant voltage controller generates the reference field current, which then compared with the feedback field current and control the DC power supply. The reference DC charging voltage is the voltage when the generator runs at a certain speed and no field current is applied, which can be adjusted according to the load requirement. Using this constant voltage control, the DC charging voltage of the proposed HE-FBMG based WPGS can be maintained at a certain level when the wind speed varies.

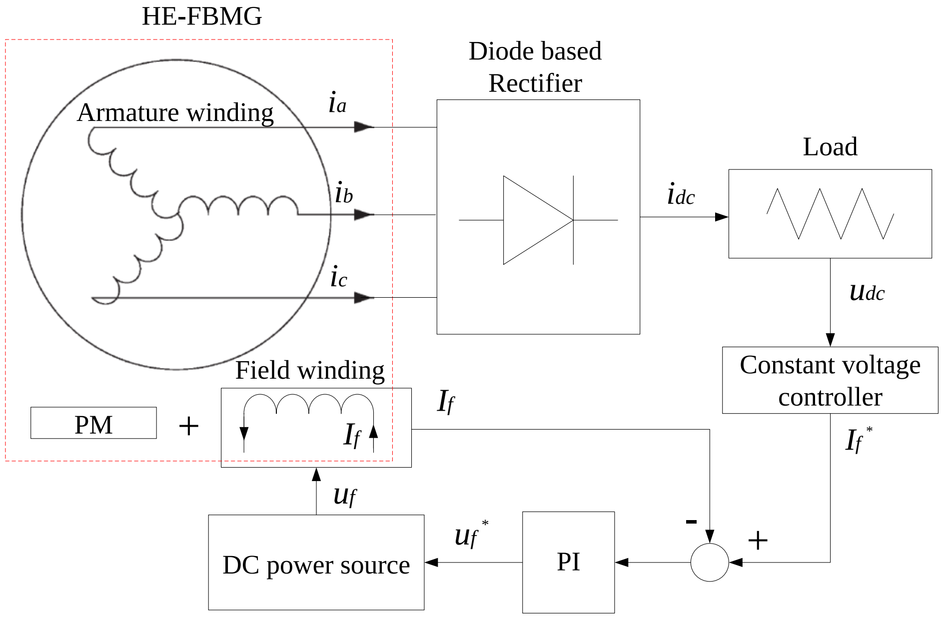

Figure 5.7 Constant voltage control of the proposed HE-FBMG based WPGS.

5.4.2 MPPT control

According to the research reported in [102], the power coefficient of wind power system is a nonlinear function of the wind speed and blade shaft speed. Corresponded to each wind speed, there is an optimal shaft speed which has the largest power coefficient. The MPPT control is to make the generator run at the optimal rotating speeds when the wind speed varies, so the wind blade can capture the maximum wind power. In traditional WPGS, the MPPT control is achieved by controlling the controlled rectifier. In the proposed HE-FBMG based WPGS, the MPPT control can be achieved by controlling the field current. The scheme of MPPT control is given in Fig. 5.8, compared with traditional WPGSs using vector control and thyristor based controlled rectifier, the proposed HE-FBMG based WPGS has simplified control method and hardware.

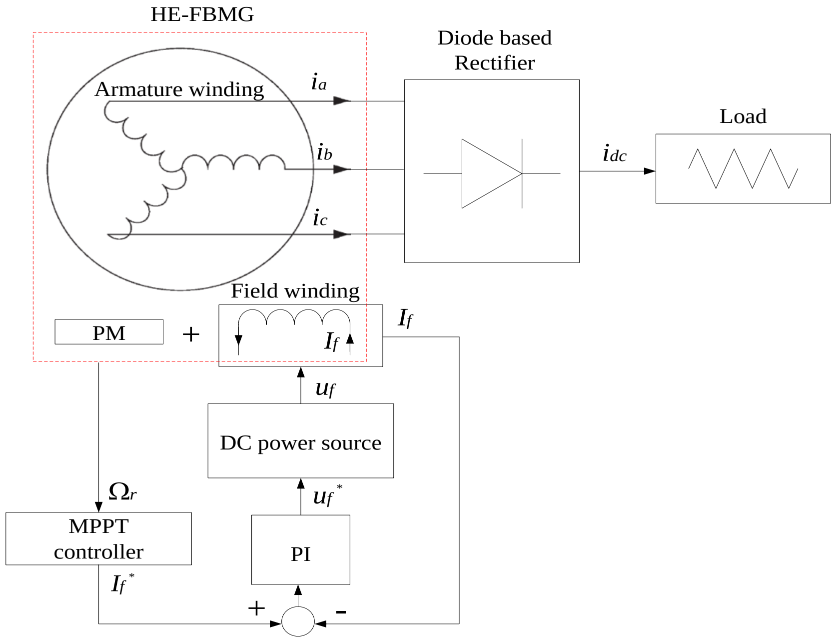

Figure 5.8 MPPT control of the proposed HE-FBMG based WPGS.

5.5 PERFORMANCE ANALYSIS

5.5.1 Air-gap flux density and harmonic spectrum

The air-gap flux density distribution and the harmonic spectrum is given in Fig. 5.9. One can find that the air-gap flux can be effectively regulated by the field current, both flux strengthening and flux weakening can be achieved by inversing the polarity of the field current. When investigating the harmonic spectrum, only low order harmonics with $n=1,2,3$ and $v=1,2,3$ are considered. The harmonics with 11, 22 and 33 PPN are only generated by the rotor PMs and will not be regulated by the field current. The harmonics with 6, 12 and 18 PPN are only generated by the field current, and the amplitude of these harmonics is zero when no field current is applied, as shown in the green bar of Fig. 5.9(b). Other harmonics are generated by both the rotor PMs and the field current, and therefore, these harmonics can be effectively regulated by controlling the field current.

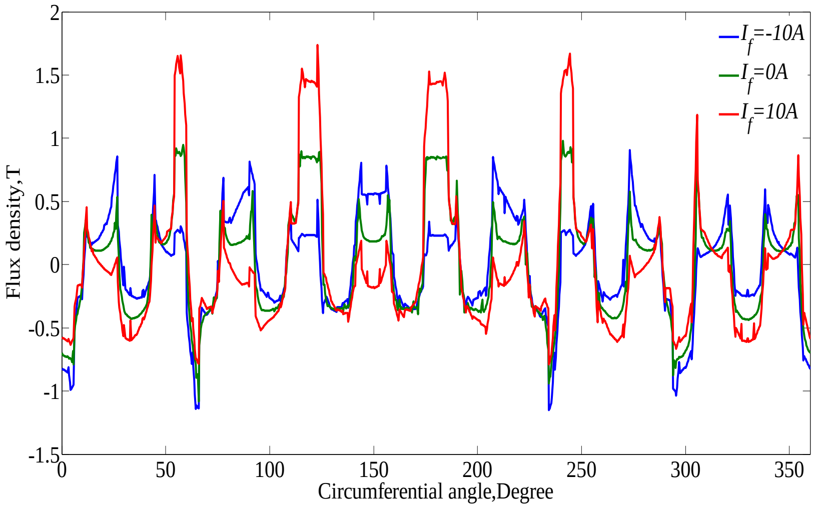

(a)

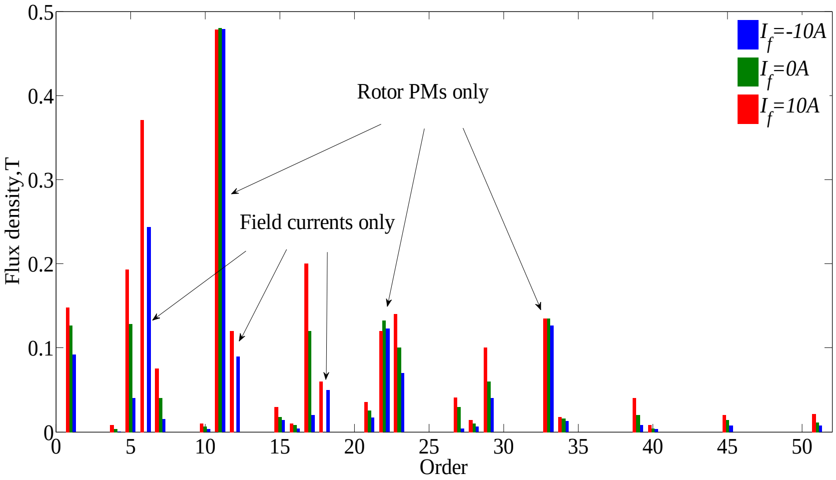

(b)

Figure 5.9 Open-circuit air-gap flux density distributions and harmonics. (a) Flux density distributions. (b) Harmonics.

5.5.2 Flux linkage and back EMF

Fig. 5.10 shows the open-circuit flux linkage waveforms of with/without field current. One can find that the flux linkage can be effectively regulated through the field current, and by inversing the polarity of the field current, both flux strengthening and flux weakening can be achieved. Similar phenomenon can be observed in the back EMF waveforms shown in Fig. 5.11. Therefore, by controlling the field current, the proposed HE-FBMG can achieve constant output voltage when runs at different speeds.

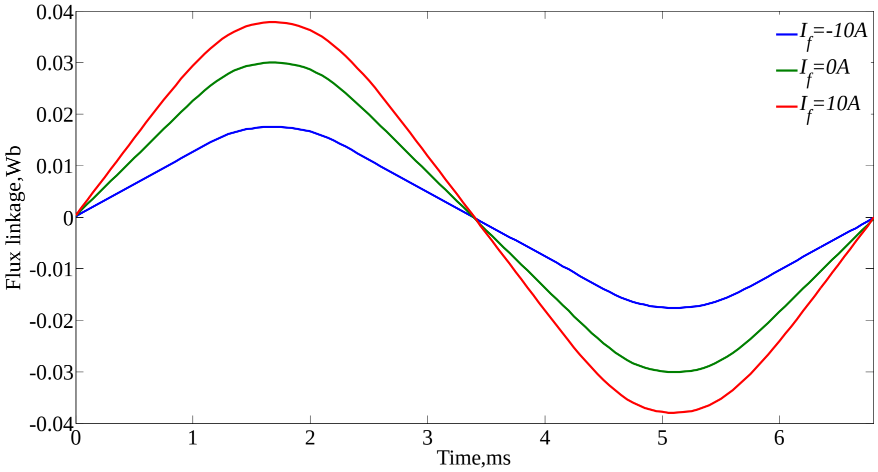

Figure 5.10 Open-circuit flux linkage waveforms.

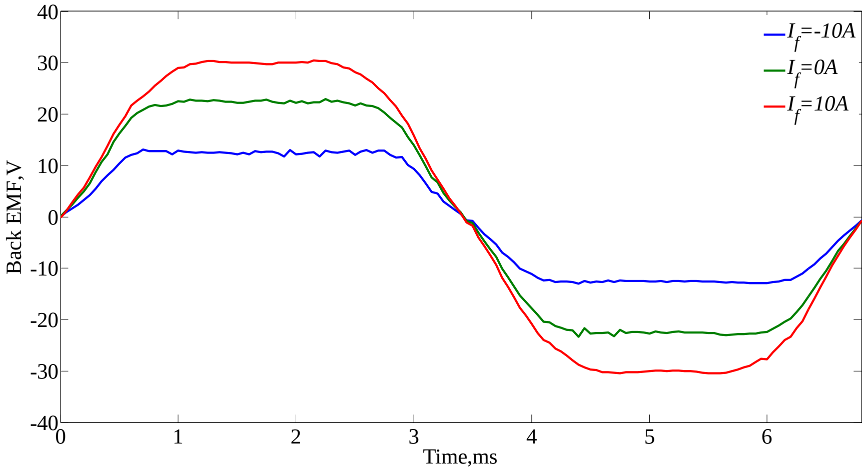

Figure 5.11 No load back EMF waveforms.

5.5.3 Torque characteristics

Fig. 5.12 shows the stationary torque waveforms, in which the armature current density is 8A/mm^2 and the rotor is locked. It can be seen that the output torque can be regulated by the field current as well, when applied with field strengthening current, the output torque of the proposed HE-FBMG can be improved. Fig. 5.13 shows the torque-current waveforms, no field current is applied in this case and the armature current density varies from 2A/mm^2 to 20A/mm^2. One can find that the output torque of the proposed HE-FBMG is greatly influenced by the current density. When the cooling condition is improved and large current density can be applied, the torque capability of the proposed generator can be increased.

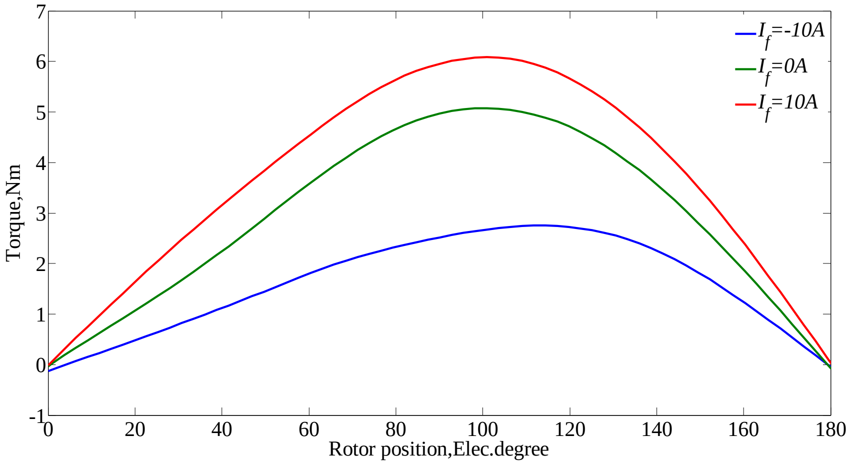

Figure 5.12 Stationary torque waveforms.

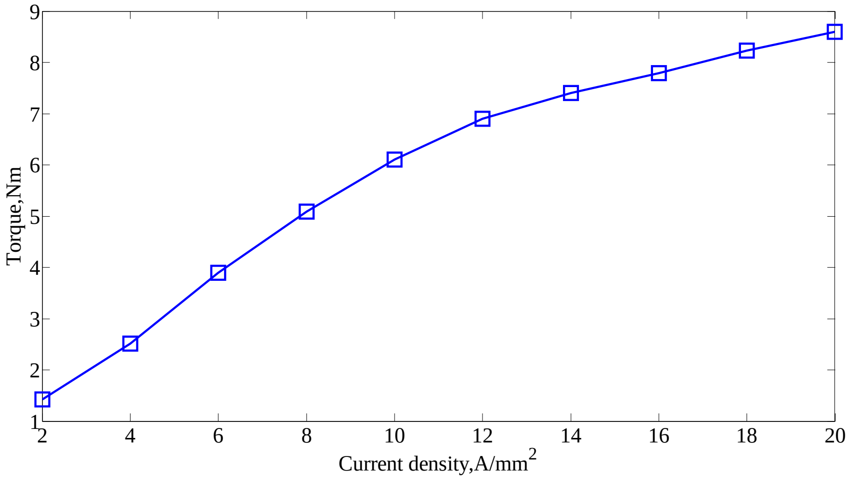

Figure 5.13 Torque-current waveforms.

5.6 EXPERIMENTAL VERIFICATION

5.6.1 Test bench

In order to verify the proposed HE-FBMG based WPGS, a prototype of the

HE-FBMG is made and the test bench is shown in Fig. 5.14. The design parameters of the prototype are exactly the same as the parameters given in Table 5.1. It should be noted that this prototype is only used to validate the proposed design, it cannot be used in a real WPGS because it is a scale-down prototype and its rotor PPN is small. The proposed machine concept can be used in real WPGS when designed with large size and large rotor PPN. The generator is driven by a servo motor, which is controlled by a Siemens 1212C PLC controller stored with the wind turbine parameters and wind curves, and the load is provided by a slide rheostat.

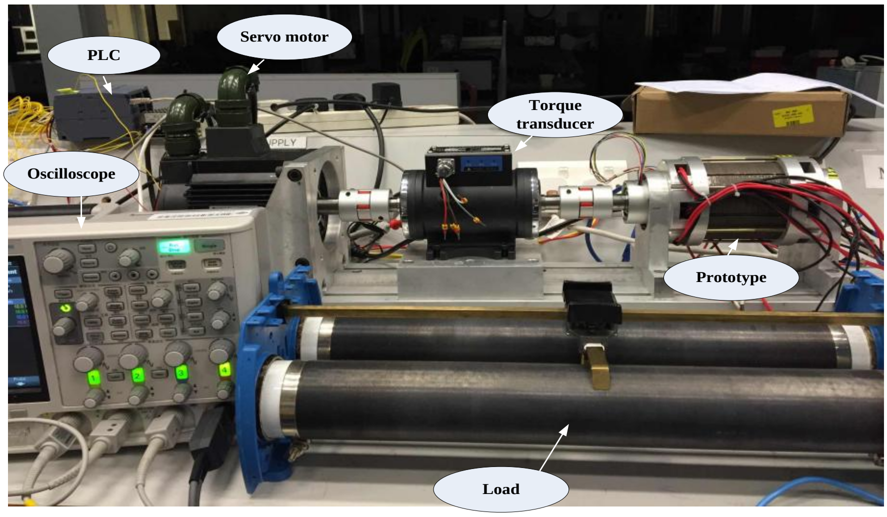

Figure 5.14 Test bench of the proposed HE-FBMG based WPGS.

5.6.2 EMF measurement

The back EMF waveforms when the proposed machine running at 800rpm and applied with different field currents are tested and given in Fig. 5.15. It can be observed that the back EMF can be effectively regulated by the field current. The EMF waveforms are not purely sinusoidal and balanced due to the unsymmetrical flux density distribution. There may also exist slight mechanical errors during manufacturing and assembling. Fig. 5.16 shows the comparison of EMF waveforms when the proposed generator is applied with positive field current, no field current and negative field current. One can find good agreement between the test results and the simulation results.

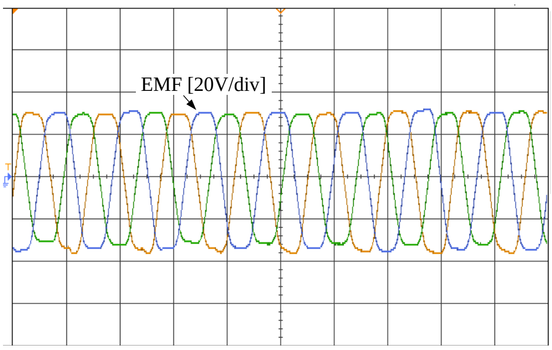

(a)

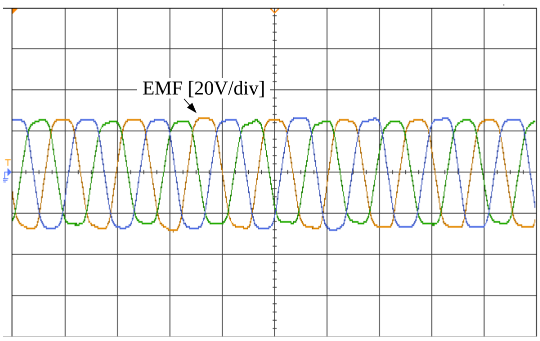

(b)

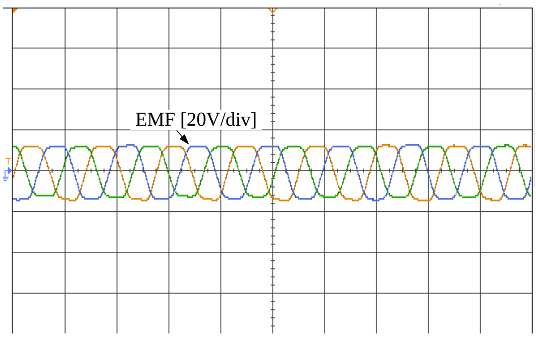

(c)

Figure 5.15 Measured EMF waveforms when applied with different field currents. (a) $I_f = 10A$. (b) $I_f = 5A$. (c) $I_f = -10A$.

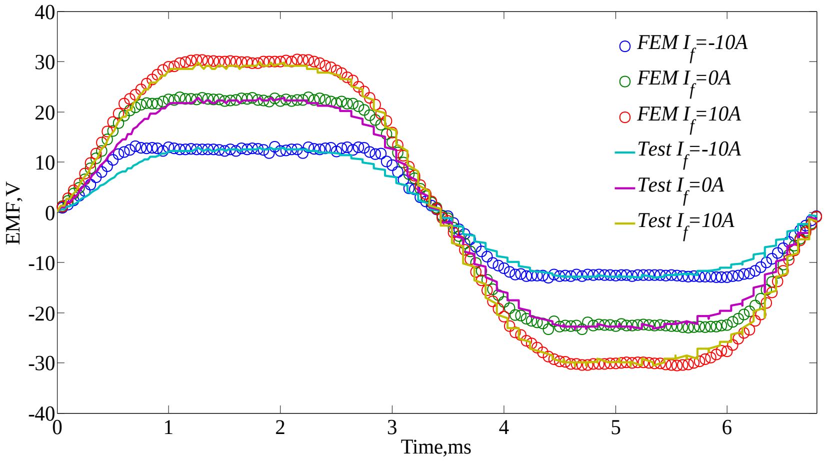

Figure 5.16 Comparison of EMF waveforms.

5.6.3 Performances without field current

The steady state performances when no field current is applied are studied. Fig. 5.17 shows the generator torque and phase current when the generator runs at 800rpm and the load resistance is 20Ω. It is shown that the proposed generator can work stably and sinusoidal phase current can be obtained. Keeping the rotating speed unchanged, the generator torque at different load resistances are tested and given in Fig. 5.18. One can find that with the increasing of load resistance, the generator torque reduces because the increasing of load resistance reduces phase current. Changing the load resistance to 35Ω, the steady state generator torque, rotating speed, output DC voltage and output DC current are all shown on the oscilloscope, as given in Fig. 5.19. Again, we can find that the proposed HE-FBMG based WPGS can generate smooth DC voltage and DC current, therefore is very suitable for DC power supply.

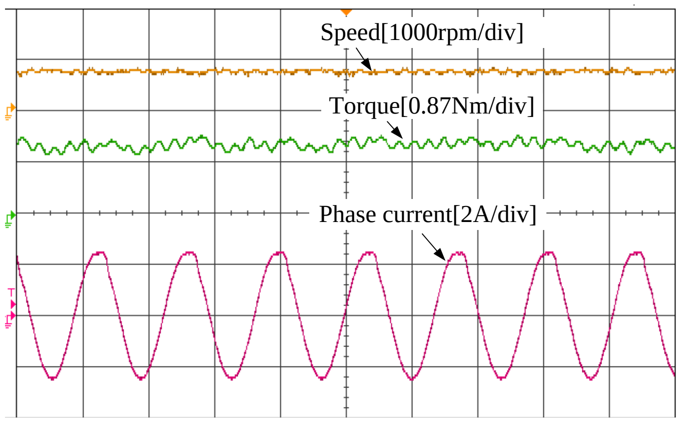

Figure 5.17 Torque, speed and phase current when the load resistance is 20Ω.

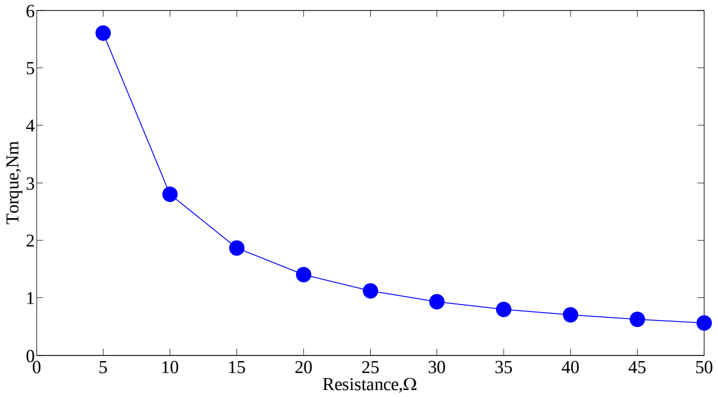

Figure 5.18 Generator torque at different load resistances.

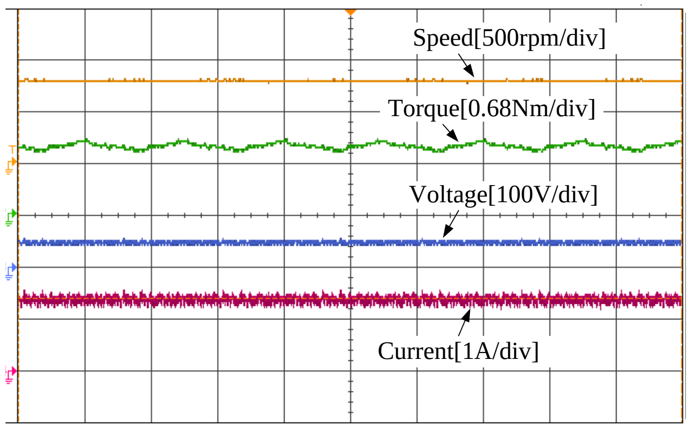

Figure 5.19 Torque, speed, DC voltage and DC current when load resistance is 35Ω.

5.6.4 DC charging voltage and power

The DC charging voltage, and output DC power are given in Fig. 5.20, when the proposed generator runs at different speeds and load resistance is 35Ω. Three operations are investigated, which include field winding open-circuited, constant voltage control and MPPT control. One can find that when no field current is applied, the DC charging voltage increases almost linearly with the increasing of the rotor speed. When using constant voltage control, the proposed HE-FBMG can maintain the DC charging voltage at a certain level, hence very suitable for variable speed constant voltage applications. When using MPPT control, the proposed HE-FBMG based WPGS can get the optimal power point and the output power can be improved effectively. The experimental results well validate the proposed design.

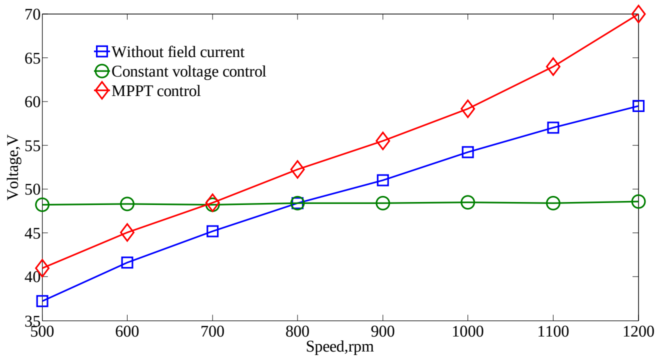

(a)

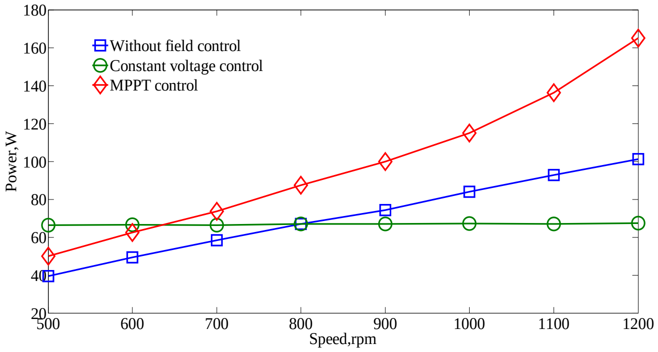

(b)

Figure 5.20 DC charging voltage and output DC power when the generator speed varies. (a) DC charging voltage. (b) Output DC power.

5.7 SUMMARY

In this chapter, a novel hybrid excited generator with flux bidirectional modulating effect is proposed for WPGS. With the proposed generator, thyristor based controlled rectifier in traditional WPGSs can be replaced with diode based uncontrolled rectifier, which can reduce the hardware cost. Bidirectional flux modulating effect is incorporated into the proposed design, which guarantees effective magnetic coupling among the magnetic fields excited by the PMs, field coils and armature windings. Both constant voltage control and MPPT control can be achieved by controlling the field current, the control process is simplified. The analytical model of the proposed generator is established, which can give an insight into the working principle and flux regulating theory. The control strategies are discussed, and an ITS algorithm is used to optimal design the proposed generator. The electromagnetic performances are preliminary investigated using FEM and verified through experiment tests, which are summarized in Table 5.3.

TABLE 5.3 ELECTROMAGNETIC PERFORMANCES

Items	Values
Rated speed	800rpm
Rated torque	5.1Nm
Maximum torque	8.6Nm
Rated power	427W
Maximum power	720W

CHAPTER 6 DC-COIL-FREE HYBRID-EXCITED MACHINES

6.1 INTRODUCTION

Although HEMs are theoretically good candidates to achieve better overall performances, they suffer from a common drawback, which is low slot utilization rate caused by the additional field windings. The field windings inevitably occupy some slot space and the effective slot area for armature windings is reduced which accordingly reduces the torque density below the base speed. The same goes for the flux regulating capability, which is also restricted by the available slot space for the field coils.

In this chapter, a novel hybrid excited machine concept is proposed, which is referred as DC-coil-free hybrid excited machine (DCF-HEM). DC coils are eliminated and field excitation is achieved through injecting DC bias currents into the armature windings. Each phase of armature windings is divided into two sub-phases, which are injected with opposite DC-bias currents. Therefore, the proposed machine has dual electrical ports and the zero sequence current flows between the two ports can act as the air-gap field regulator. The proposed DCF-HEM can be designed with stator PM, rotor PM and dual PMs, all of them are optimized and investigated using finite element method (FEM) in this paper. A dual PM DCF-HEM prototype is made, and its electromagnetic performances are verified through experimental investigations.

6.2 MACHINE CONFIGURATION

DCF-HEM can be designed with various configurations. As long as concentrated armature windings are employed and the rotor has flux modulating effect with proper number of salient poles, the field winding can be eliminated through injecting DC bias current into the armature windings. In this chapter, three machine configurations are investigated, which is developed from the HEMs discussed in chapter 4 and chapter 5. The machine configurations are shown in Fig. 6.1, namely DPM with dual PM excitation, RPM with rotor PM excitation only and SPM with stator PM excitation only. Each phase of the armature coils is divided into two sub-phases, which are excited by the same armature current but opposite DC bias current, as given in Eq. (6.1).

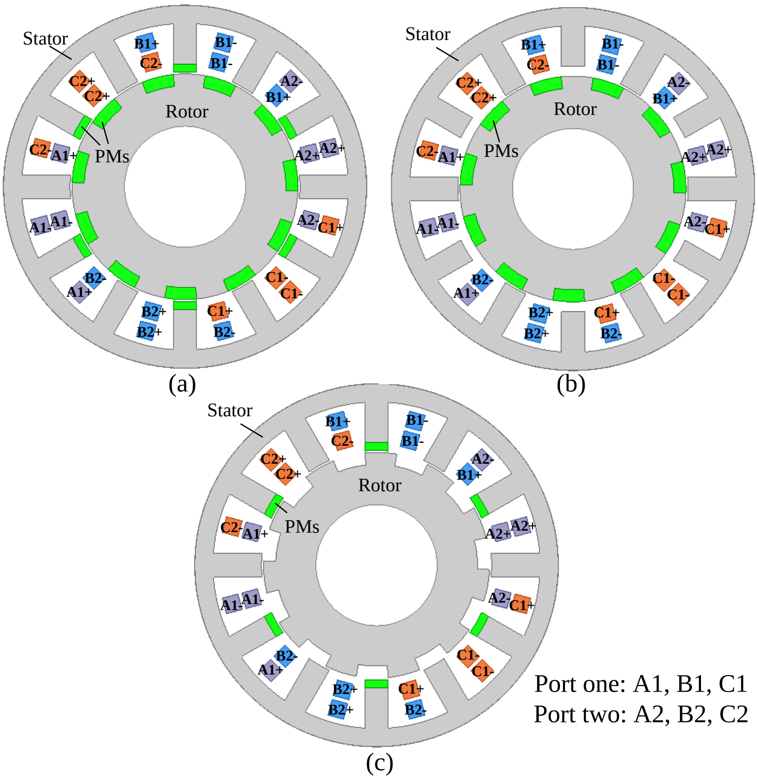

(a) (b) (c)

Figure 6.1 Configurations of the proposed DCF-HEMs. (a) DPM. (b) RPM. (c) SPM.

$$\begin{cases} i_{A1} = \sqrt{2} I_{ac} \cos\left(\omega_e t\right) + I_{dc} \\ i_{B1} = \sqrt{2} I_{ac} \cos\left(\omega_e t - 2\pi/3\right) + I_{dc} \\ i_{C1} = \sqrt{2} I_{ac} \cos\left(\omega_e t - 4\pi/3\right) + I_{dc} \\ i_{A2} = \sqrt{2} I_{ac} \cos\left(\omega_e t\right) - I_{dc} \\ i_{B2} = \sqrt{2} I_{ac} \cos\left(\omega_e t - 2\pi/3\right) - I_{dc} \\ i_{C2} = \sqrt{2} I_{ac} \cos\left(\omega_e t - 4\pi/3\right) - I_{dc} \end{cases} \tag{6.1}$$

where $i_{A1,\,B1,\,C1}$ and $i_{A2,\,B2,\,C2}$ are the currents of the port I and port II, respectively. I_{ac} and I_{dc} are the RMS value of armature current and DC bias current, respectively. ω_e refers to the angular velocity of armature current. An equivalent current I_e is defined and expressed in Eq. (6.2).When DC bias current is applied, the RMS value of armature current is reduced to keep the equivalent current I_e unchanged so as to keep the copper loss unchanged.

$$I_e = \sqrt{\frac{1}{T}\int_0^T \left[\sqrt{2} I_{ac} \cos\left(\omega_e t\right) + I_{dc}\right]^2 dt} = \sqrt{I_{ac}^2 + I_{dc}^2} \tag{6.2}$$

6.3 CONTROL STRATEGY

The overall control block diagram is shown in Fig. 6.2. The d-axis reference current is set to zero during the control process. The AC component is totally transformed to q-axis current to produce electromagnetic torque, while the DC bias current is transformed to zero sequence current to regulate flux. The Clarke transformer and Park transformer for the proposed machine can be expressed as

$$\begin{bmatrix} i_{\alpha 1} \\ i_{\beta 1} \\ i_{\alpha\beta 01} \\ i_{\alpha 2} \\ i_{\beta 2} \\ i_{\alpha\beta 02} \end{bmatrix} = \sqrt{\frac{2}{3}} \begin{bmatrix} 1 & -\frac{1}{2} & -\frac{1}{2} & 0 & 0 & 0 \\ 0 & \frac{\sqrt{3}}{2} & -\frac{\sqrt{3}}{2} & 0 & 0 & 0 \\ \frac{1}{\sqrt{2}} & \frac{1}{\sqrt{2}} & \frac{1}{\sqrt{2}} & 0 & 0 & 0 \\ 0 & 0 & 0 & 1 & -\frac{1}{2} & -\frac{1}{2} \\ 0 & 0 & 0 & 0 & \frac{\sqrt{3}}{2} & -\frac{\sqrt{3}}{2} \\ 0 & 0 & 0 & \frac{1}{\sqrt{2}} & \frac{1}{\sqrt{2}} & \frac{1}{\sqrt{2}} \end{bmatrix} \begin{bmatrix} i_{\mathrm{A1}} \\ i_{\mathrm{B1}} \\ i_{\mathrm{C1}} \\ i_{\mathrm{A2}} \\ i_{\mathrm{B2}} \\ i_{\mathrm{C2}} \end{bmatrix} \tag{6.3}$$

$$\begin{bmatrix} i_{d1} \\ i_{q1} \\ i_{01} \\ i_{d2} \\ i_{q2} \\ i_{02} \end{bmatrix} = \begin{bmatrix} \cos\theta & -\sin\theta & 0 & 0 & 0 & 0 \\ \sin\theta & \cos\theta & 0 & 0 & 0 & 0 \\ 0 & 0 & 1 & 0 & 0 & 0 \\ 0 & 0 & 0 & \cos\theta & -\sin\theta & 0 \\ 0 & 0 & 0 & \sin\theta & \cos\theta & 0 \\ 0 & 0 & 0 & 0 & 0 & 1 \end{bmatrix} \begin{bmatrix} i_{\alpha 1} \\ i_{\beta 1} \\ i_{\alpha\beta 01} \\ i_{\alpha 2} \\ i_{\beta 2} \\ i_{\alpha\beta 02} \end{bmatrix} \tag{6.4}$$

By substituting Eq. (6.1) into Eq. (6.3), the zero-sequence current i_0 can be obtained, as followed.

$$\begin{cases} i_{01} = \sqrt{3} I_{dc} \\ i_{02} = -\sqrt{3} I_{dc} \end{cases} \tag{6.5}$$

From Eq. (6.5), the zero-sequence current i_0 is proportional to the DC bias current I_{dc}, so the control of I_{dc} can be realized by controlling i_0, as shown in Fig. 6.2. PI controllers are used to regulate the dq0-axis currents to reach their reference values. Detailed design method of PI controllers including how to select the gains are reported in [103].

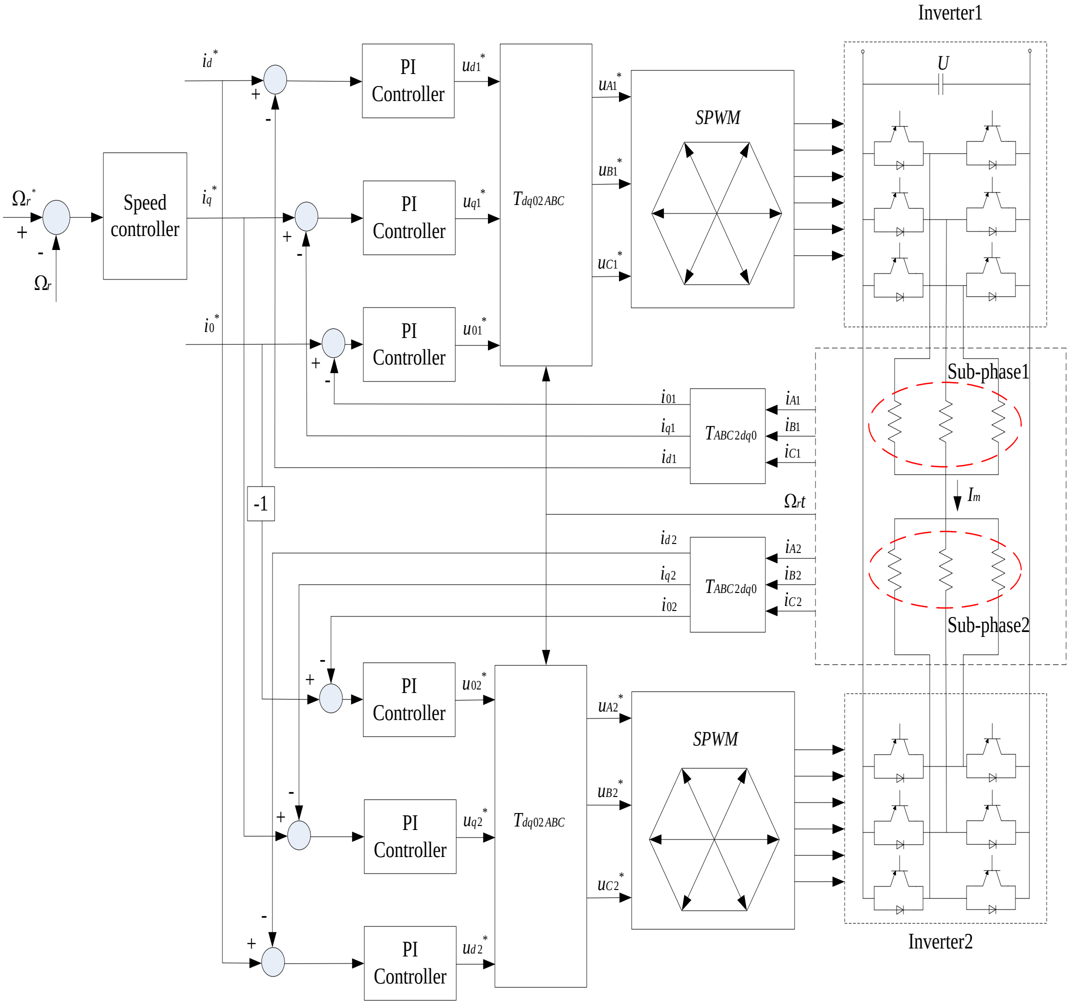

Figure 6.2 Control block diagram of the proposed machine.

6.3.1 Generating the DC bias current

The key feature of the proposed machine is the utilization of DC bias current to achieve air-gap field regulation. The stator winding is divided into two sub-phases. Sub-phase 1 is supplied by sinusoidal AC current with positive DC bias, while sub-phase 2 is supplied by sinusoidal current with negative DC bias. For traditional star-connected three-phase winding, the sinusoidal current is produced by pulse width modulation (PWM) scheme, as shown in Fig. 6.3 (a). Since the used inverter is voltage fed, a DC bias voltage is generated first to produce a DC bias current. The PI controller responsible to minimize the error $i_0^* - i_{01}$, and generate DC voltages which are added to reference voltage vector used for SPWM.

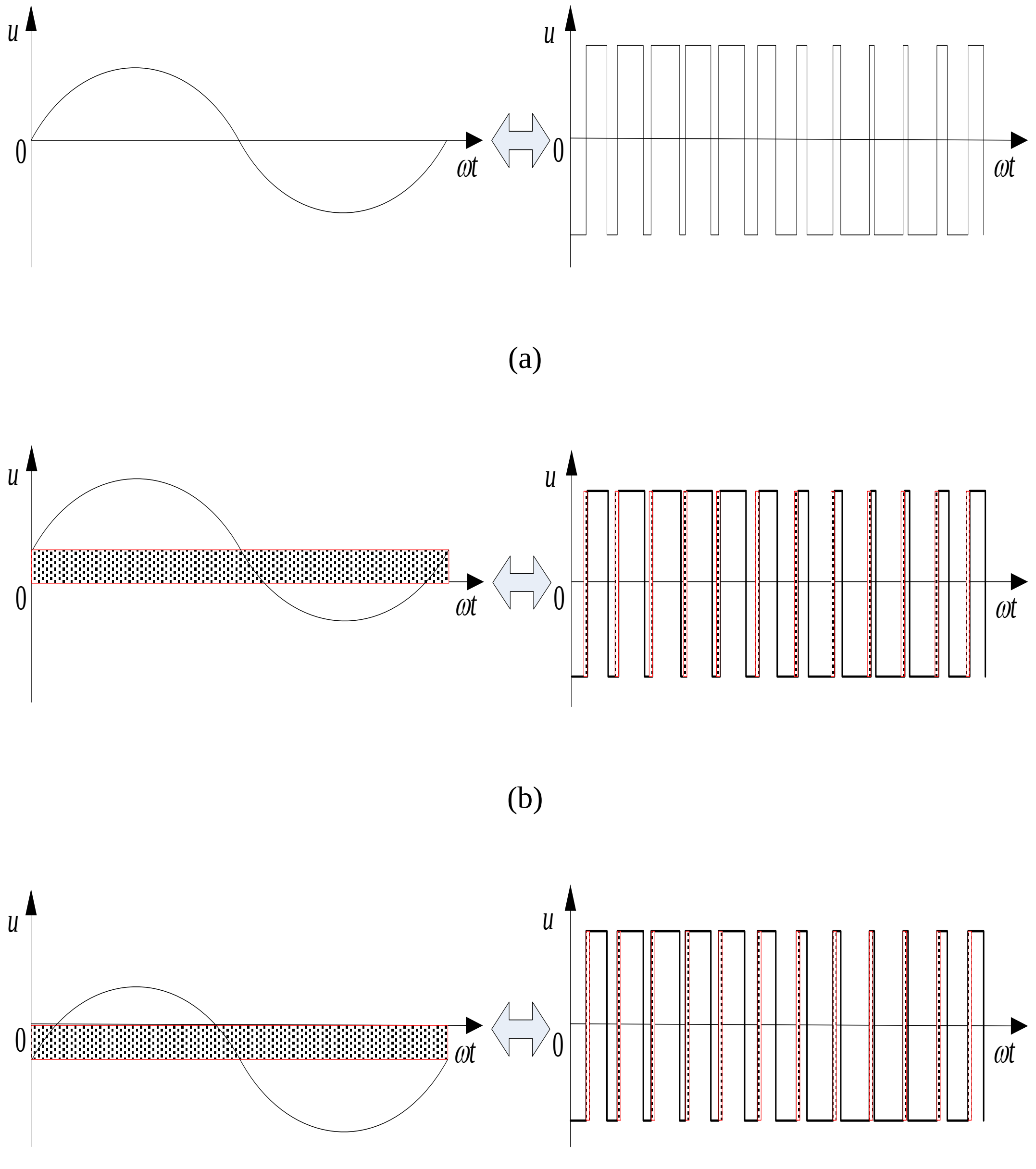

(a)

(b)

(c)

Figure 6.3 PWM scheme with/without DC bias. (a) Conventional sinusoidal wave. (b) Sinusoidal wave with positive DC bias. (c) Sinusoidal wave with negative DC bias.

To generate sinusoidal current with positive DC bias, the turn-on period is extended with the same value for all the pulses, as shown in Fig. 6.3 (b), while, to create sinusoidal current with negative DC bias, the turn-on period for all the pulses are shortened with the same value, as shown in Fig. 6.3 (c). The area of the shadow parts in the left figures and the corresponding right figures are equal based on the area equivalence principle.

6.3.2 Flux weakening operation

For traditional HEMs, the armature windings and field windings are separately controlled. The armature current is used as q-axis current to produce electromagnetic torque, while the flux weakening is achieved by applying DC current to the field windings. The maximum flux weakening current can be expressed as

$$I_{HEM} = A_{slot} K_{slot} J \frac{N_{dc}}{N_{dc} + N_{ac}} \tag{6.6}$$

in which, J is the current density, A_{slot} and K_{slot} are the slot area and slot filling factor, respectively, while N_{ac} and N_{dc} represent the turns of armature winding and field winding, respectively. However, for the proposed machine, the maximum flux weakening current can be increased as the armature winding and field winding are integrated into one set of winding. Theoretically, the maximum flux weakening current is given in Eq. (6.7) with AC component equal to zero, which means all the current are used as zero sequence current to regulate the flux.

$$I_{pro} = A_{slot} K_{slot} J \tag{6.7}$$

The voltage equation in dq0 frame can be expressed as

$$\begin{bmatrix} u_d \\ u_q \\ u_0 \end{bmatrix} = R_s \begin{bmatrix} i_d \\ i_q \\ i_0 \end{bmatrix} + \begin{bmatrix} L_d & 0 & 0 \\ 0 & L_q & 0 \\ 0 & 0 & L_0 \end{bmatrix} p \begin{bmatrix} i_d \\ i_q \\ i_0 \end{bmatrix} + \Omega_r \begin{bmatrix} 0 & -L_q & 0 \\ L_d & 0 & 0 \\ 0 & 0 & 0 \end{bmatrix} \begin{bmatrix} i_d \\ i_q \\ i_0 \end{bmatrix} + \Omega_r \psi_f \begin{bmatrix} 0 \\ 1 \\ 0 \end{bmatrix} \quad (6.8)$$

where p is differential operator, R_s is the resistance of each phase, ψ_f is the excitation flux, $u_{d,q,0}$, $i_{d,q,0}$ and $L_{d,q,0}$ are the voltage, current and self-inductance in dq0 axis, respectively. If flux weakening is required, it can be achieved by adjusting the zero sequence current after i_d is set to zero. During steady condition, the differential of current is zero and the voltage equation can be rewritten as

$$\begin{aligned} u_d &= 0 \\ u_q &= R_s i_q + \omega \psi_f \\ u_0 &= R_s i_0 \end{aligned} \quad (6.9)$$

Therefore the voltage from the inverter can be expressed as

$$u = \sqrt{u_q^2 + u_0^2} = \sqrt{\left(R_s i_q + \Omega_r \psi_f\right)^2 + \left(R_s i_0\right)^2} \quad (6.10)$$

One can find that the zero sequence current only involves a small voltage drop since the resistance R_s is usually very small. The i_q^* is obtained from the speed controller, which is exactly the same as the control in traditional permanent magnet synchronous machines, and i_0^* is obtained through

$$i_0^* = \frac{\sqrt{u_{\lim}^2 - \left(R_s i_q^* + \Omega_r \psi_f\right)^2}}{R_s} \quad (6.11)$$

where $u_{\lim}$ is the voltage limit of inverter.

6.3.3 Constant torque operation

When the proposed machine runs below the base speed and no flux regulation is required, the zero sequence current is set to zero. It means there is no DC bias in the excitation currents, and all the AC current is transformed into the q-axis current. For traditional HEMs, since the field winding is not excited and useless during constant torque operation, the maximum output torque can be expressed as

$$T_{HEM} = p\psi_f A_{slot} K_{slot} J \frac{N_{ac}}{N_{dc} + N_{ac}} \tag{6.12}$$

in which p is the pole-pair number, ψ_f is the flux linkage produced by the PMs. For this proposed machine, since all the windings are excited as q-axis current to produce electromagnetic torque, the maximum output torque is improved, which can be expressed as

$$T_{pro} = p\psi_f A_{slot} K_{slot} J \tag{6.13}$$

6.4 DESIGN CONSIDERATIONS

The design process of electrical machine is usually a compromise among a lot of conflicting requirements. As there are many factors need to be considered, it’s difficult to find a unique solution. In this paper, torque is the major consideration during the design process because torque improvement is a major advantage of the proposed DCF-HEMs over traditional HEMs with additional field coils.

Fig. 6.4 shows the flow chart of the design process. Firstly, the overall dimensions are obtained based on the well-known torque equation. Then parametric models of stator and rotor are established using Maxwell Package. The materials used for lamination and magnet are chosen according to their electromagnetic characteristics. Finally, the windings are designed and connected. With these four steps, an initial model is obtained. Since some key design parameters have significant influence on output torque, these parameters are swept and optimal values are obtained based on their torque performance.

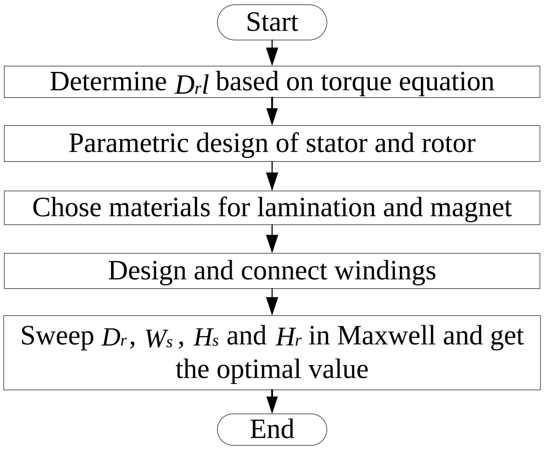

Figure 6.4 Flow chart of the design process.

For conventional PM machines, the electromagnetic torque T_e is positively proportional to the rotor volume, as governed by Eq. (6.14).

$$T_e \propto D_r^2 l \tag{6.14}$$

where D_r and l are the rotor diameter and axial length, respectively. The size of stator PMs and rotor PMs also have great impact on the electromagnetic torque. According to the existing research reported in[69], good flux modulating effect can be achieved when the ratio of modulating segment is 0.5. Therefore the ratio of rotor-pole width to rotor-PM width is fifty to fifty in this paper, and only thickness of rotor pole is investigated. The analyzed variables are listed as follows:

1) D_r, Rotor diameter;

2) W_s, Width of stator tooth;

3) H_s, Thickness difference of stator tooth;

4) H_r, Thickness of rotor pole.

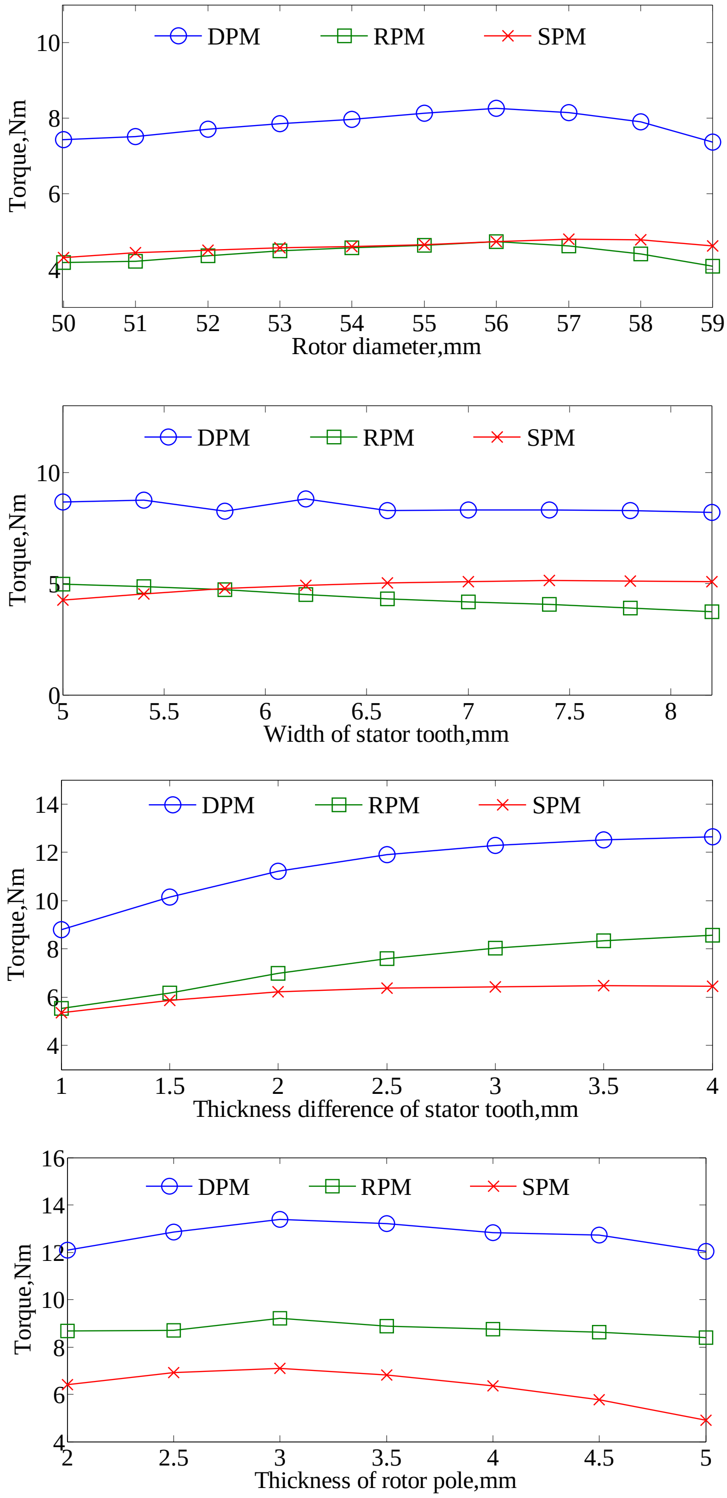

Figure 6.5 Effect of geometric parameters on torque.

Fig. 6.5 shows the effect of geometric parameters on torque, in which no DC bias current is applied and the armature current density is fixed at 8A/mm^2. It can be observed that both the stator PM and rotor PM can interact with armature field to produce electromagnetic torque, and machine one has larger torque capability due to its dual PM excitation. It should be noted that the purpose of this paper is to propose HEMs with integrated AC and DC windings, and systematical design optimization is not conducted in this paper. The final design parameters of these three machines are listed in Table 6.1.

TABLE 6.1 DESIGN PARAMETERS

Items	DPM	RPM	SPM
Stator outer diameter	90mm		
Rotor outer diameter	56mm	56mm	58mm
Length of air-gap	0.5mm		
Stack length	80mm		
Width of stator tooth	6.2mm	5mm	5.8mm
Thickness difference of stator tooth	3mm	3.5mm	2mm
Thickness of rotor pole	3mm		
Ratio of rotor pole	0.5		
PPN of stator	6		
PPN of rotor	11		
PPN of armature current	5		
Number of stator slots	12		
Number of phases	3		
Turns of conductors	70		
PM material	NdFeB		
Magnet Remanence	1.1T		

6.5 FINITE ELEMENT ANALYSIS

6.5.1 Flux linkage

The electromagnetic performances of the proposed DCF-HEMs are investigated using finite element method (FEM). Maxwell package is used to establish the models and conduct FE calculation. Fig. 6.6 shows the flux linkage waveforms when the DCF-HEMs run at 800rpm and are applied with/without DC bias current. It can be observed that flux linkage in sub-phase one and sub-phase two are synchronous but with opposite DC bias components. When no DC bias current is applied, sub-phase one has negative DC biased flux linkage while sub-phase two has positive DC biased flux linkage. After injecting positive DC bias current into the windings, the peak-peak value of flux linkage is reduced, which means flux weakening is achieved. The peak-peak value of flux linkage when applied with different DC bias current is given in Fig. 6.7. One can find that the flux linkage variation decreases almost linearly with the increasing of DC bias current.

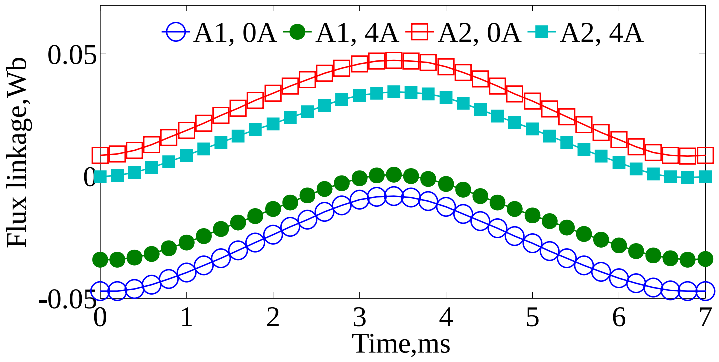

(a)

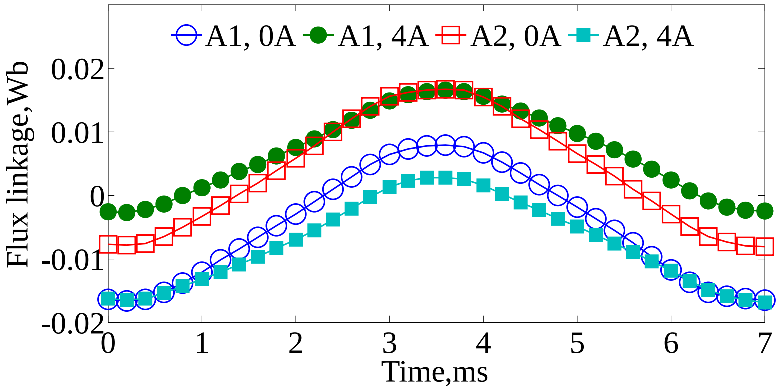

(b)

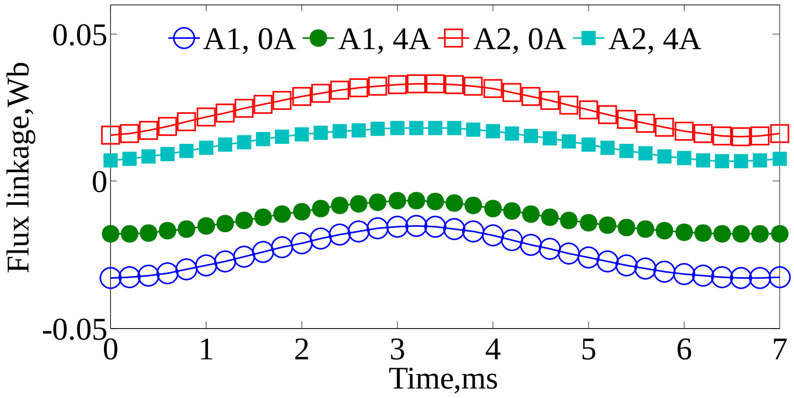

(c)

Figure 6.6 Flux linkage waveforms. (a) DPM. (b) RPM. (c) SPM.

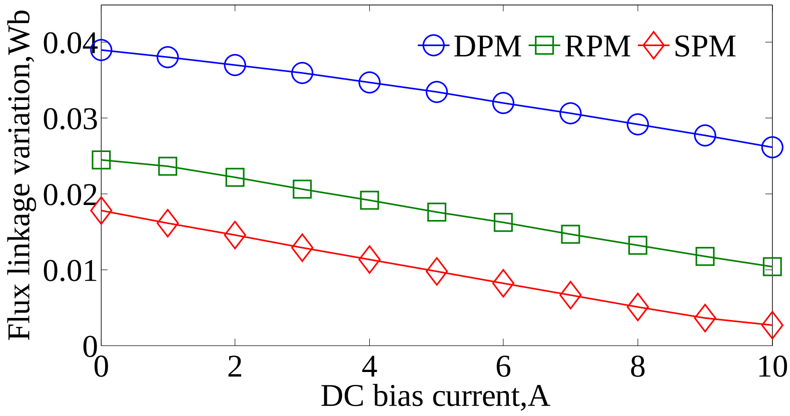

Figure 6.7 Flux linkage variation.

6.5.2 Back EMF

Fig. 6.8 shows the back EMF of DCF-HEMs when applied with/without DC bias current. It can be clearly observed that the back EMF can be weakened effectively by injecting DC bias currents. Among all the three machines, SPM has the best flux weakening capability since the stator PMs and DC bias current share the same magnetic path, therefore stator PM excitation can be directly regulated by the DC bias current. Although rotor PMs are rotating, the rotor PM field can also be regulated by DC bias current due to bi-directional flux modulating effect.

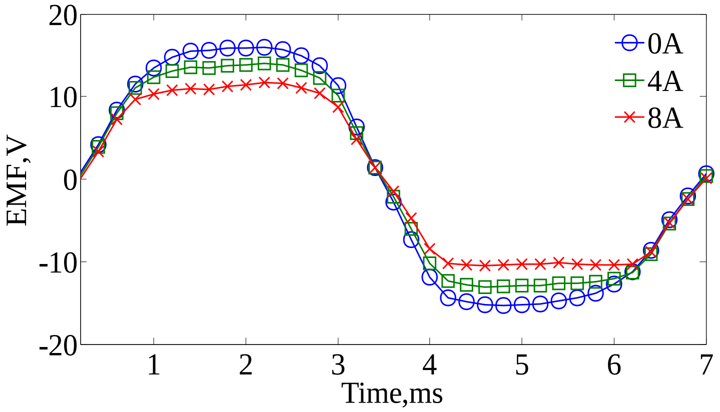

(a)

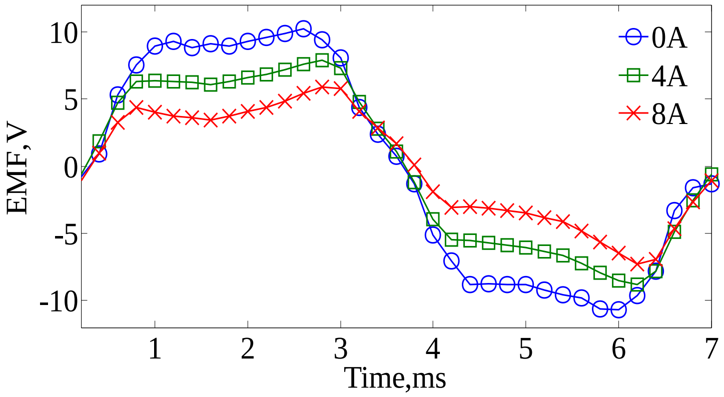

(b)

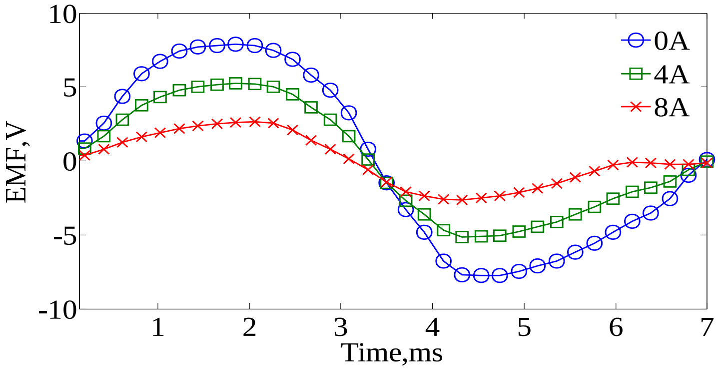

(c)

Figure 6.8 Back-EMF waveforms. (a) DPM. (b) RPM. (c) SPM.

The flux weakening capability of DPM is not that significant as DPM has the strongest PM excitation. The ratio of flux weakening of the studied DEP-DCF-HEMs or n_{max}/n_{rate} are given in Fig. 6.9. The maximum flux weakening times are 1.51, 2.1 and 5.83 for DPM, RPM and SPM, respectively.

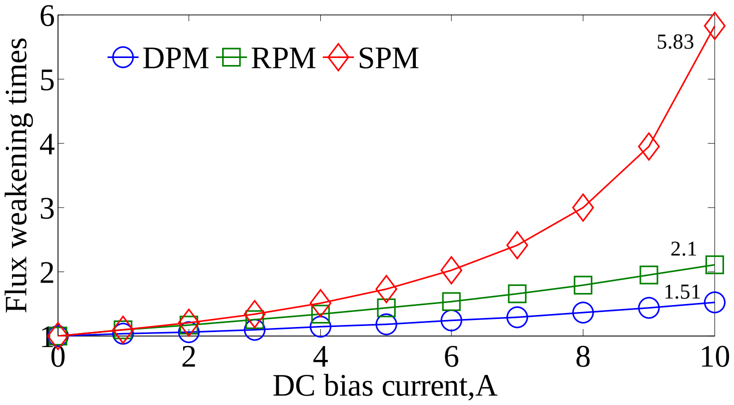

Figure 6.9 The ratio of flux weakening.

6.5.3 Torque characteristics

Fig. 6.10 shows the stationary torque waveforms, in which no DC bias current is applied, and the RMS armature current density is 8A/mm^2. It can be observed that DPM motor can produce the highest torque among DPM, RPM and SPM motors.

The steady torque waveforms are given in Fig. 6.11, the torque ripple ratio of DPM, RPM and SPM are 7.9%, 11.3% and 5%, respectively.

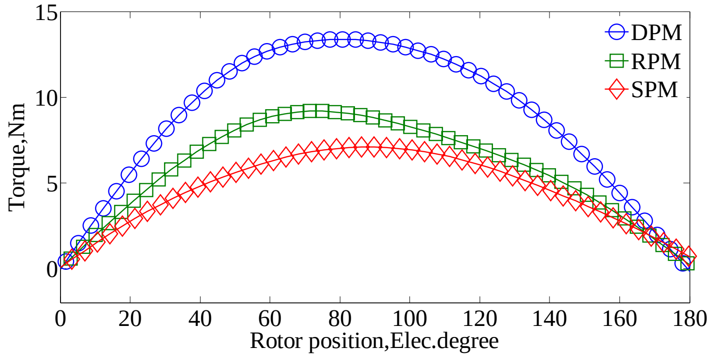

Figure 6.10 Stationary torque waveforms.

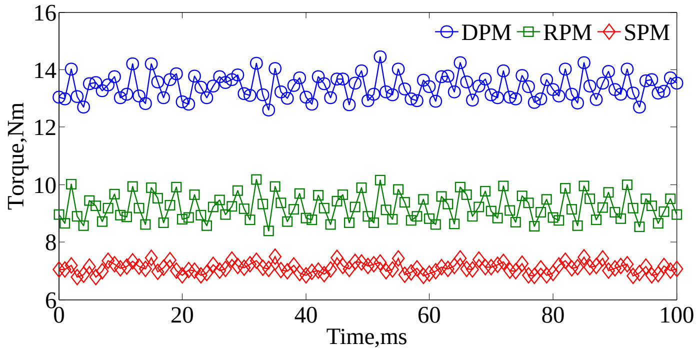

Figure 6.11 Steady torque waveforms.

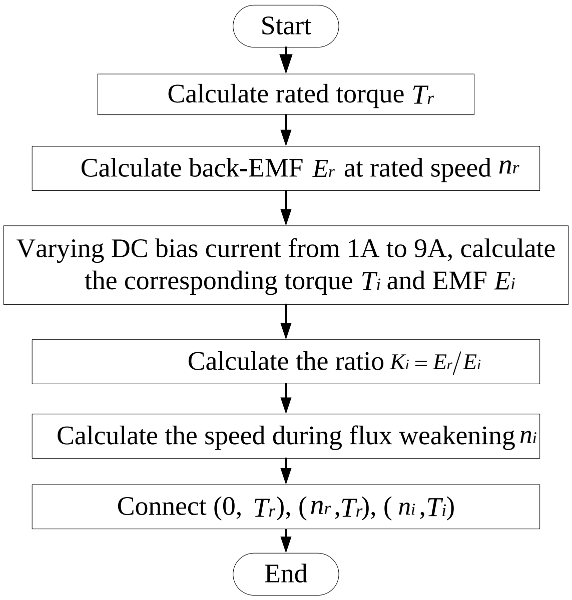

Figure 6.12 Flow chart of the calculation process of torque-speed curve.

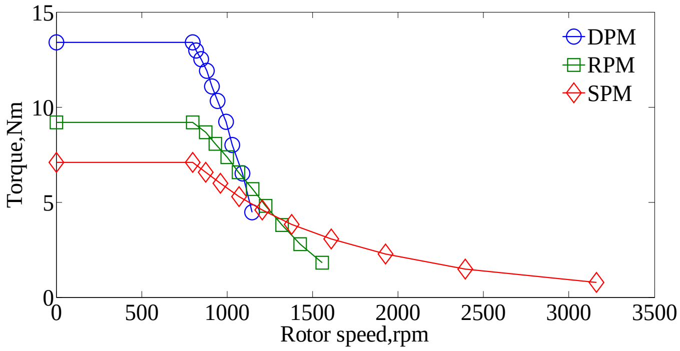

Figure 6.13 Torque versus speed waveforms.

Fig. 6.12 shows the flow chart of the calculation process of torque-speed curve, and the results are given in Fig. 6.13. The torque when the machine runs below rated speed n_r is rated torque T_r, which is simulated when the AC current density is 8A/mm^2 and DC bias current is zero. When calculating torque-speed curve over the rated speed, the back-EMF when the machine runs at rated speed E_r is calculated and recorded first, then applying DC bias current from 1A to 9A, and calculate the corresponding EMF E_i, $i = 1, 2...9$ and torque T_i, $i = 1, 2...9$. The ratio of E_r over E_i, $i = 1, 2...9$ is defined as K_i

$$K_i = \frac{E_r}{E_i}, \quad i = 1, 2...9 \tag{6.15}$$

And the machine speeds correspond to T_i, $i = 1, 2...9$ can be obtained by multiplying n_r and K_i

$$n_i = n_r K_i, \quad i = 1, 2...9 \tag{6.16}$$

The torque-speed curve can be obtained by connecting $(0, T_r)$, (n_r, T_r), (n_i, T_i)($i = 1, 2...9$). It should be noted that there is a conflict between the torque density and flux weakening capability. In order to increase torque density, strong PM excitation should be used and the flux weakening capability is reduced accordingly.

6.5.4 Efficiency maps

The efficiency maps of the DCF-HEMs are simulated and shown in Fig. 6.14. One can find that DPM has the highest efficiency since it has the largest torque density. The detailed electromagnetic performances of the DCF-HEMs are listed in Table 6.2. One can find that although SPM has the lowest torque density, it has the highest torque per PM volume (T/PMV) value, which shows a good utilization of PM material. A surface mounted permanent magnet motor and an interior permanent magnet motor are modeled as benchmark, which have the same overall sizes and copper loss as the DCF-HEMs in our paper. The torque density is 16.94kNm/m^3 for surface mounted permanent magnet motor and 21kNm/m^3 for interior permanent magnet motor, when the current density is 8A/mm^2. Therefore, the proposed DPM can achieve the highest torque density compared with normal permanent magnet motor, RPM and SPM.

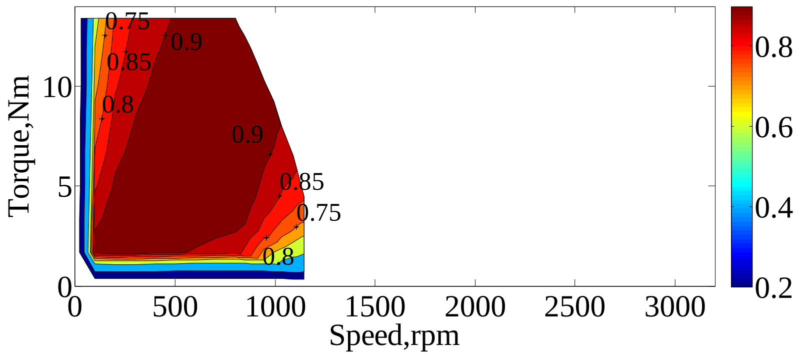

(a)

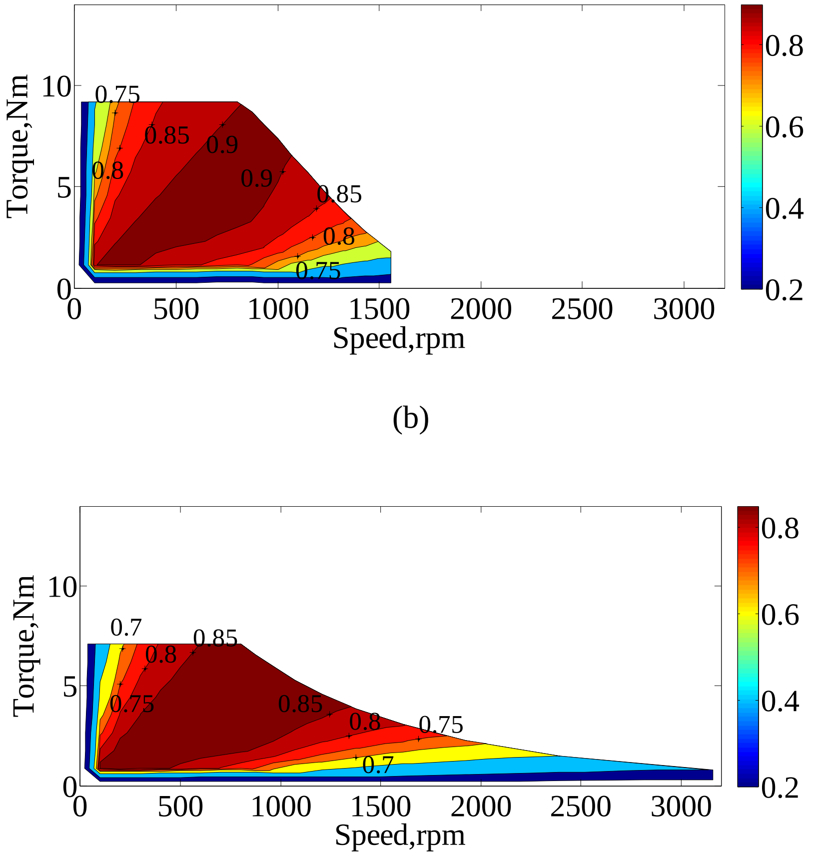

(b)

(c)

Figure 6.14 Efficiency maps. (a) DPM. (b) RPM. (c) SPM.

TABLE 6.2 ELECTROMAGNETIC PERFORMANCES

Items	DPM	RPM	SPM
Rated power (W)	1122	770	595
Rated speed (rpm)	800	800	800
Rated torque (Nm)	13.4	9.2	7.1
Ratio of flux weakening	1.51	2.1	5.83
PM usage(cm^3)	28.9	20	5.6
Torque density(kNm/m^3)	26.3	18	13.9
T/PMV(kNm/m^3)	464	460	1268

6.6 EXPERIMENTAL VERIFICATION

6.6.1 Test bench

In order to verify the principles and design of DCF-HEMs, a DPM prototype is made and experimental investigations are conducted. The design parameters are the same as given in Table 6.1. Fig. 6.15 shows the test bench, which includes the prototype, a torque sensor for torque measurement, a servo motor and servo controller used to generate adjustable load torque, DC power source and inverter to drive the prototype, and an oscilloscope used to display the tested waveforms.

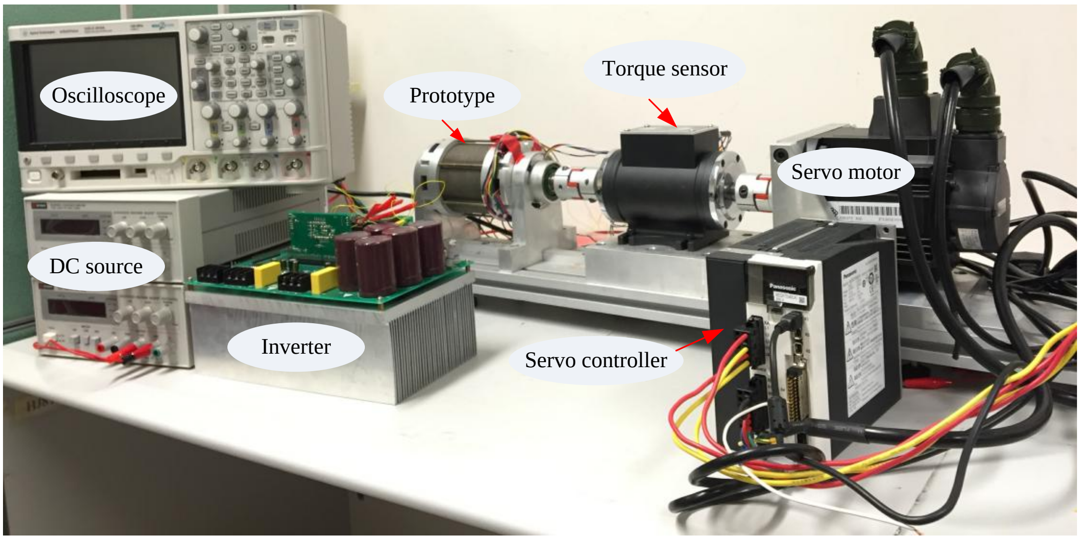

Figure 6.15 Test bench of the DPM.

6.6.2 EMF measurement

Fig. 6.16 shows the measured EMF waveforms of sub-phase one when the machine runs at 800rpm, balanced waveforms can be obtained which shows the feasibility of the proposed design. The measured and simulated EMF waveform of sub-phase A1 are compared in Fig. 6.17, one can see good agreement between the measured curve and simulated curve.

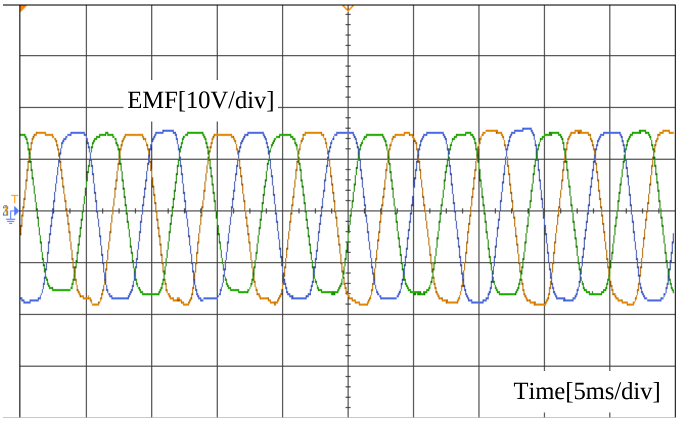

Figure 6.16 Back EMF waveforms of sub-phase one.

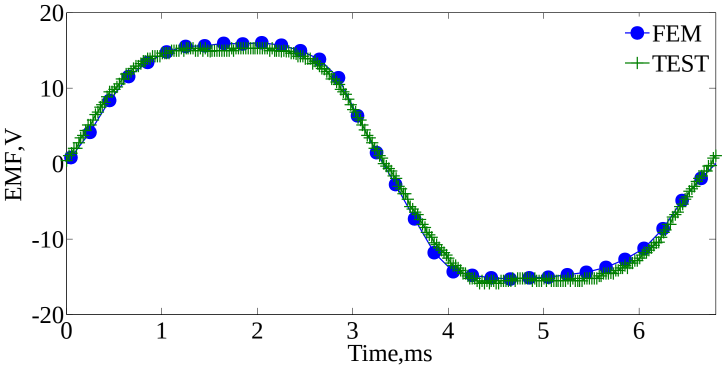

Figure 6.17 Back EMF waveforms of sub-phase A1.

6.6.3 Steady state performance

The steady state torque when the RMS armature current is 4A and DC bias current is 6A is measured, as given in Fig. 6.18. The machine speed is 800rpm during this measurement. It can be observed that stable electromagnetic torque can be generated. Fig. 6.19 shows the torque values when applied with different DC bias currents, the equivalent current I_e is fixed at 10A during the test. Again, one can find good agreement between the tested results and simulated ones. The output decreases with the increasing of DC bias current. The major reason behind is that increasing DC bias current will reduce the RMS armature current, and the electromagnetic torque decreases accordingly. Also, increasing DC bias current will result in flux weakening, which will reduce the torque as well.

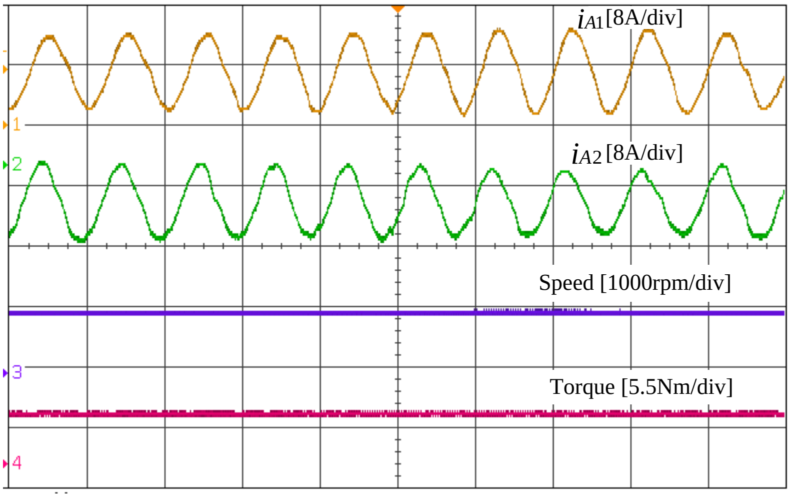

Figure 6.18 Steady state torque, speed and phase currents.

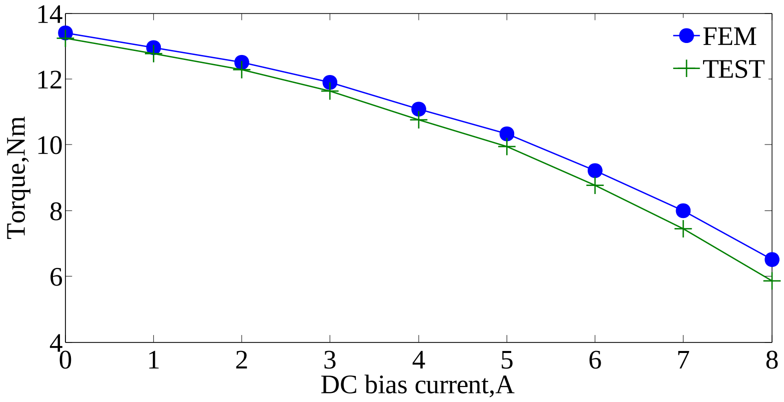

Figure 6.19 Torque values when applied with different DC bias currents.

6.6.4 Efficiency maps

The efficiency map of the DPM over the whole operating region is investigated, and compared with the efficiency when using external DC field current control as used in traditional hybrid excited machines, as given in Fig. 6.20. One can find that the proposed machine can achieve both higher torque and wider flux weakening range.

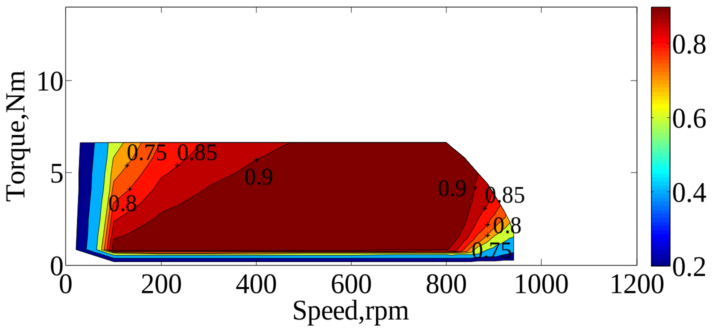

(a)

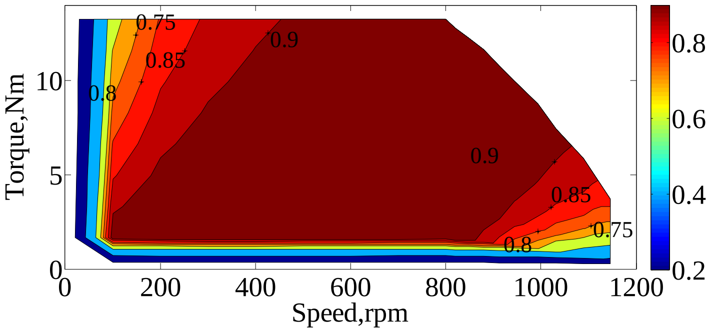

(b)

Figure 6.20 Efficiency maps. (a) External DC field current control. (b) DC bias current control.

6.7 SUMMARY

In this chapter, the idea of integrated field and armature windings is incorporated into the design of novel hybrid excited machines with bi-directional flux modulating effect. Field windings in traditional hybrid excited machines are eliminated and DC bias current is injected into the windings to act as flux regulator. Analytical model of bi-directional flux modulating effect is established and harmonics excited by different magnetic sources are investigated in detail, which can give a physical insight of the working principle.

Three finite element models which are SPM with stator PM excitation, RPM with rotor PM excitation, and DPM with dual PM excitations are built and compared. Their electromagnetic performances are deeply studied, and the results show that DPM can achieve the highest torque density and SPM has the widest flux weakening range. All these three machines can realize flux weakening through DC bias current control. A prototype of DPM is made, and experimental tests are conducted which well verifies its electromagnetic design.

CHAPTER 7 CONCLUSIONS AND RECOMMENDATIONS

7.1 CONCLUSIONS

This thesis incorporates the flux modulating theory and flux controllability into the design of electrical machines, which results in flux-controllable flux-modulated (FCFM) machines. This kind of machines can achieve both high torque density due to the flux modulating effect, and wide speed range introduced by the good flux controllability. Three major machine concepts are proposed, which are dual stator memory machines, hybrid excited dual PM machine and DC coil free hybrid excited machines. The research objectives have been achieved and conclusions are discussed as following:

Firstly, the literature review is conducted, in which flux-controllable machines and flux-modulated machines are reviewed separately. The configuration, working principle, advantages and disadvantages, and application of each machine concept are discussed and compared, which gives a clear scope of the development of the current techniques.

Secondly, flux-modulated memory machines with dual stators are proposed. Hybrid PM excitation is employed, in which AlNiCo can act as flux regulator and NdFeB is used to generate electromagnetic torque. The flux regulating theory is discussed based on the demagnetization model of AlNiCo. FEM is employed to analyze the electromagnetic performances, the results show that the proposed flux-modulated memory machines can achieve both high torque density and good flux regulating capability.

Thirdly, the flux-modulated memory machine is designed with five phases, so it can work under fault conditions. The current control method under open circuit fault is discussed, which shows that stable torque can still be generated by controlling the current of the remaining healthy windings. The torque characteristics under open circuit conditions are compared with normal condition. The results show that average torque is reduced and torque ripple is increased during open circuit condition. The reason is because the amplitude of fundamental field component is reduced while the amplitude of harmonic field components is increased.

Fourthly, a hybrid-excited dual PM machine is proposed, which incorporates the outer stator and inner stator of the dual stator flux modulated machine into one stator, and the mechanical structure is simplified. Through controlling the field current, the air-gap field can be both strengthened and weakened, and EMF and torque can be adjusted accordingly. Compared with traditional single PM machine, the proposed dual PM machine can achieve higher torque density.

Fifthly, the application of a hybrid excited flux bidirectional modulated machine in wind power generation is studied. Two control strategies are investigated, which are constant voltage control and MPPT control. A Siemens 1212C PLC controller stored with the wind turbine parameters and wind curves is used to simulate the real wind, and the load is provided by a slide rheostat. The experimental results show that this machine can achieve both constant voltage control and MPPT control by controlling field current. Therefore, thyristor based controlled rectifier in traditional wind power generation systems can be replaced with diode based uncontrolled rectifier with the proposed generator, which can reduce the hardware cost.

Lastly, the idea of integrated winding is applied to the design of hybrid excited machines and DC-coil-free hybrid-excited machines are proposed. Different from field regulation in traditional hybrid excited machines with additional field windings, DC bias current is injected into the winding to act as field regulator. The slot utilization can be improved. The proposed machine can achieve both higher torque density and wider speed range than traditional hybrid excited machines. Experimental investigations are conducted, and the results show the effectiveness of the proposed design.

In summary, this thesis incorporates flux controllability and flux modulating into electrical machine design. After a systematical literature review of the current techniques, a series of flux controllable flux modulated machines are proposed. Although their configurations are different and they have different features, their design principles are identical, which is based on bidirectional flux modulating theory. The electromagnetic performances of the proposed machines are comprehensively studied using FEM. Some prototypes are made, and experimental investigations are conducted to verify the electromagnetic design.

7.2 RECOMMENDATIONS

Although systematic research and the design, analysis and application of novel flux-controllable flux-modulated machines have been accomplished in this thesis, there are still some aspects to be further studied. Some recommendations are given as follows：

a) The flux controllable flux modulated machines are based on bidirectional flux modulating effect, which results in low power factor. Therefore, it would be interesting to explore machine concepts with high power factor.
b) When AlNiCo magnet is used, the transient performances and accurate control methods need to be studied further.
c) The driver of DC coil free hybrid excited machines has two sets of converters, which doubles the converter cost. It would be meaningful to explore new converter topologies for the DC coil free hybrid excited machines.

REFERENCES

[1] D. G. Dorrell, "Are wound-rotor synchronous motors suitable for use in high efficiency torque-dense automotive drives?," in *IECON 2012 - 38th Annual Conference on IEEE Industrial Electronics Society*, 2012, pp. 4880-4885.

[2] K. Hruska, V. Kindl, and R. Pechanek, "Design and FEM analyses of an electrically excited automotive synchronous motor," in *Power Electronics and Motion Control Conference (EPE/PEMC), 2012 15th International*, 2012, pp. LS2e.2-1-LS2e.2-7.

[3] C. Rossi, D. Casadei, A. Pilati, and M. Marano, "Wound rotor salient pole synchronous machine drive for electric traction," in *Industry Applications Conference, 2006. 41st IAS Annual Meeting. Conference Record of the 2006 IEEE*, 2006, pp. 1235-1241.

[4] W. Q. Chu, Z. Q. Zhu, and J. T. Chen, "Simplified Analytical Optimization and Comparison of Torque Densities Between Electrically Excited and Permanent-Magnet Machines," *Industrial Electronics, IEEE Transactions on,* vol. 61, pp. 5000-5011, 2014.

[5] M. Bash, S. Pekarek, S. Sudhoff, J. Whitmore, and M. Frantzen, "A comparison of permanent magnet and wound rotor synchronous machines for portable power generation," in *Power and Energy Conference at Illinois (PECI), 2010*, 2010, pp. 1-6.

[6] V. Ostovic, "Performance comparison of wound field and permanent magnet excited electric machines," in *Energy Conference (ENERGYCON), 2014 IEEE International*, 2014, pp. 106-112.

[7] W. Chu, Z. Zhu, J. Zhang, X. Liu, D. Stone, and M. Foster, "Investigation on Operational Envelops and Efficiency Maps of Electrically Excited Machines for Electrical Vehicle Applications," *Magnetics, IEEE Transactions on,* vol. 51, pp. 1-10, 2015.

[8] L. Sang-Ho, O. K. Soon, L. Jeong-Jong, and H. Jung-Pyo, "Characteristic

Analysis of Claw-Pole Machine Using Improved Equivalent Magnetic Circuit," *Magnetics, IEEE Transactions on,* vol. 45, pp. 4570-4573, 2009.

[9] C. Kaehler and G. Henneberger, "Transient 3-D FEM computation of eddy-current losses in the rotor of a claw-pole alternator," *Magnetics, IEEE Transactions on,* vol. 40, pp. 1362-1365, 2004.

[10] L. Li, A. Kedous-Lebouc, A. Foggia, and J. C. Mipo, "Influence of Magnetic Materials on Claw Pole Machines Behavior," *Magnetics, IEEE Transactions on,* vol. 46, pp. 574-577, 2010.

[11] Y. G. Guo, J. G. Zhu, and H. Y. Lu, "Accurate determination of parameters of a claw-pole motor with SMC stator core by finite-element magnetic-field analysis," *Electric Power Applications, IEE Proceedings -,* vol. 153, pp. 568-574, 2006.

[12] G. Youguang, Z. Jianguo, and D. G. Dorrell, "Design and Analysis of a Claw Pole Permanent Magnet Motor With Molded Soft Magnetic Composite Core," *Magnetics, IEEE Transactions on,* vol. 45, pp. 4582-4585, 2009.

[13] S. Yang, Z. Q. Zhu, J. T. Chen, R. P. Deodhar, and A. Pride, "Analytical Modeling of Claw-Pole Stator SPM Brushless Machine Having SMC Stator Core," *Magnetics, IEEE Transactions on,* vol. 49, pp. 3830-3833, 2013.

[14] L. Chengcheng, Z. Jianguo, W. Youhua, G. Youguang, and L. Gang, "Comparison of Claw-Pole Machines With Different Rotor Structures," *Magnetics, IEEE Transactions on,* vol. 51, pp. 1-4, 2015.

[15] D. Yiping, G. Youguang, Z. Jian Guo, and L. Haiyan, "Effect of Armature Reaction of a Permanent-Magnet Claw Pole SMC Motor," *Magnetics, IEEE Transactions on,* vol. 43, pp. 2561-2563, 2007.

[16] R. Rebhi, A. Ibala, and A. Masmoudi, "MEC-Based Sizing of a Hybrid-Excited Claw Pole Alternator," *Industry Applications, IEEE Transactions on,* vol. 51, pp. 211-223, 2015.

[17] F. N. Jurca and C. Martis, "Theoretical and experimental analysis of a

three-phase permanent magnet claw-pole synchronous generator," *Electric Power Applications, IET,* vol. 6, pp. 491-503, 2012.

[18] F. Liang, Y. Liao, and T. Lipo, "A new variable reluctance motor utilizing an auxiliary commutation winding," *Industry Applications, IEEE Transactions on,* vol. 30, pp. 423-432, 1994.

[19] L. Chunhua, K. T. Chau, Z. Jin, and L. Jiangui, "Design and Analysis of a HTS Brushless Doubly-Fed Doubly-Salient Machine," *Applied Superconductivity, IEEE Transactions on,* vol. 21, pp. 1119-1122, 2011.

[20] X. Liu and Z. Q. Zhu, "Comparative Study of Novel Variable Flux Reluctance Machines With Doubly Fed Doubly Salient Machines," *Magnetics, IEEE Transactions on,* vol. 49, pp. 3838-3841, 2013.

[21] K. Xiangxin, C. Ming, and S. Yagang, "Flux-weakening control of constant power of stator-doubly-fed doubly salient motor for electric vehicles," in *Electrical Machines and Systems, 2008. ICEMS 2008. International Conference on*, 2008, pp. 1721-1725.

[22] F. Ying and K. T. Chau, "Design, Modeling, and Analysis of a Brushless Doubly Fed Doubly Salient Machine for Electric Vehicles," *Industry Applications, IEEE Transactions on,* vol. 44, pp. 727-734, 2008.

[23] F. Ying, K. T. Chau, and S. Niu, "Development of a New Brushless Doubly Fed Doubly Salient Machine for Wind Power Generation," *Magnetics, IEEE Transactions on,* vol. 42, pp. 3455-3457, 2006.

[24] X. Liu, Z. Zhu, and Z. Pan, "Analysis of electromagnetic torque in sinusoidal excited switched reluctance machines having DC bias in excitation," in *Electrical Machines (ICEM), 2012 XXth International Conference on*, 2012, pp. 2882-2888.

[25] Z. Q. Zhu and X. Liu, "Novel Stator Electrically Field Excited Synchronous Machines Without Rare-Earth Magnet," *Magnetics, IEEE Transactions on,* vol. 51, pp. 1-9, 2015.

[26] J. A. Tapia, F. Leonardi, and T. A. Lipo, "Consequent-pole permanent-magnet machine with extended field-weakening capability," *Industry Applications, IEEE Transactions on*, vol. 39, pp. 1704-1709, 2003.

[27] L. Chunhua, Z. Jin, and K. T. Chau, "A Novel Flux-Controllable Vernier Permanent-Magnet Machine," *Magnetics, IEEE Transactions on*, vol. 47, pp. 4238-4241, 2011.

[28] L. Chunhua, "Design of a new outer-rotor flux-controllable vernier PM in-wheel motor drive for electric vehicle," in *Electrical Machines and Systems (ICEMS), 2011 International Conference on*, 2011, pp. 1-6.

[29] X. Luo and T. A. Lipo, "A synchronous/permanent magnet hybrid AC machine," *IEEE TRANSACTIONS ON ENERGY CONVERSION EC*, vol. 15, pp. 203-210, 2000.

[30] T. Finken and K. Hameyer, "Study of Hybrid Excited Synchronous Alternators for Automotive Applications Using Coupled FE and Circuit Simulations," *Magnetics, IEEE Transactions on*, vol. 44, pp. 1598-1601, 2008.

[31] N. Naoe and T. Fukami, "Trial production of a hybrid excitation type synchronous machine," in *Electric Machines and Drives Conference, 2001. IEMDC 2001. IEEE International*, 2001, pp. 545-547.

[32] N. Youyuan, W. Qunjing, B. Xiaohua, and Z. Weiguo, "Optimal design of a hybrid excitation claw-pole alternator based on a 3-D MEC method," in *Electrical Machines and Systems, 2005. ICEMS 2005. Proceedings of the Eighth International Conference on*, 2005, pp. 644-647 Vol. 1.

[33] F. Leonardi, T. Matsuo, Y. Li, T. A. Lipo, and P. McCleer, "Design considerations and test results for a doubly salient PM motor with flux control," in *Industry Applications Conference, 1996. Thirty-First IAS Annual Meeting, IAS '96., Conference Record of the 1996 IEEE*, 1996, pp. 458-463 vol.1.

[34] Z. Xiaoyong, C. Ming, H. Wei, Z. Jianzhong, and Z. Wenxiang, "Design and Analysis of a New Hybrid Excited Doubly Salient Machine Capable of Field Control," in *Industry Applications Conference, 2006. 41st IAS Annual Meeting. Conference Record of the 2006 IEEE,* 2006, pp. 2382-2389.

[35] Z. Xiaoyong, C. Ming, Z. Wenxiang, L. Chunhua, and K. T. Chau, "A Transient Cosimulation Approach to Performance Analysis of Hybrid Excited Doubly Salient Machine Considering Indirect Field-Circuit Coupling," *Magnetics, IEEE Transactions on,* vol. 43, pp. 2558-2560, 2007.

[36] K. T. Chau, J. Z. Jiang, and W. Yong, "A novel stator doubly fed doubly salient permanent magnet brushless machine," *Magnetics, IEEE Transactions on,* vol. 39, pp. 3001-3003, 2003.

[37] C. Zhihui, W. Bo, C. Zhe, and Y. Yangguang, "Comparison of Flux Regulation Ability of the Hybrid Excitation Doubly Salient Machines," *Industrial Electronics, IEEE Transactions on,* vol. 61, pp. 3155-3166, 2014.

[38] H. Wei, Z. Gan, and C. Ming, "Flux-Regulation Theories and Principles of Hybrid-Excited Flux-Switching Machines," *Industrial Electronics, IEEE Transactions on,* vol. 62, pp. 5359-5369, 2015.

[39] Z. Gan, H. Wei, C. Ming, L. Jinguo, W. Kai, and Z. Jianzhong, "Investigation of an Improved Hybrid-Excitation Flux-Switching Brushless Machine for HEV/EV Applications," *Industry Applications, IEEE Transactions on,* vol. 51, pp. 3791-3799, 2015.

[40] R. L. Owen, Z. Q. Zhu, and G. W. Jewell, "Hybrid-Excited Flux-Switching Permanent-Magnet Machines With Iron Flux Bridges," *Magnetics, IEEE Transactions on,* vol. 46, pp. 1726-1729, 2010.

[41] B. J. Chalmers, R. Akmese, and L. Musaba, "Design and field-weakening performance of permanent-magnet/reluctance motor with two-part rotor," *Electric Power Applications, IEE Proceedings -*, vol. 145, pp. 133-139, 1998.

[42] W. Yu and D. Zhiquan, "Hybrid Excitation Topologies and Control Strategies

of Stator Permanent Magnet Machines for DC Power System," *Industrial Electronics, IEEE Transactions on,* vol. 59, pp. 4601-4616, 2012.

[43] W. Yu and D. Zhiquan, "Comparison of Hybrid Excitation Topologies for Flux-Switching Machines," *Magnetics, IEEE Transactions on,* vol. 48, pp. 2518-2527, 2012.

[44] V. Ostovic, "Memory motors-a new class of controllable flux PM machines for a true wide speed operation," in *Industry Applications Conference, 2001. Thirty-Sixth IAS Annual Meeting. Conference Record of the 2001 IEEE*, 2001, pp. 2577-2584 vol.4.

[45] V. Ostovic, "Memory motors," *Industry Applications Magazine, IEEE,* vol. 9, pp. 52-61, 2003.

[46] L. Hengchuan, L. Heyun, S. Fang, and Z. Q. Zhu, "Permanent Magnet Demagnetization Physics of a Variable Flux Memory Motor," *Magnetics, IEEE Transactions on,* vol. 45, pp. 4736-4739, 2009.

[47] L. Jung Ho and H. Jung Pyo, "Permanent Magnet Demagnetization Characteristic Analysis of a Variable Flux Memory Motor Using Coupled Preisach Modeling and FEM," *Magnetics, IEEE Transactions on,* vol. 44, pp. 1550-1553, 2008.

[48] Y. Chen, W. Pan, Y. Wang, R. Tang, and J. Wang, "Interior composite-rotor controllable-flux PMSM - memory motor," in *Electrical Machines and Systems, 2005. ICEMS 2005. Proceedings of the Eighth International Conference on*, 2005, pp. 446-449 Vol. 1.

[49] J. Huang, X. Wang, and Z. Sun, "Variable flux memory motors: A review," in *Transportation Electrification Asia-Pacific (ITEC Asia-Pacific), 2014 IEEE Conference and Expo*, 2014, pp. 1-6.

[50] Y. Chen, L. Kong, and W. Zhong, "Finite element analysis of interior composite-rotor controllable flux permanent magnet synchronous machine," in *Electrical Machines and Systems, 2009. ICEMS 2009. International*

Conference on, 2009, pp. 1-4.

[51] Y.-G. Chen, Y. Wang, Y.-H. Shen, and R.-Y. Tang, "MAGNETIC CIRCUIT DESIGN AND FINITE ELEMENT ANALYSIS OF WIDE-SPEED CONTROLLABLE-FLUX PMSM [J]," *Proceedings of the Csee*, vol. 20, p. 029, 2005.

[52] H. Lin, H. Liu, Y. Huang, and S. Fang, "Characteristic analysis and experimental study of a hybrid permanent magnet variable flux memory motor," in *Zhongguo Dianji Gongcheng Xuebao(Proceedings of the Chinese Society of Electrical Engineering)*, 2011, pp. 71-76.

[53] K. Sakai, K. Yuki, Y. Hashiba, N. Takahashi, and K. Yasui, "Principle of the variable-magnetic-force memory motor," in *Electrical Machines and Systems, 2009. ICEMS 2009. International Conference on*, 2009, pp. 1-6.

[54] Y. Chuang and K. T. Chau, "Design, Analysis, and Control of DC-Excited Memory Motors," *Energy Conversion, IEEE Transactions on,* vol. 26, pp. 479-489, 2011.

[55] Y. Chuang, K. T. Chau, and J. Z. Jiang, "A permanent-magnet flux-mnemonic integrated-starter-generator for hybrid electric vehicles," in *Vehicle Power and Propulsion Conference, 2008. VPPC '08. IEEE*, 2008, pp. 1-6.

[56] C. Yu and K. T. Chau, "New fault-tolerant flux-mnemonic doubly-salient permanent-magnet motor drive," *Electric Power Applications, IET,* vol. 5, pp. 393-403, 2011.

[57] L. Fuhua, K. T. Chau, L. Chunhua, J. Z. Jiang, and W. Winson Yong, "Design and Analysis of Magnet Proportioning for Dual-Memory Machines," *Applied Superconductivity, IEEE Transactions on,* vol. 22, pp. 4905404-4905404, 2012.

[58] L. Fuhua, K. T. Chau, L. Chunhua, and Z. Zhen, "Design Principles of Permanent Magnet Dual-Memory Machines," *Magnetics, IEEE Transactions on,* vol. 48, pp. 3234-3237, 2012.

[59] L. Wenlong, K. T. Chau, G. Yu, J. Z. Jiang, and L. Fuhua, "A New Flux-Mnemonic Dual-Magnet Brushless Machine," *Magnetics, IEEE Transactions on*, vol. 47, pp. 4223-4226, 2011.

[60] L. Fuhua, K. T. Chau, L. Chunhua, and Q. Chun, "New Approach for Pole-Changing With Dual-Memory Machine," *Applied Superconductivity, IEEE Transactions on*, vol. 24, pp. 1-4, 2014.

[61] F. Li, K. T. Chau, and C. Liu, "Pole-Changing Flux-Weakening DC-Excited Dual-Memory Machines for Electric Vehicles," *Energy Conversion, IEEE Transactions on*, vol. PP, pp. 1-10, 2015.

[62] C. Dajian, Z. Xiaoyong, Q. Li, D. Qian, W. Zheng, and C. Ming, "Electromagnetic performance analysis and fault-tolerant control of new doubly salient flux memory motor drive," in *Electrical Machines and Systems (ICEMS), 2010 International Conference on*, 2010, pp. 834-838.

[63] Z. Xiaoyong, Q. Li, C. Dajian, C. Ming, W. Zheng, and L. Wenlong, "Design and Analysis of a New Flux Memory Doubly Salient Motor Capable of Online Flux Control," *Magnetics, IEEE Transactions on*, vol. 47, pp. 3220-3223, 2011.

[64] L. Chunhua, K. T. Chau, and Q. Chun, "Design and Analysis of a New Magnetic-Geared Memory Machine," *Applied Superconductivity, IEEE Transactions on*, vol. 24, pp. 1-5, 2014.

[65] W. Qingsong, N. Shuangxia, H. Siu Lau, F. Weinong, and Z. Shuguang, "Design and analysis of novel magnetic flux-modulated mnemonic machines," *Electric Power Applications, IET*, vol. 9, pp. 469-477, 2015.

[66] Q. Wang and S. Niu, "Electromagnetic Design and Analysis of a Novel Fault-Tolerant Flux-Modulated Memory Machine," *Energies*, vol. 8, pp. 8069-8085, 2015.

[67] K. T. Chau, D. Zhang, J. Z. Jiang, C. Liu, and Y. Zhang, "Design of a Magnetic-Geared Outer-Rotor Permanent-Magnet Brushless Motor for

Electric Vehicles," *IEEE Transactions on Magnetics,* vol. 43, pp. 2504-2506, 2007.

[68] L. Jian, K. T. Chau, and J. Z. Jiang, "A Magnetic-Geared Outer-Rotor Permanent-Magnet Brushless Machine for Wind Power Generation," *IEEE Transactions on Industry Applications,* vol. 45, pp. 954-962, 2009.

[69] L. Wang, J.-X. Shen, P. C.-K. Luk, W.-Z. Fei, C. Wang, and H. Hao, "Development of a magnetic-geared permanent-magnet brushless motor," *Magnetics, IEEE Transactions on,* vol. 45, pp. 4578-4581, 2009.

[70] Y. Du, K. T. Chau, M. Cheng, and Y. Wang, "A linear magnetic-geared permanent magnet machine for wave energy generation," in *2010 International Conference on Electrical Machines and Systems*, 2010, pp. 1538-1541.

[71] S. Ho, Q. Wang, S. Niu, and W. Fu, "A novel magnetic-geared tubular linear machine with halbach permanent-magnet arrays for tidal energy conversion," *IEEE Transactions on Magnetics,* vol. 51, pp. 1-4, 2015.

[72] B. Kim and T. A. Lipo, "Operation and Design Principles of a PM Vernier Motor," *IEEE Transactions on Industry Applications,* vol. 50, pp. 3656-3663, 2014.

[73] A. Toba and T. Lipo, "Generic torque-maximizing design methodology of surface permanent-magnet vernier machine," *IEEE transactions on industry applications,* vol. 36, pp. 1539-1546, 2000.

[74] D. Li, R. Qu, and T. A. Lipo, "High-Power-Factor Vernier Permanent-Magnet Machines," *IEEE Transactions on Industry Applications,* vol. 50, pp. 3664-3674, 2014.

[75] S. Niu, S. L. Ho, and W. N. Fu, "Design of a Novel Electrical Continuously Variable Transmission System Based on Harmonic Spectra Analysis of Magnetic Field," *IEEE Transactions on Magnetics,* vol. 49, pp. 2161-2164, 2013.

[76] Y. Wang, S. Niu, and W. Fu, "An Electrical-Continuously Variable Transmission System Based on Doubly-Fed Flux-Bidirectional Modulation," *IEEE Transactions on Industrial Electronics,* pp. 1-1, 2016.

[77] Y. Liu, S. Niu, and W. Fu, "Design of an Electrical Continuously Variable Transmission Based Wind Energy Conversion System," *IEEE Transactions on Industrial Electronics,* vol. 63, pp. 6745-6755, 2016.

[78] X. Luo and S. Niu, "A Novel Contra-Rotating Power Split Transmission System for Wind Power Generation and its Dual MPPT Control Strategy," *IEEE Transactions on Power Electronics,* 2016.

[79] S. Niu, K. Chau, J. Jiang, and C. Liu, "Design and control of a new double-stator cup-rotor permanent-magnet machine for wind power generation," *IEEE Transactions on Magnetics,* vol. 43, pp. 2501-2503, 2007.

[80] S. Peng, W. Fu, and S. Ho, "A Novel High Torque-Density Triple-Permanent-Magnet-Excited Magnetic Gear," *Magnetics, IEEE Transactions on,* vol. 50, pp. 1-4, 2014.

[81] Y. Amara, L. Vido, M. Gabsi, E. Hoang, A. H. Ben Ahmed, and M. Lecrivain, "Hybrid Excitation Synchronous Machines: Energy-Efficient Solution for Vehicles Propulsion," *Ieee Transactions on Vehicular Technology,* vol. 58, pp. 2137-2149, Jun 2009.

[82] H. Yang, H. Lin, Z.-Q. Zhu, S. Fang, and Y. Huang, "A Dual-Consequent-Pole Vernier Memory Machine," *Energies,* vol. 9, p. 134, 2016.

[83] Z. Wu and Z. Zhu, "Analysis of air-gap field modulation and magnetic gearing effects in switched flux permanent magnet machines," *Magnetics, IEEE Transactions on,* vol. 51, pp. 1-12, 2015.

[84] H. Sterling, "Harmonic Field Effects in Induction Machines," *Electronics and Power,* vol. 23, p. 841, 1977.

[85] P. Frauman, A. Burakov, and A. Arkkio, "Effects of the slot harmonics on the

unbalanced magnetic pull in an induction motor with an eccentric rotor," *IEEE transactions on magnetics*, vol. 43, pp. 3441-3444, 2007.

[86] O. Barré and B. Napame, "Concentrated Windings in Compact Permanent Magnet Synchronous Generators: Managing Efficiency," *Machines*, vol. 4, p. 2, 2016.

[87] W. Chu and Z. Zhu, "Average torque separation in permanent magnet synchronous machines using frozen permeability," *Magnetics, IEEE Transactions on*, vol. 49, pp. 1202-1210, 2013.

[88] J. Wang, W. Wang, K. Atallah, and D. Howe, "Demagnetization assessment for three-phase tubular brushless permanent-magnet machines," *IEEE Transactions on Magnetics*, vol. 44, pp. 2195-2203, 2008.

[89] J. K. Kaldellis and D. Zafirakis, "The wind energy (r) evolution: A short review of a long history," *Renewable Energy*, vol. 36, pp. 1887-1901, 2011.

[90] B. R. Karthikeya and R. J. Schütt, "Overview of Wind Park Control Strategies," *IEEE Transactions on Sustainable Energy*, vol. 5, pp. 416-422, 2014.

[91] M. Liserre, R. Cardenas, M. Molinas, and J. Rodriguez, "Overview of Multi-MW Wind Turbines and Wind Parks," *IEEE Transactions on Industrial Electronics*, vol. 58, pp. 1081-1095, 2011.

[92] H. Polinder, J. A. Ferreira, B. B. Jensen, A. B. Abrahamsen, K. Atallah, and R. A. McMahon, "Trends in Wind Turbine Generator Systems," *IEEE Journal of Emerging and Selected Topics in Power Electronics*, vol. 1, pp. 174-185, 2013.

[93] GWEC, "http://www.gwec.net/."

[94] Q. Wang and S. Niu, "Overview of flux-controllable machines: Electrically excited machines, hybrid excited machines and memory machines," *Renewable and Sustainable Energy Reviews*, vol. 68, pp. 475-491, 2017.

[95] H. Jagau, M. A. Khan, and P. S. Barendse, "Design of a Sustainable Wind

Generator System Using Redundant Materials," *IEEE Transactions on Industry Applications,* vol. 48, pp. 1827-1837, 2012.

[96] J. Ojeda, M. G. Simoes, G. Li, and M. Gabsi, "Design of a Flux-Switching Electrical Generator for Wind Turbine Systems," *IEEE Transactions on Industry Applications,* vol. 48, pp. 1808-1816, 2012.

[97] R. Cárdenas, R. Peña, P. Wheeler, J. Clare, and G. Asher, "Control of the reactive power supplied by a WECS based on an induction generator fed by a matrix converter," *IEEE Transactions on Industrial Electronics,* vol. 56, pp. 429-438, 2009.

[98] G. Abad, M. A. Rodriguez, G. Iwanski, and J. Poza, "Direct power control of doubly-fed-induction-generator-based wind turbines under unbalanced grid voltage," *IEEE Transactions on Power Electronics,* vol. 25, pp. 442-452, 2010.

[99] K. Rothenhagen and F. W. Fuchs, "Doubly fed induction generator model-based sensor fault detection and control loop reconfiguration," *IEEE Transactions on Industrial Electronics,* vol. 56, pp. 4229-4238, 2009.

[100] J. Lopez, E. Gubia, P. Sanchis, X. Roboam, and L. Marroyo, "Wind turbines based on doubly fed induction generator under asymmetrical voltage dips," *IEEE Transactions on energy conversion,* vol. 23, pp. 321-330, 2008.

[101] S. L. Ho, Y. Shiyou, N. Guangzheng, and H. C. Wong, "An improved Tabu search for the global optimizations of electromagnetic devices," *IEEE Transactions on Magnetics,* vol. 37, pp. 3570-3574, 2001.

[102] V. Nayanar, N. Kumaresan, and N. Ammasai Gounden, "A Single-Sensor-Based MPPT Controller for Wind-Driven Induction Generators Supplying DC Microgrid," *IEEE Transactions on Power Electronics,* vol. 31, pp. 1161-1172, 2016.

[103] K. Ogata, *Modern control engineering*: Prentice Hall PTR, 2001.